NAVAL POSTGRADUATE SCHOOL

MONTEREY, CALIFORNIA

THESIS

INTER-ANNUAL VARIABILITY OF THE ACOUSTIC PROPAGATION IN THE MEDITERRANEAN SEA IDENTIFIED FROM A SYNOPTIC MONTHLY GRIDDED DATABASE AS COMPARED WITH GDEM

by

Murat Kucukosmanoglu

December 2016

Thesis Advisor: Peter C. Chu
Co-Advisor: Tetyana Margolina

Approved for public release. Distribution is unlimited.

THIS PAGE INTENTIONALLY LEFT BLANK

REPORT DOCUMENTATION PAGE		*Form Approved OMB No. 0704–0188*

Public reporting burden for this collection of information is estimated to average 1 hour per response, including the time for reviewing instruction, searching existing data sources, gathering and maintaining the data needed, and completing and reviewing the collection of information. Send comments regarding this burden estimate or any other aspect of this collection of information, including suggestions for reducing this burden, to Washington headquarters Services, Directorate for Information Operations and Reports, 1215 Jefferson Davis Highway, Suite 1204, Arlington, VA 22202-4302, and to the Office of Management and Budget, Paperwork Reduction Project (0704-0188) Washington, DC 20503.

1. AGENCY USE ONLY (*Leave blank)*	2. REPORT DATE December 2016	3. REPORT TYPE AND DATES COVERED Master's thesis	
4. TITLE AND SUBTITLE INTER-ANNUAL VARIABILITY OF THE ACOUSTIC PROPAGATION IN THE MEDITERRANEAN SEA IDENTIFIED FROM A SYNOPTIC MONTHLY GRIDDED DATABASE AS COMPARED WITH GDEM		**5. FUNDING NUMBERS** **W7A19**	
6. AUTHOR(S) Murat Kucukosmanoglu			
7. PERFORMING ORGANIZATION NAME(S) AND ADDRESS(ES) Naval Postgraduate School Monterey, CA 93943-5000		**8. PERFORMING ORGANIZATION REPORT NUMBER**	
9. SPONSORING /MONITORING AGENCY NAME(S) AND ADDRESS(ES) Naval Research Program (NRP), CNO-N2N6E		**10. SPONSORING / MONITORING AGENCY REPORT NUMBER**	

11. SUPPLEMENTARY NOTES The views expressed in this thesis are those of the author and do not reflect the official policy or position of the Department of Defense or the U.S. Government. IRB number _____N/A_____.		
12a. DISTRIBUTION / AVAILABILITY STATEMENT Approved for public release. Distribution is unlimited.		**12b. DISTRIBUTION CODE**

13. ABSTRACT (maximum 200 words)

The primary area of this research is to identify inter-annual variability of acoustic propagation in the Mediterranean Sea through comparison of sound speed profiles obtained from the synoptic monthly gridded World Ocean Database (SMD-WOD) and Generalized Digital Environmental Model (GDEM) temperature (T) and salinity (S) data. The SMG-WOD for the region of interest in this study has 0.25°×0.25° horizontal resolutions, 28 vertical levels from the surface to 3000-meter depth, one-month temporal increment from January 1960 to December 2014. It provides the long-term spatial and temporal variability of the (T, S) and sound speed profile data. However, the GDEM offers climatological monthly mean (T, S) data with 0.25 horizontal resolution and 78 vertical depths from the surface to 6600 meters. Five distinct points were chosen in order to model acoustic propagation to account for significant differences in mean salinity, temperature vertical profiles and bottom sediments between sub-basins. Overall, we found that the Levantine Surface Water (LSW) has the highest spiciness among the all water masses. We analyzed that transmission loss (TL) for each decade, and we found that there are inter-annual TL variabilities. TL does not show high inter-annual variabilities over convergence zone paths; however, it shows high inter-annual variability on surface duct, bottom bounce and sound channels.

14. SUBJECT TERMS Mediterranean Sea			**15. NUMBER OF PAGES** 169
			16. PRICE CODE
17. SECURITY CLASSIFICATION OF REPORT Unclassified	**18. SECURITY CLASSIFICATION OF THIS PAGE** Unclassified	**19. SECURITY CLASSIFICATION OF ABSTRACT** Unclassified	**20. LIMITATION OF ABSTRACT** UU

NSN 7540–01-280-5500

Standard Form 298 (Rev. 2–89)
Prescribed by ANSI Std. 239–18

i

THIS PAGE INTENTIONALLY LEFT BLANK

INTER-ANNUAL VARIABILITY OF THE ACOUSTIC PROPAGATION IN THE MEDITERRANEAN SEA IDENTIFIED FROM A SYNOPTIC MONTHLY GRIDDED DATABASE AS COMPARED WITH GDEM

Murat Kucukosmanoglu
Lieutenant Junior Grade, Turkish Navy
B.S., Turkish Naval Academy, 2011

Submitted in partial fulfillment of the
requirements for the degree of

**MASTER OF SCIENCE IN METEOROLOGY
AND PHYSICAL OCEANOGRAPHY**

from the

**NAVAL POSTGRADUATE SCHOOL
December 2016**

Approved by: Peter C. Chu
                   Thesis Advisor

                   Tetyana Margolina
                   Co-Advisor

                   Peter C. Chu
                   Chair, Department of Oceanography

THIS PAGE INTENTIONALLY LEFT BLANK

ABSTRACT

The primary area of this research is to identify inter-annual variability of acoustic propagation in the Mediterranean Sea through comparison of sound speed profiles obtained from the synoptic monthly gridded World Ocean Database (SMD-WOD) and Generalized Digital Environmental Model (GDEM) temperature (T) and salinity (S) data. The SMG-WOD for the region of interest in this study has 0.25°×0.25° horizontal resolutions, 28 vertical levels from the surface to 3000-meter depth, one-month temporal increment from January 1960 to December 2014. It provides the long-term spatial and temporal variability of the (T, S) and sound speed profile data. However, the GDEM offers climatological monthly mean (T, S) data with 0.25 horizontal resolution and 78 vertical depths from the surface to 6600 meters. Five distinct points were chosen in order to model acoustic propagation to account for significant differences in mean salinity, temperature vertical profiles and bottom sediments between sub-basins. Overall, we found that the Levantine Surface Water (LSW) has the highest spiciness among the all water masses. We analyzed that transmission loss (TL) for each decade, and we found that there are inter-annual TL variabilities. TL does not show high inter-annual variabilities over convergence zone paths; however, it shows high inter-annual variability on surface duct, bottom bounce and sound channels.

THIS PAGE INTENTIONALLY LEFT BLANK

TABLE OF CONTENTS

LIST OF FIGURES

x

LIST OF TABLES

THIS PAGE INTENTIONALLY LEFT BLANK

LIST OF ACRONYMS AND ABBREVIATIONS

AG   array gain

AW   Atlantic water

ASW   anti-submarine warfare

CTD   conductivity temperature depth

DBDB-V   Digital bathymetric Database-Variable resolution version

EOF   empirical orthogonal function

EMED   Eastern Mediterranean Deep Water

GDEM   generalized digital environmental model

GLD   glider

NATO   North Atlantic Treaty Organization

LIW   Levantine Intermediate Water

LSW   Levantine Surface Water

LB   Levantine Basin

MAW   Modified Atlantic Water

MCM   mine countermeasures

MODAS   Modular Ocean Data Assimilation System

NODC   National Oceanographic Data Center

NL   noise level

NOVA   National Oceanic Atmospheric Administration

OSD   optimal spectral decomposition

PC   principal component

PD   periscope depth

SL   source level

SMG-WOD   synoptic monthly gridded-world ocean database

SSP   sound speed profile

SSS   sea surface salinity

SST   sea surface temperature

WOD13   World Ocean Database 2013

TL   transmission loss

TS	target strength
USW	undersea warfare
XBT	expendable bathythermograph

ACKNOWLEDGMENTS

I would first like to thank my thesis advisor, Professor Peter C. Chu, a passionate scientist, for his intellectual contribution to my thesis.

I would like to thank my co-advisor, Dr. Tetyana Margolina, a talented scientist, not only for her time but also for her patience.

Finally, I would like to express appreciation to my program officer, CDR Paulo Travis, for supporting me greatly through my education.

THIS PAGE INTENTIONALLY LEFT BLANK

I. INTRODUCTION

The Mediterranean Sea is an important area to research for the navy's tactical issues, especially given its historical importance and its position surrounded by NATO countries. Chapter I defines the basic structure of the Mediterranean Sea and the objective of this thesis to highlight the relevance of the inter-annual variability of sound propagation.

A. THE MEDITERRANEAN SEA

The word Mediterranean derives from the Latin *medius terrae*, meaning "inland." Surrounded by the continents of Europe, Asia, and Africa, the Mediterranean is an intercontinental sea extending from the Atlantic Ocean to the Middle East, separating Europe from Africa (Tanabe 2013). Its major subdivisions from west to east include the Balearic, Ligurian, Tyrrhenian, Adriatic, Ionian, and Aegean Seas. Figure 1 shows countries that border the Mediterranean Sea.

Figure 1. The Mediterranean Sea, Bordering Countries, and Subdivisions. Adapted from WorldAtlas (2016).

B.   GEOGRAPHY

The overall length of the Mediterranean Sea basin is 3,860 kilometers, and the utmost width is 1,600 kilometers. The Strait of Gibraltar connects the Mediterranean Sea to the Atlantic Ocean. The depth of the Strait of Gibraltar varies between 300 and 900 meters. Deep basins of the Mediterranean Sea are well connected to one another; however, the Black Sea and the Aegean Sea are connected only by a very narrow strait (Office of Ocean Exploration and Research 2001). The Mediterranean Sea consists of two main sub-basins: the Western Mediterranean and the Eastern Mediterranean. The Western Mediterranean Basin lies between the Strait of Gibraltar and the Strait of Sicily. As described by Alhammoud et al. (2005), the Eastern Mediterranean basin lies to the east of the Strait of Sicily (~150 km wide and ~600 m deep), and consists of important regional seas: the Ionian, Levantine, Adriatic, and Aegean Seas. The maximum depths are approximately 3400 meters in the Western Basin and 4200 meters in the Levantine Sea, separated by the Strait of Sicily, which is roughly 430 meters deep (Reddy 2001).

Both basins include many regional seas and straits. As for regional seas, the Alboran, Balearic, and Ligurian Seas are within the Western Mediterranean. The Tyrrhenian, Ionian, Adriatic, and Aegean Seas are within the Eastern Mediterranean. Figure 2 shows individual seas that make up the Mediterranean.

Figure 2.   Individual Seas that Make Up the Mediterranean Sea. Adapted
from World Facts Inc. (2016).

C.   THESIS OBJECTIVE

The Mediterranean Sea has been extensively studied as this region is of operational significance to the U.S. Navy. Effective undersea warfare (USW) operations such as anti-submarine warfare (ASW), undersea warfare (USW), and mine countermeasures (MCM) require a clear understanding of how sound propagates through the water. Therefore, the North Atlantic Treaty Organization (NATO) gives priority to improved understanding of ocean acoustics as a means to maintain a tactical advantage in the Mediterranean Sea.

In recent years, NATO–Russian tensions have risen, particularly in the Eastern Mediterranean, due to the development of a Russian naval base in Syria's Tartus port. Because Turkey has the longest coastline in the Eastern Mediterranean Sea among NATO members, those tensions put Turkey in a more delicate situation.

For this reason, depth characterization of acoustic transmission loss in the Mediterranean Sea is of vital importance and requires more in-depth study. This thesis aims to acquire operationally important results for ASW by performing a detailed analysis of variations in temperature, salinity, and sound speed in the region to examine

inter-annual variability of sound propagation. This study focuses on data collected in the Mediterranean Sea from January 1960 to December 2014.

D. THESIS ORGANIZATION

Some significant aspects of the Mediterranean Sea oceanography are explained in Chapter II including external forcing, thermohaline circulation, and inter-annual variability. The data, which include bathymetry and sediment databases, geoacoustics parameters, the synoptic monthly gridded–world ocean database (SMG-WOD), and the generalized digital environmental model (GDEM), are described in Chapter III. Chapter IV contains the methods used in this study. Chapter V describes and compares seasonal variability of spice and sound speed fields in the synoptic monthly data with GDEM. Chapter VI contains discussion of the interannual variability of temperature, salinity and sound speed, and associated acoustic propagation patterns. Chapter VII summarized research findings as well as identifies new areas for research within the Mediterranean Sea.

II. OCEANOGRAPHY OF THE MEDITERRANEAN SEA

The oceanography of the Mediterranean Sea is unique. It can be characterized by very high salinity, temperature, and spiciness. This chapter explains the external forcing, and its effects on the thermohaline circulation, water masses, and sound propagation, and especially the intra-seasonal and inter-annual variability.

A. EXTERNAL FORCING

The Mediterranean Sea is a useful example of influence of air-sea interaction or external forcing on the local circulation patterns and thermal structure over the water column. It is an evaporative basin with an estimated freshwater (evaporation-precipitation-river runoff = net evaporation) loss of 50 to 100 centimeter (cm) per year (Bethoux 1979; Bryden and Kinder 1991). For this reason, the Mediterranean Sea is a concentration basin on average.

The Mediterranean Sea region has very hot and dry summers, which results in a high rate of water evaporation. During most of the year, the Mediterranean Sea is also affected by winds from the northwest carrying warm and dry air. Evaporation from these winds also results in a net loss of fresh water, as has dam placement along the Nile River. The Diversion of Nile River discharge has caused the salinity of the Mediterranean Sea to increase by about 0.04 over a time scale of 40 years (Borghini et al. 2014).

B. THERMOHALINE CIRCULATION

Thermohaline circulation is a term used to describe the movement of water in the ocean in response to changes of temperature and salinity. These two properties affect the density of water. There is a high-density difference between the Atlantic Ocean and the Mediterranean Sea, and this density variation creates a thermohaline circulation between them, which is the case for oceans all over the world (Topper and Meijer 2015). The Strait of Gibraltar drives the circulation because it connects the Atlantic Ocean with the Mediterranean Sea (Béranger et al. 2005). The water that inflows from the Atlantic Ocean is less dense in the upper layer through the Strait of Gibraltar. The denser Western Mediterranean water outflows to the Atlantic Ocean under the inflowing Atlantic water.

This saltier and denser water in the Western Mediterranean Sea also plays an important role in the thermohaline structure in the Atlantic Ocean.

A strong seasonal thermocline occurs in the Mediterranean Sea due to significant evaporation in the summer. Most of the Mediterranean's annual evaporation surpasses river runoff and rainfall (Borghini et al. 2014). Nevertheless, the Adriatic Sea is one exception. It receives a large amount of fresh water from the Po River.

Seasonal variations of temperature and salinity also drive the circulation in the Mediterranean Sea. The Eastern Mediterranean is exposed to more evaporation than the Western Mediterranean. Thus, the Modified Atlantic Water enters the Eastern Mediterranean Sea to compensate the loss of water in the Eastern Mediterranean Sea. Conversely, Levantine Intermediate Water, which is saltier and warmer than the Modified Atlantic Water, enters the Western Mediterranean Sea as the deeper layer in the Strait of Gibraltar (Artale et al. 2002). Figure 3 demonstrates the thermohaline circulation in the Mediterranean Sea.
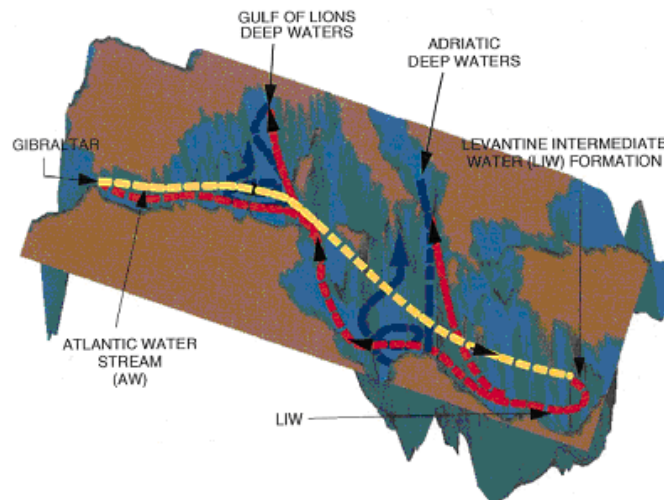
Figure 3.   The Schematic of Thermohaline Circulation in the
Mediterranean Sea. Source: European Ocean Observatory
Network (2000).

C.   WATER MASSES

There are four fundamental water masses in the Mediterranean Sea: Modified Atlantic Water, Levantine Intermediate Water, East Mediterranean Deep Water, and Levantine Surface Water. Figure 4 depicts the vertical distribution of the Mediterranean's water masses.
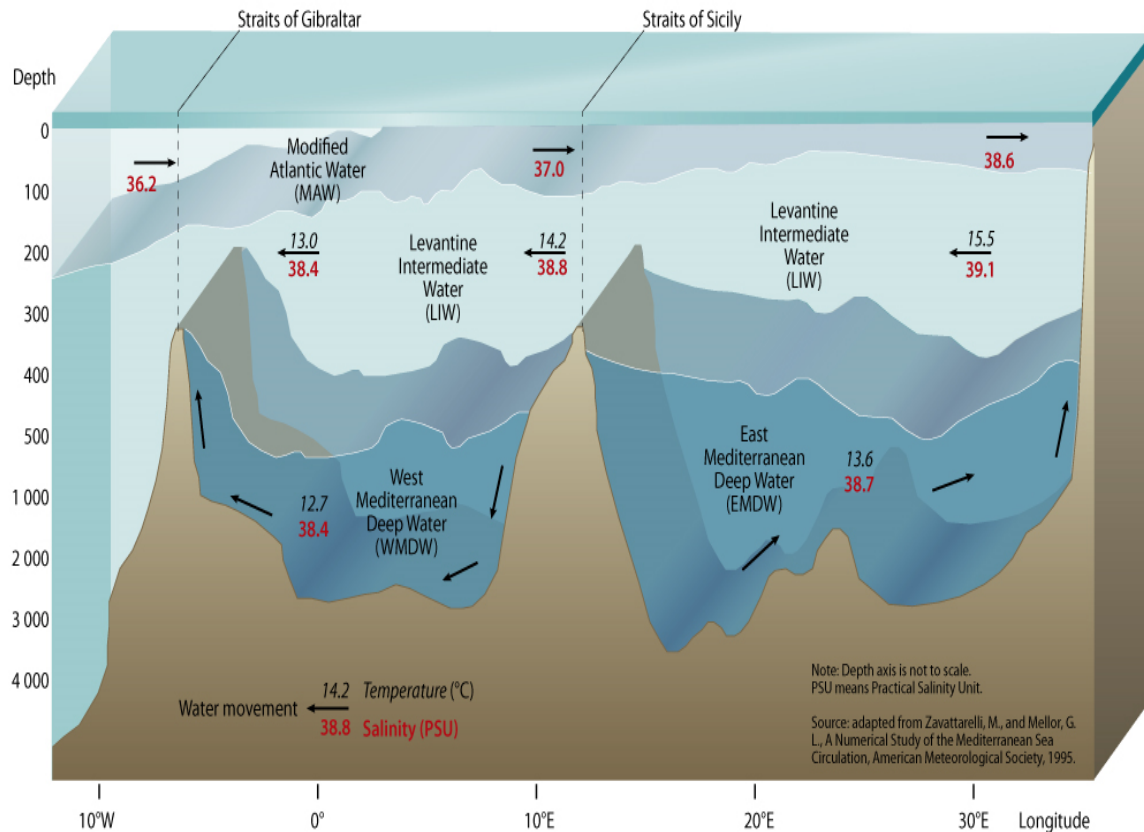
Figure 4.   Mediterranean Sea Vertical Distribution of Water Masses.
Source: GRID-Arendal (2013).

1. Modified Atlantic Water (MAW)

Robinson et al. (2001) show that the flow between the Atlantic Ocean and the Mediterranean Sea depends primarily on the density difference between two important water masses: the Modified Atlantic Water (MAW) and the Levantine Intermediate Water (LIW). From the data, we found that the MAW is less dense than the LIW. Thus, the less dense MAW flows in the upper part of the Strait of Gibraltar. The denser LIW flows out in the deep layer of the Strait of Sicily and reaches the Strait of Gibraltar. It also flows out in the deep layer of the Strait of Gibraltar. These two important water masses adjust the mass transportation (Robinson et al. 2001). Figure 5 demonstrates currents in the Strait of Gibraltar.
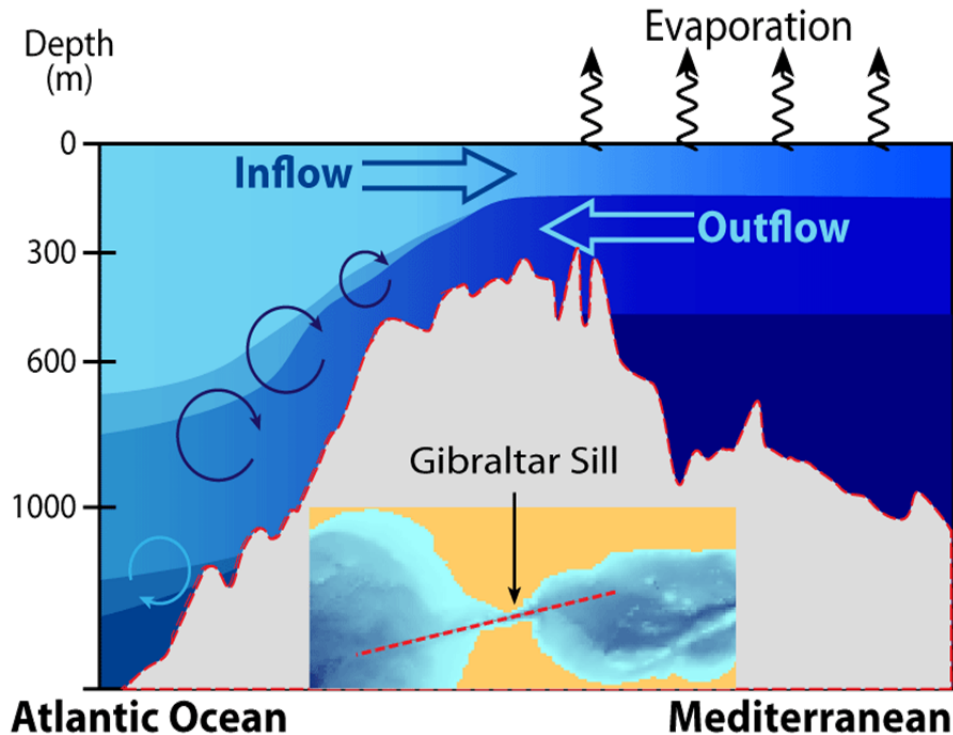
Figure 5.   Currents in the Strait of Gibraltar.
Source: National Oceanography Centre Southampton (2015).

The Modified Atlantic Water is generally distinguished as having a minimum subsurface salinity of ~38.6 in depths of 30 to 200 m. Its salinity increases and its depth

8

range decreases as it flows eastward as a result of high evaporation (Alhammoud et al. 2005). Figure 6 presents the mean salinity on the surface from 1945 to 2014.
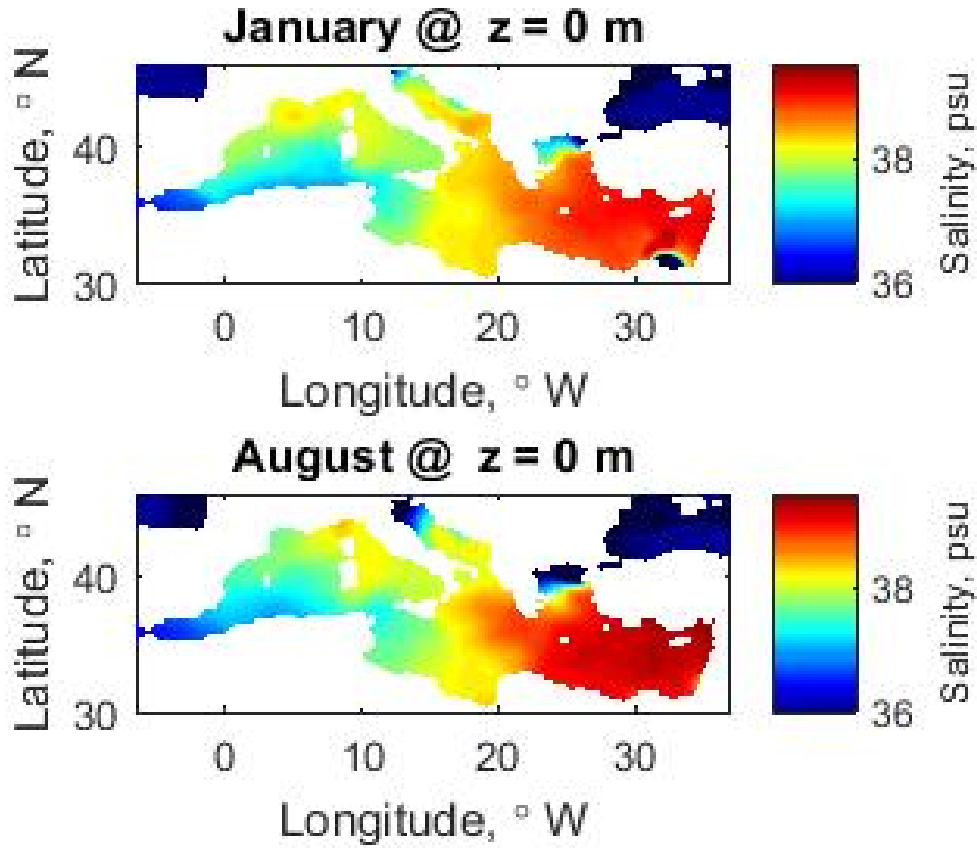
Figure 6.   Mean Salinity at the Surface from GDEM database

Figure 6 shows that the Modified Atlantic Water is concentrated in the south region of the Western Mediterranean Sea in a narrow, long line. It flows along the Algerian Coast to the Strait of Sicily. Its mean salinity is about 36 psu at the Strait of Gibraltar and increases as it flows eastward.

2.   Levantine Intermediate Water (LIW)

Another essential water mass in the Mediterranean Sea is the Levantine Intermediate Water (LIW). Citing Tchernia 1980, Ozsoy et al. 1989, and Ozsoy et al. 1993, Alhammoud et al. (2005) provide a comprehensive description of the LIW:

"A homogenous water mass occupies the intermediate depth between 300 and 700 m, below the AW. It is well known that this water mass is formed in winter in the LB by the transformation of AW. The LIW signature is characterized by the highest sub-surface salinity (38.8–39.0 psu) in the LB. As LIW flows westward, its salinity decreases due to the mixing with the adjacent water masses" (p. 9).

Figure 7 shows the LIW in August, and Figure 8 shows the LIW in January. The density of the LIW varies between 28.95 and 29.10 $\frac{kg}{m^3}$.
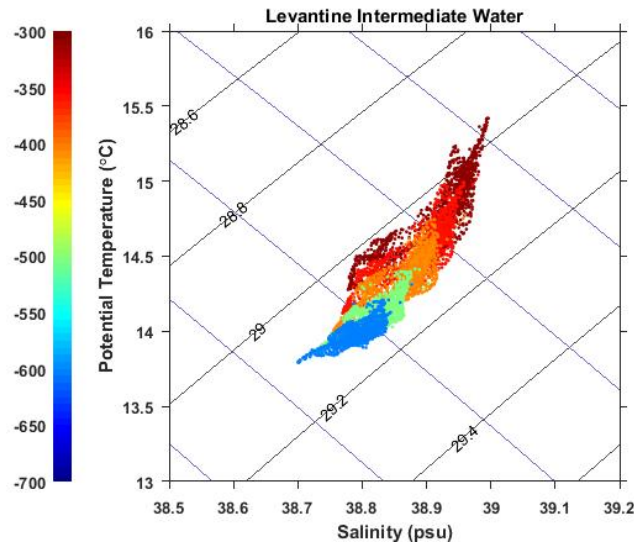
Figure 7.   LIW T-S Diagram in August from the GDEM database
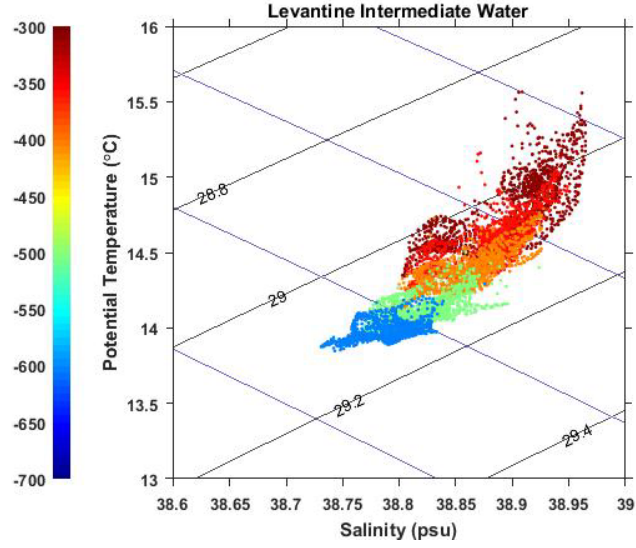
Figure 8.   LIW T-S Diagram in January from the GDEM database

3.   Eastern Mediterranean Deep Water (EMDW)

The third water mass affecting the Mediterranean, the Eastern Mediterranean Deep Water (EMDW), is identified as having salinity of 38.7 psu and temperature of 13.8°C at depths greater than 800 m. It is formed in the Adriatic and Aegean Seas in the Levantine Basin due to strong cooling (Alhammoud et al. 2005). The density remains between 29.05 and 29.10 $\frac{kg}{m^3}$. Figure 9 shows the EMDW in August, and Figure 10 shows the EMDW in January.

11
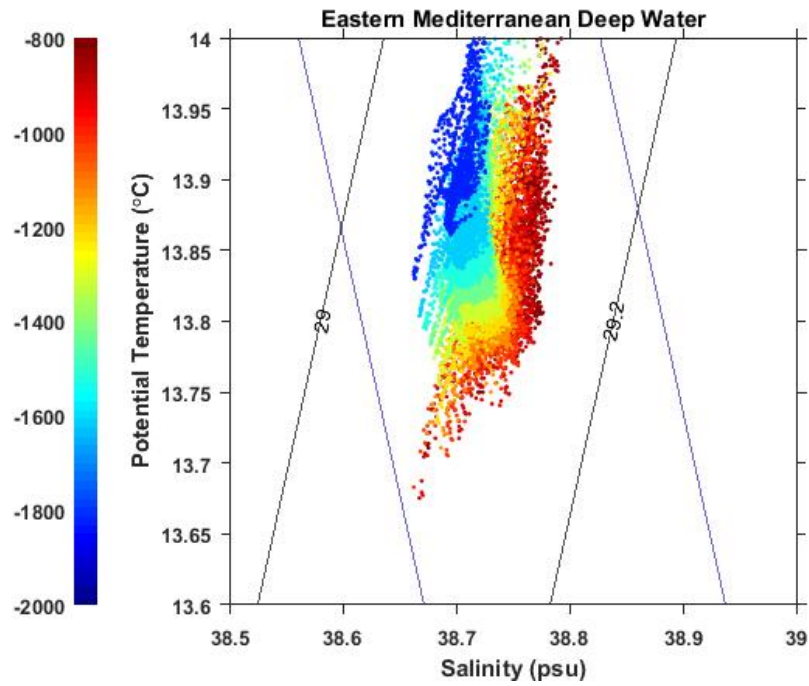
Figure 9.   Eastern Mediterranean Deep Water T-S Diagram in August
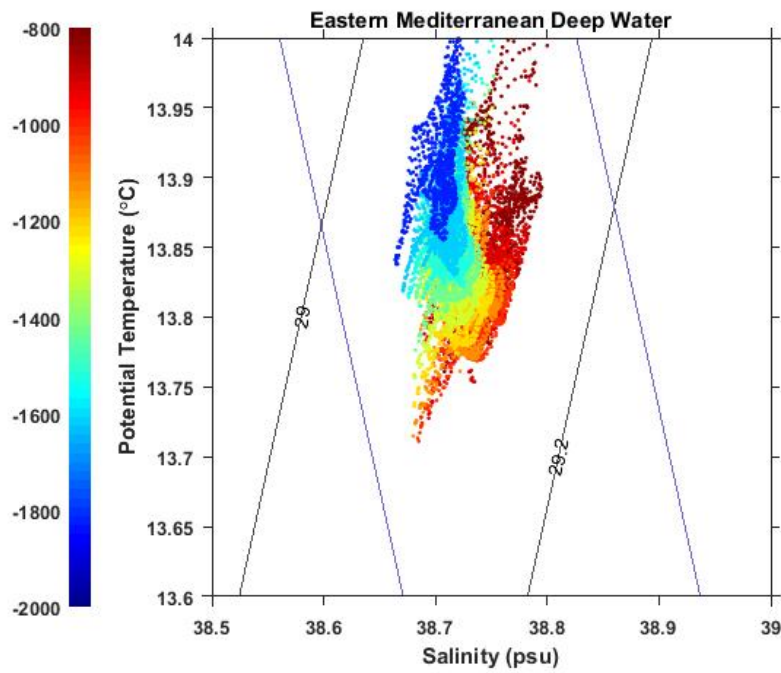
Figure 10.   Eastern Mediterranean Deep Water T-S Diagram in January

4. Levantine Surface Water (LSW)

Another water mass, the Levantine Surface Water (LSW), is thin, warm, and salty. It resides over the surface of the Levantine basin. It forms particularly in summer because of the high rate of evaporation (Alhammoud et al. 2005). It floats over the MAW. We found that the LSW is the saltiest and warmest water mass among all others in the Mediterranean Sea (see Figure 11).
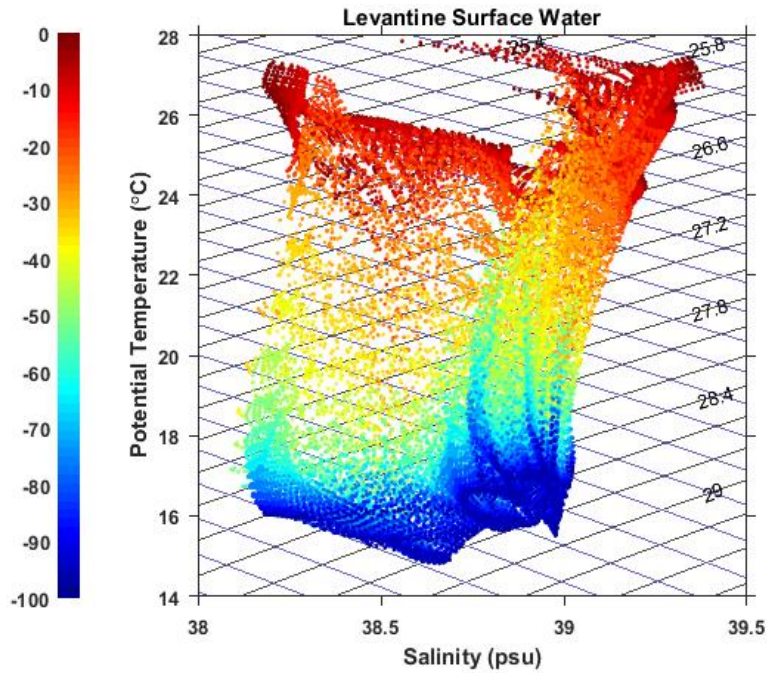
Figure 11.   Levantine Surface Water in August

THIS PAGE INTENTIONALLY LEFT BLANK

III. DATA

Chapter II explained the different forces acting on the Mediterranean Sea. This chapter shows how the four environmental datasets were utilized into an acoustic model to study the inter-annual acoustic variability (Allen and U.S. Navy 2012, Chu and Fan 2016b, NAVO 2006, NAVO 2009, and Porter 2011): sediment, bathymetry, SMG-WOD and GDEM salinity and temperature data.

A.   SEDIMENT DATABASE

The Naval Oceanographic Office (NAVO) has four open sediment databases: enhanced, standard, reduced, and High-Frequency Environmental Acoustics (HFEVA). The enhanced database is the actual database, which NAVO maintains. The other three sediment databases are rearranged from this data source.

The HFEVA sediment database has 23 standard types based on sediment mixture and grain-size. There are two uncommon numbers, 888 alluding to "no data" and "999" alluding to land. Table 1 shows the HFEVA sediment types. See Appendix A for a complete sediment list.

The HFEVA dataset is derived for high-frequency acoustic performance prediction (NAVO 2003). The 23 sediment types are transformed into a set of three geoacoustic parameters for the BELLHOP acoustic model.

.

Table 1.   HFEVA Sediment Categories. Source: NAVO (2006).

HFEVA Standard Sediment Type	HFEVA Category
Rough Rock	1
Rock	2
Cobble or Gravel or Pebble	3
Sandy Gravel	4
Very Coarse Sand	5
Muddy Sandy	6
Gravel Coarse Sand or Gravelly Sand	7
Gravelly Muddy Sand	8
Medium Sand or Sand	9
Muddy Gravel	10
Fine Sand or Silty Sand	11
Muddy Sand	12
Very Fine Sand	13
Clayey Sand	14
Coarse Silt	15
Gravelly Mud or Sandy Silt	16
Medium Silt or Sand-Silt-Clay	17
Sandy Mud or Silt	18
Fine Silt or Clayey Silt	19
Sandy Clay	20
Very Fine Silt	21
Silty Clay	22
Clay	23
No data	888
Land	999

B.   BATHYMETRY DATABASE

We extracted bathymetry data for the Mediterranean Sea from the NAVO Digital Bathymetric Database-Variable resolution (DBDB-V) version 5.4. There are three accessible database levels of DBDB-V. We used Level 0, which is unclassified, for this research. The DBDB-V is a fine-scale database due to four resolutions of bathymetry data: in arc minutes of 2', 1', 0.5', or 0.1'. The two-minute arc grid had been generated by aggregating data from different freely accessible sources in 2004, and it is the main resolution that presents complete global coverage (McDonald 2016). This search uses a 2' resolution.

C.   GEOACOUSTIC PARAMETERS

The geoacoustic parameters are obtained to compute attenuation and sound speed in the bottom sediments. There are three main geoacoustic parameters used as a part of the present research: sediment density, the attenuation coefficient, and the compressional sound speed. The attenuation coefficient values for all bottom sediments in the region of interest were obtained from (Hamilton 1980). Table 2 provides the other parameters.

Table 2.   Geoacoustic Parameters Index. Source: Cintron (2001).

Bottom Sediment Composition	Bulk Grain Size Index	Long (32 Char) Name	Density gm/cm^3	Sound Speed Ratio	Wave Number Ratio
BOULDER	-9	Rough Rock	2.5	2.5	0.0137
ROCK	-7	Rock	2.5	2.5	0.0137
GRAVEL	-3	Grave, Cobble or Pebble	2.5	1.8	0.0137
	-1	Sandy Gravel	2.492	1.337	0.01705
	-0.5	Very Coarse Sand	2.401	1.3067	0.01667
	0.0	Muddy Sand Gravel	2.314	1.2778	0.01630
	0.5	Coarse Sand	2.231	1.2503	0.01638
	1.0	Gravelly Muddy Sand	2.151	1.2241	0.01645
SAND	1.5	Sand or Medium Sand	1.845	1.1782	0.01624
	2.0	Muddy Gravel	1.615	1.1396	0.01610
	2.5	Silty Sand or Fine Sand	1.451	1.1073	0.01602
	3.0	Muddy Sand	1.339	1.0800	0.01728
	3.5	Very Fine Sand	1.268	1.0568	0.01875
	4.0	Clayey Sand	1.224	1.0364	0.02019
	4.5	Coarse Sand	1.195	1.0179	0.02158
	5.0	Sandy Silt	1.169	0.9999	0.01261
	5.5	Medium Silt	1.149	0.9885	0.00676
SILT	6.0	Silt	1.148	0.9873	0.00386
	6.5	Fine Silt	1.147	0.9861	0.00306
MUD	7.0	Sandy Clay	1.147	0.9849	0.00242
	7.5	Very Fine Silt	1.146	0.9837	0.00194
	8.0	Silty Clay	1.145	0.9824	0.00163
CLAY	9.0	Clay	1.145	0.9800	0.00148
	10.0		1.145	0.9800	0.00148

D.   GDEM

The GDEM provides monthly climatological fields of temperature and salinity. Carnes (2004) states, "Development of GDEM at the Naval Oceanographic Office began in 1975 and culminated in the first release to the Navy community in 1984. The first release contained only the North Atlantic Region, but by 1991 most of the world's oceans were included." The early form of the GDEM had a few restrictions in regions where the depth was shallower than 100 meters. In this manner, the main adaptation of GDEM did not make a difference between the shallow and waterfront waters. At that point, GDEM-V 2.6 was enhanced by another procedure to empower to deliver vertical profiles in regions where bottom depths are 5 meters. Although GDEM-V 2.6 demonstrated better results in shallow waters, it had a few problems capturing salinity and temperature vertical profiles in some region of the world's oceans.

GDEM-V 3.0, the current working version, has been utilized as a part of the present research. GDEM3 was derived from temperature and salinity profiles extracted from the Master Oceanographic Observational Data Set (MOODS) in 1995. Staff at the Naval Research Laboratory (NRL) altered the profiles and afterward used them to build the climatology of the Modular Ocean Data Assimilation System (MODAS) by Fox et al. (2001–2002). Carnes states,

> GDEM profiles were interpolated by the method of the weighted parabolas to create 78 standard depths starting from the surface 0m and going down to 6600m. It has a horizontal resolution of 0.25. The gridded of the temperature, salinity, temperature variance, and salinity variance was performed separately at each of the 78 depth levels.

However, GDEM is not an open source as it is open only to the U.S. military and its members.

E.   SMG-WOD

Four-dimensional (4D) SMG-WOD was produced from the NOAA WOD13 at NPS using the optimal spectral decomposition (OSD) method Chu and Fan (2016), and provides 4D world ocean gridded temperature and salinity data, from January 1945 to December 2014, its spatial bounding box coordinates are limited to 180E–180W and 80N–80S.

The WOD13 database contains a "collection of scientifically quality-controlled ocean profile and plankton data that includes measurements of temperature, salinity, oxygen, phosphate, nitrate, silicate, chlorophyll, alkalinity, pH, pCO2, TCO2, Tritium, Δ13Carbon, Δ14Carbon, Δ18Oxygen, Freons, Helium, Δ3Helium, Neon, and plankton" (Boyer et al. 2013). Table 3 provides the WOD13 datasets and the instrument sources that contributed data.

As a part of ocean investigation, we utilized the OSD-technique, which proved fruitful in drawing out an ocean phenomenon that had not documented previously (see Chu et al. 2005; Chu et al. 2007; and Chu 2011) and might be utilized as part of ocean data assimilation (Chu et al. 2015). This method makes use of the geography and lateral boundary conditions but is different from past interpolation methods, for instance, optimal interpolation (OI) because it does not require a foundation error covariance matrix (Chu and Fan 2016a). Table 4 presents the vertical levels of the SMG-WOD data (Chu et al. 2003a; 2003b; 2004; and 2015), which is now publicly accessible at the National Oceanic and Atmospheric Association (NOAA) and the National Centers for Environmental Information (NCEI) website (Chu and Fan 2016). The SMG-WOD data for the Mediterranean Sea region has higher horizontal (0.25°) and vertical (57 levels) resolution, and covers the period 1960–2014.

Table 3.   Datasets and the Instruments Sources Contribute Data.
Source: Boyer et al. (2013).

DATASET	SOURCE
OSD	Bottle, low-resolution Conductivity-Temperature-Depth (CTD), low-resolution XCTD data, and plankton data
CTD	High-resolution Conductivity-Temperature-Depth (CTD) data and high-resolution XCDT data
MBT	Mechanical Bathythermograph (MBT) data, DBT, micro-BT
XBT	Expendable (XBT) data
SUR	Surface only data (bucket, thermosalinograph)
APB	Autonomous Pinniped Bathythermograph – Time- Temperature-Depth recorders attached to elephant seals
MRB	Moored buoy data from TAO (Tropical Atmosphere-Ocean), PIRATA (moored array in the tropical Atlantic). MARNET, and TRITON (Japan-JAMSTEC)
PFL	Profiling float data
DRB	Drifting buoy data from surface buoys with thermistor chains
UOR	Undulating Oceanographic Recorder data from a Conductivity/Temperature/Depth probe mounted on a towed undulating vehicle
GLD	Glider data

Table 4.   SMG-WOD Depth Layers. Source: Rodriguez (2016).

Level	Depth (m)	Level	Depth (m)	Level	Depth (m)
1	0	11	250	21	1200
2	10	12	300	22	1300
3	20	13	400	23	1400
4	30	14	500	24	1500
5	50	15	600	25	1750
6	75	16	700	26	2000
7	100	17	800	27	2500
8	125	18	900	28	3000
9	150	19	1000		
10	200	20	1100		

IV. METHODS

Chapter IV explains the methodology including the composite analysis, acoustic modeling using BELLHOP, choice of reference points based on bottom sediment type, calculation of spiciness and quantifying uncertainty in the transmission loss.

A. COMPOSITE ANALYSIS

From the SMG-WOD gridded dataset, the sound speed (c) profiles are calculated from the (T, S) profiles. At a specific horizontal grid, it is represented by $c(z_i, \tau_k, t_l)$, with z_i represents the vertical levels; $i = 1, 2, \ldots, I$, where I (= 28) is the total number of the vertical levels; τ_k = 1960, 1961, ..., 2014 is the time sequence in years; and $t_l = 1, 2, \ldots, 12$ is the monthly sequence within a year.

Two Temporal Means

Before investigating the annual variation of c, we define the following two temporal averages:

$$\overline{c}(z_i, t_l) = \frac{1}{\Delta\tau} \sum_k c(z_i, \tau_k, t_l), \quad \Delta\tau = 55 \ (1960 \text{ to } 2014), \qquad (4.1)$$

which are the multiyear averaged mean values, and

$$\overline{\overline{c}}(z_i) = \frac{1}{12} \sum_{l=1}^{12} \overline{c}(z_i, t_l), \qquad (4.2)$$

which is the total-time mean.

Mean Seasonal Variability

The annual mean values deviated from the total-time mean, $\overline{\overline{c}}(z_i)$,

$$\tilde{c}(z_i, t_l) = \overline{c}(z_i, t_l) - \overline{\overline{c}}(z_i), \qquad (4.3)$$

lead to composite features of the mean seasonal variability.

Interannual Variability

The deviation from its annual mean value

$$\hat{c}(z_i, \tau_k, t_l) = c(z_i, \tau_k, t_l) - \overline{c}(z_i, t_l), \qquad (4.4)$$

Is called the anomaly data, which is re-arranged into a I×P matrix, $\hat{c}(z_i, \tilde{t}_p)$, p = 1, 2, …,

P. Here P = 660 is the total number of months (i.e., total time points). The empirical

orthogonal function (EOF) analysis (Chu et al., 1998; Chu 2010) was conducted on the

anomaly data

$$\hat{c}(z_i, \tilde{t}_p) = \sum_j PC_j(\tilde{t}_p) E_j(z_i), \qquad (4.5)$$

where $E_j(z_i)$ is the jth EOF mode with the unit of m/s; and $PC_j(\tilde{t}_p)$ is the jth principal

component without unit. Here, j = 1, 2, …, J; J is truncated number of the EOF modes.

B.   BELLHOP

BELLHOP was used in this present research in order to predict transmission loss
for acoustic popagation in the Mediterranean Sea. Porter (2011) states, "BELLHOP can
produce a variety of useful outputs including transmission loss, eigenrays, arrivals, and
received time series. It allows for range-dependence in the top and bottom boundaries
(altimetry and bathymetry), as well as in the sound-speed profile." The sound speed
profiles uploaded into BELLHOP were created by the GDEM and SMG-WOD for
comparison. BELLHOP is a program that can be used on many platforms. In this present
research, BELLHOP is used in MATLAB.

BELLHOP creates a two-dimensional ray that traces plots for the given sound-
speed profiles and bottom sediment. Although the Mediterranean Sea is not shallow, its
mean depth falls below the mean for all global oceans. Additionally, it has very shallow
waters in some crucial areas for NATO operations.

There are many reasons why we preferred BELLHOP in the present research. First, it is an open-source program and can be used internationally. Second, modeling acoustic transmissions with rays is a common method for studying and understanding how sound energy propagates through a given sound channel (Porter 2011).

Bottom sediment types exhibit different parameters in the calculation. Each bottom sediment provides a different bottom reflection coefficient. In order to analyze bottom sediment effects on sound propagation, different bottom sediments were taken into account. The calculation for transmission loss is shown in Equation (4.6)

$$TL = -10log\frac{I(r,z)}{I_O}$$

$$= -20\log\frac{[p(r,z)]}{[p0]} \qquad \text{(db re 1 m)} \qquad (4.6)$$

There are three different ways to plot in BELLHOP. They are: coherent, incoherent and semi-coherent. The user selects one depending on the level of interference. For example, if a user wants to calculate fine-patterned interference in the transmission loss, the coherent mode is required. Otherwise, the user may select the incoherent mode. Semi-coherent transmission loss is a combination of coherent and incoherent. It calculates some interference but not as much as the coherent mode (McDonald 2016). Figure 12 demonstrates the BELLHOP structure.
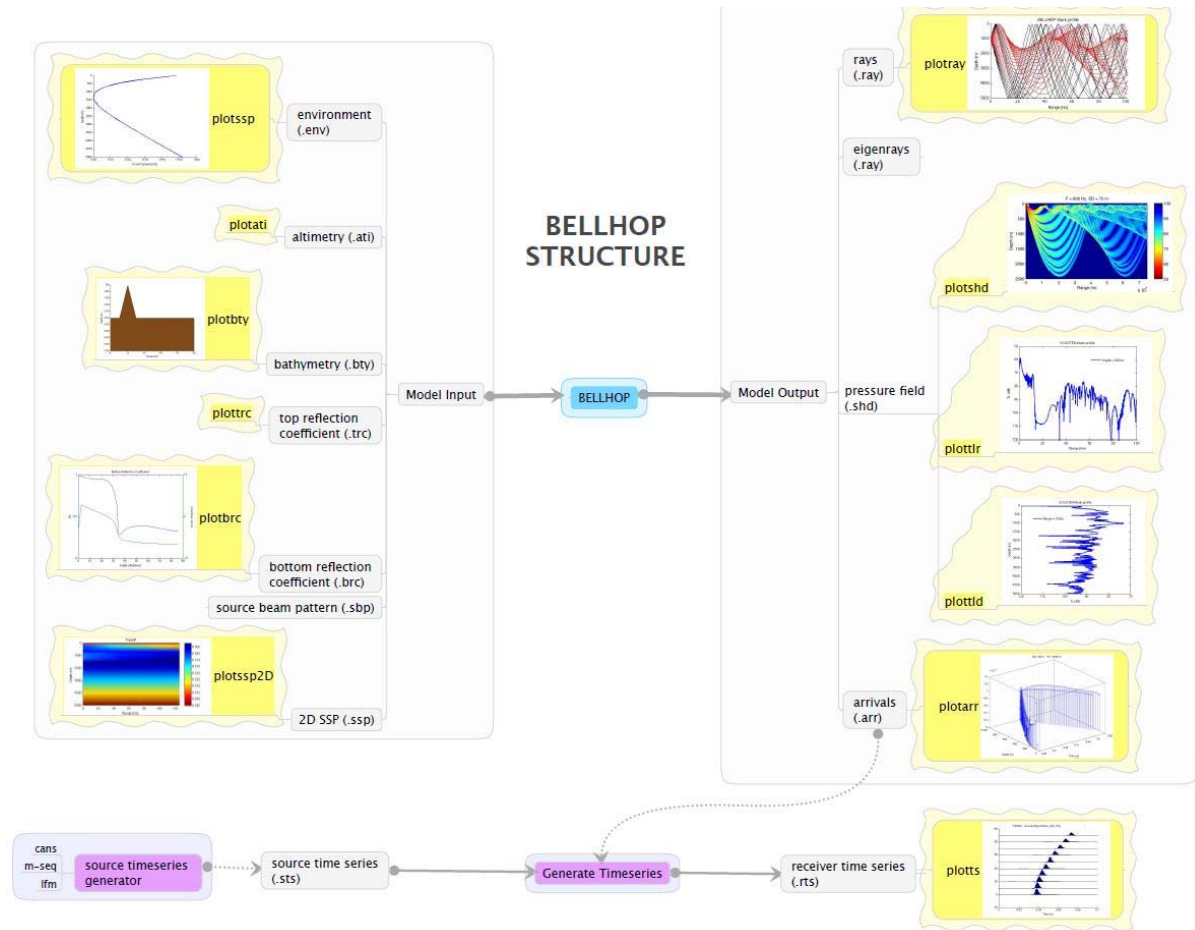
The left side of the figure exhibits all the inputs that can be uploaded into BELLHOP.
The right side of figure represents model outputs.

Figure 12. BELLHOP Structure

BELLHOP transmission losses were plotted for a source depth of 40 meters and various receiver depths. The results are explained in Chapter V.

C.   TREATMENT OF BOTTOM SEDIMENTS

The effects of bottom sediment on transmission loss depend on sound frequencies. At low frequencies, less than 10 Hz, bottom sediments parameters are required a few meters above the sea floor. At frequencies higher than 10 Hz, all sediment thicknesses and materials underlying the seafloor have to be provided. In this thesis the frequency of 3500 Hz was selected to calculate transmission loss via BELLHOP. Therefore, bottom sediments are needed due to high frequencies penetration under the seafloor. (Computational Ocean Acoustic, 2011).

The Mediterranean Sea has a variety of bottom sediment at different depths. Although the Mediterranean is not considered shallow, it is shallower than other oceans with a four-kilometer mean depth. Seafloor properties of the Mediterranean Sea were extracted and plotted in Figure 13.
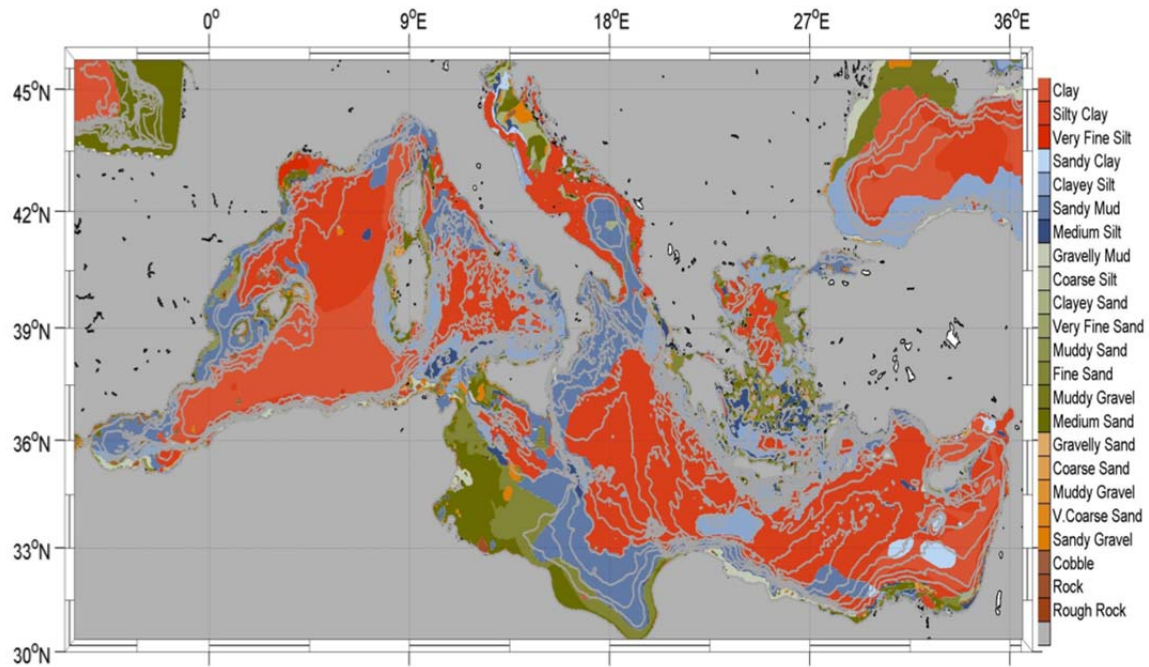
Figure 13.   Bottom Sediments and Bathymetry of the Mediterranean Sea

Five reference points were selected to model acoustic propagation in the Mediterranean Sea. Although the Mediterranean has two sub-basins, the Western Basin and Levantine Basin, some authors classify the water masses into western, central, and Levantine. Points, labeled A through E, have been selected for these water masses as shown in Table 5.

Table 5.   Locations A through E by Bottom Sediment Types and Depth

Location	Latitude (N)	Longitude (E)	Depth (m)	Bottom Sediment	Region
A	33.7794	34.939	1000	clay	Eastern
B	34.2399	13.6275	200	very fine sand	Central
C	32.1361	27.9229	1000	sandy mud	Eastern
D	36	18	1000	very fine silt	Eastern
E	40.3946	1,1739	70	sandy mud	Western

D.   CALCULATION OF SPICINESS AND SOUND SPEED

Spiciness is a useful variable for characterizing the water masses at a given isopycnal surface. Flament (2002) states,

> It is simultaneously a tracer conserved by isentropic motions, and an indicator of diffusive stability. It is useful for the combined description of interleaving and double-diffusive processes at the boundary between water masses.

Potential temperature and salinity can be used to define spiciness. Positive spiciness corresponds to warm, salty water. Inversely, negative spiciness corresponds to cold, fresh water. High positive spiciness usually results from the lack of fresh water and air–sea interaction (Bindoff and McDougall 1994). The equation from Flament (1986) for computing spiciness is as follows:

$$\pi(\theta, S) = \sum_{i=0}^{5} \sum_{i=0}^{4} b_{(ij)} \theta^i (s - 35)^i \qquad (4.7)$$

Spiciness in this thesis was calculated using Flament's algorithm. See Appendix B for more information on the spiciness calculation function.

The Mediterranean Sea loses buoyancy and exhibits a stratified water column due to considerable evaporation, especially in the summer. The Levantine Surface Water (LSW) forms in summer; it is very hot and salty with positive spiciness. Figure 14 shows the spiciness of the LSW in August.

Sound speed depends on density and compressibility. Density is also related to temperature and salinity in the ocean. Medwin's equation to express sound speed is

28

provided in Equation 4.8. There are three variables: temperature (T) in Celsius, salinity (S) in ppt, and depth (z) in meters.

$$c = 1449.2 + 4.6T - 0.055T^2 + 0.00029T^3 + (1.34 - 0.01T)(S - 35) + 0.016z \quad (4.8)$$
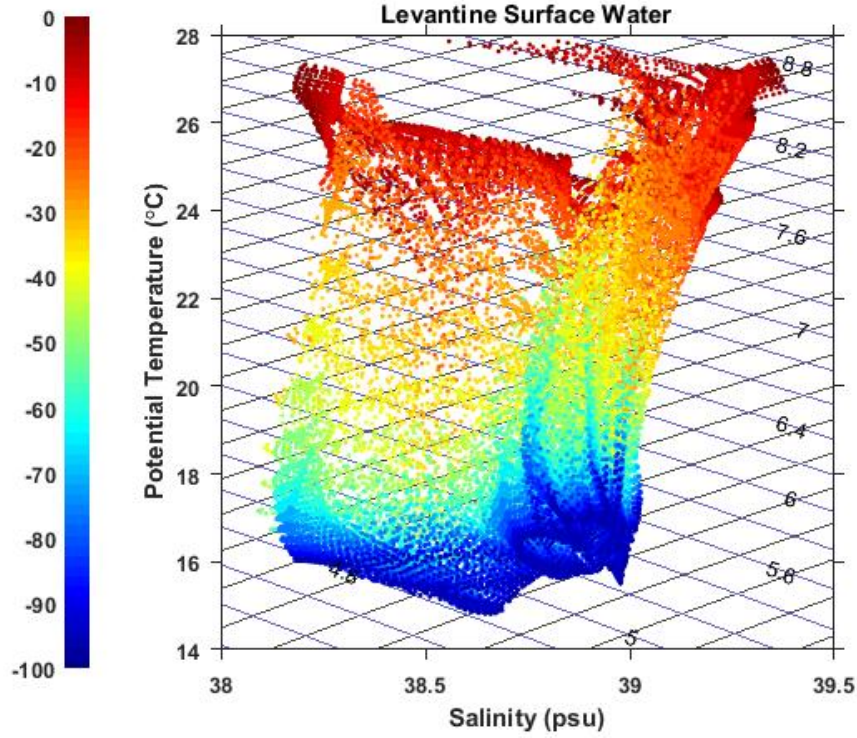
Figure 14.   Spiciness of the Levantine Surface Water in August

Equation (4.8) indicates that when temperature and salinity increase together, sound speed also increases. The increase of salinity and temperature corresponds to elevated spiciness. The vertical structure of spiciness affects the vertical structure of the sound speed.

E.   TRANSMISSION LOSS

An acoustic signal propagating in the ocean becomes distorted due to various loss mechanisms. Jensen (2011) says, "The standard measure in underwater acoustics of the change in signal strength with range is transmission loss defined as the ratio in decibels between the acoustics intensity $I(r, z)$ at a field point and the intensity I_O at 1-m distance from the source."

Low frequencies propagate further than high frequencies do. Therefore, low frequencies can be more critical for detection of submarines. The most common noise source of a submarine is the propeller. Noise produced by bubbles collapsing is called cavitation. At low speeds, machine noise often dominates the cavitation, but at intermediate and high speeds, especially when the submarine travels at periscope depths, cavitation often dominates all other noise. Cavitation depends on the operational depth and speed. Speeds that generate cavitation increase with depth (Renilson, 2015).

Researchers express the active sonar equation and calculate a signal-to-noise ratio (SNR) of possible submarines at the receiver. Equation (4.9) provides the active sonar equation.

$$SNR(decibels) = SL - 2TL + TS - (NL - AG) \qquad (4.9)$$

TL stands for transmission loss, *TS* stands for target strength, *NL* stands for the noise level, and *AG* stands for the array gain.

For this thesis, the following values for Equation (4.9) from DOSITS.org were assumed as reasonable.

SL = 220 dB; the typical array gain is 20 dB; *TS* = 25 dB; *NL* (total) is 73 dB; and a reasonable *SNR* is 22 dB. The equation can be written as follows.

$$TL = \left(\frac{1}{2}\right) * (SL - SNR\ (dB) + TS - (NL - AG)) \qquad (4.10)$$

These values depend on the type of submarine and ship, the speed, and other variables. After the above values are put into Equation (4.10), it gives

$$TL = \left(\frac{1}{2}\right) * (220 - 22 + 25 - (73 - 20)) \qquad (4.11)$$

TL= 85 dB

Therefore, values of 85 dB and below can be assumed as reasonable *TL* for detection of a submarine. The transmission loss includes sound-spreading loss and attenuation loss. We use the BELLHOP model to calculate the TL.

V. SEASONAL VARIABILITY

This chapter discusses seasonal variability of the Mediterranean Sea thermohaline structure and associated acoustic environment. First, we compare SMG-WOD multi-year monthly averaged and GDEM monthly mean fields of seawater spiciness at several horizons, which are characteristic of different water masses. Then we discuss the corresponding fields of sound speed following by discussion of sound speed profiles in several selected locations. The final subsection contains description of seasonal variability of acoustic propagation at these locations.

A.   SPICINESS

1.   SMG-WOD MULTI-YEAR MONTHLY AVERAGE

The mean spiciness in the Mediterranean Sea showed a large range of variability, both seasonally and regionally. SMG-WOD multiyear monthly average fields of spice are shown in Figure 15 for sea surface, and in Figure 16 for the depth of 100 meters. Spiciness was characterized by strong decrease from the surface to the 100 m depth, especially in August. The maximum value ($9.1\ m^3/kg$) was found at the surface of the Eastern Mediterranean Sea, decreasing with depth to about 100 meters to $5.6\ m^3/kg$ It also decreased in the Western Mediterranean Sea from $6.7\ m^3/kg$ to $4.2\ m^3/kg$ at about 100 meters. Spice did not show the same variations from the surface to the 100 meters depth in February. Maximum value ($5.6\ m^3/kg$) is found at the surface of the Eastern Mediterranean Sea, increasing with depth up to $5.8\ m^3/kg$) at 100 m. It also increases in the Western Mediterranean Sea, from $3.5\ m^3/kg$ to $3.8\ m^3/kg$ at about 100 meters. The main reason for this difference between spice variations between summer and winter seasons is the seasonal variability of temperature because of changing air-ocean heat fluxes. The surface water gets warmer during the summer season due to significant heating, and colder in the winter season due to surface cooling.

The layer between 300 meters and 700 meters in the Eastern Mediterranean is occupied by the Levantine Intermediate Water (LIW). Sometimes, LIW can extend to 800 meters. SMG-WOD multi-year monthly averaged spice at 400 m is plotted in Figure 17 to analyze the Levantine Intermediate Water.
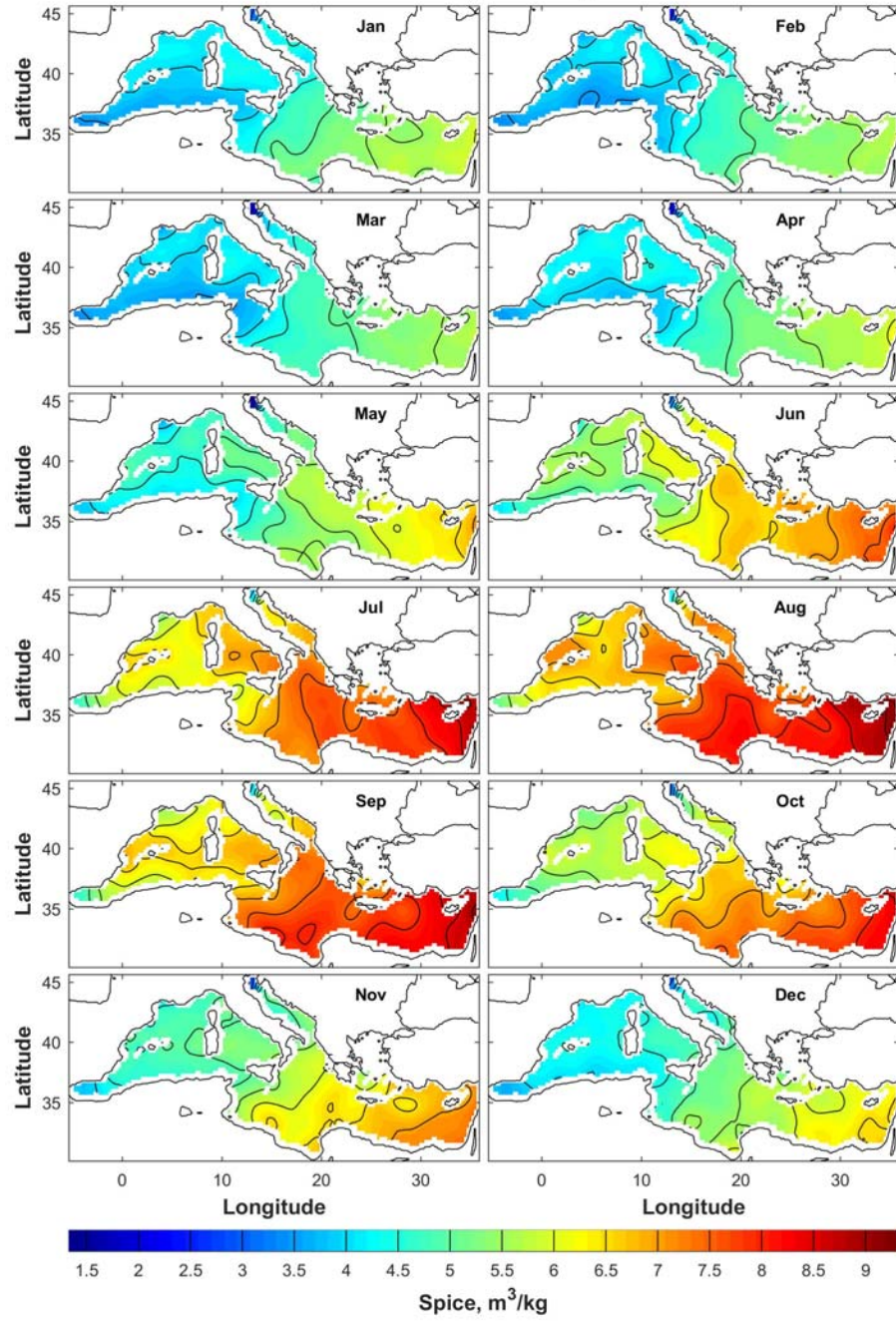
Figure 15.   SMG-WOD Multi-year Monthly Averaged Spiciness
at Zero Meters
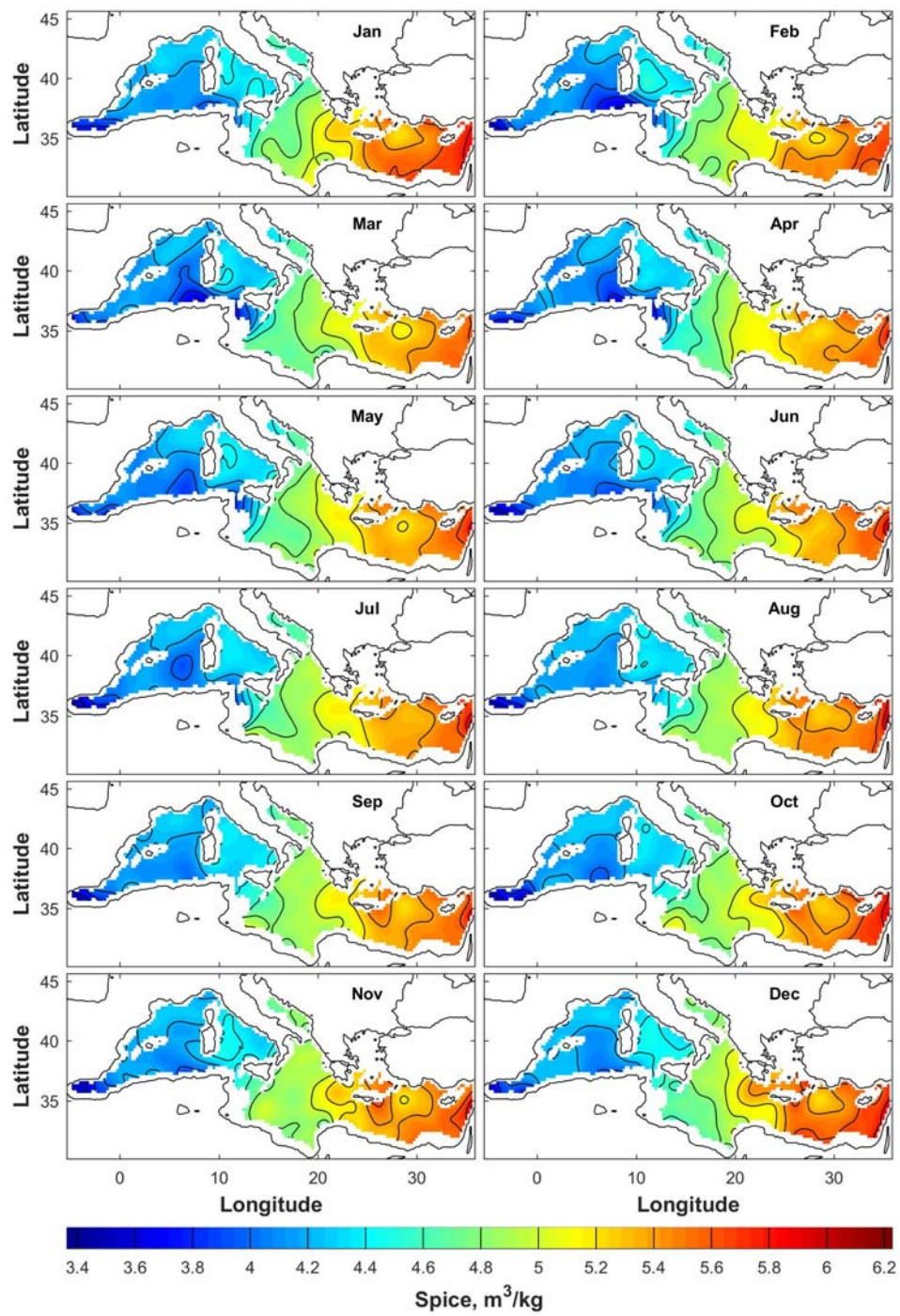
Figure 16.   SMG-WOD Multi-year Monthly Averaged Spiciness
at 100 Meters

The spice decreased significantly at the depth of 400 meters relative to the surface. Unlike the situations at the surface, the minimum values were found in August in the Eastern Mediterranean Sea. At 400 meters depth, it is approximately $4.9\ m^3/kg$. The maximum values ($5.1\ m^3/kg$) were seen in December. There were high spice values around the Crete passage where the LIW forms in winter due to strong wintertime northerlies. That finding provided a good idea of where and when the LIW forms (Millot 2013). High salinity and temperatures, or positive spiciness, are the hallmarks of the LIW.

SMG-WOD multi-year monthly averaged spice was plotted at 1050 meters to analyze the Eastern Mediterranean Deep Water (see Figure 18). The maximum value was found near the Crete Passage in March at approximately $4.82\ m^3/kg$ The minimum value was found in the southern part of the Crete Passage in June at approximately $4.56\ m^3/kg$. There was no significant difference of spice as expected in the Eastern Mediterranean Sea.

2. GDEM MONTHLY MEANS

The GDEM monthly spice fields were analyzed at the same depths was analyzed to compare it with that of the SMG-WOD model. Figures 19 and 20 show GDEM monthly spice fields at surface and at 100 meters. The maximum value ($9.1\ m^3/kg$) was found at the surface of the Eastern Mediterranean Sea, decreasing with a depth of about 100 meters to $5.5\ m^3/kg$ in August. It also increased in the Western Mediterranean Sea, from $6.3\ m^3/kg$ to $4.1\ m^3/kg$ at 100 m. There was a slight difference between two models in spice values in coastal areas, where SMG-WOD has lower resolution. The SMG-WOD corresponded well with the GDEM for deep-water values. Appendix C provides a comprehensive collection of spice figures. As expected, it was confirmed that Eastern Mediterranean was more spicy than the Western Mediterranean in all months. Additionally, the data revealed that the LWS, which forms in August, has the highest spice as compared to other water masses in the Mediterranean Sea.
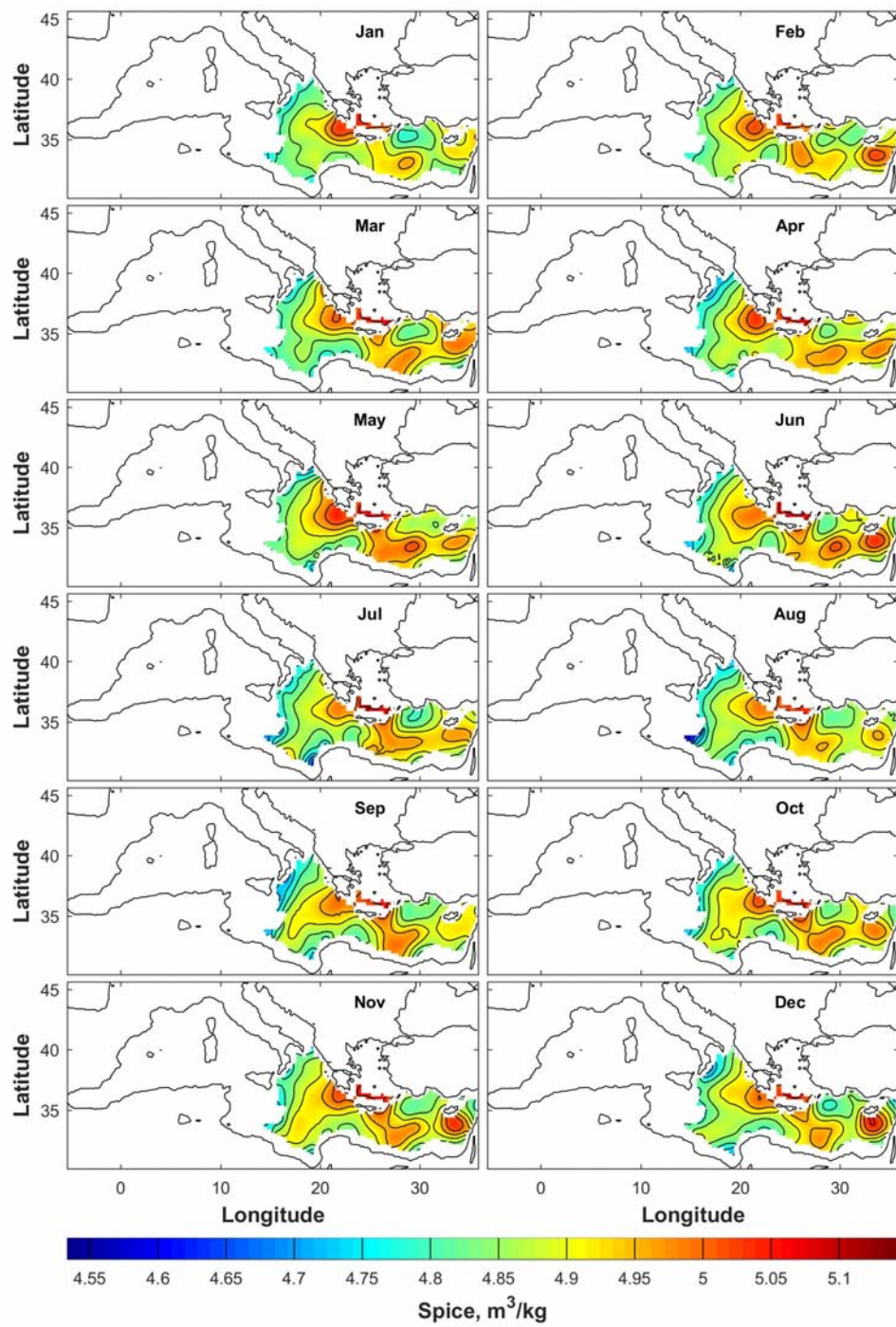
Figure 17.   SMG-WOD Multi-year Monthly Averaged Spiciness
at 400 Meters
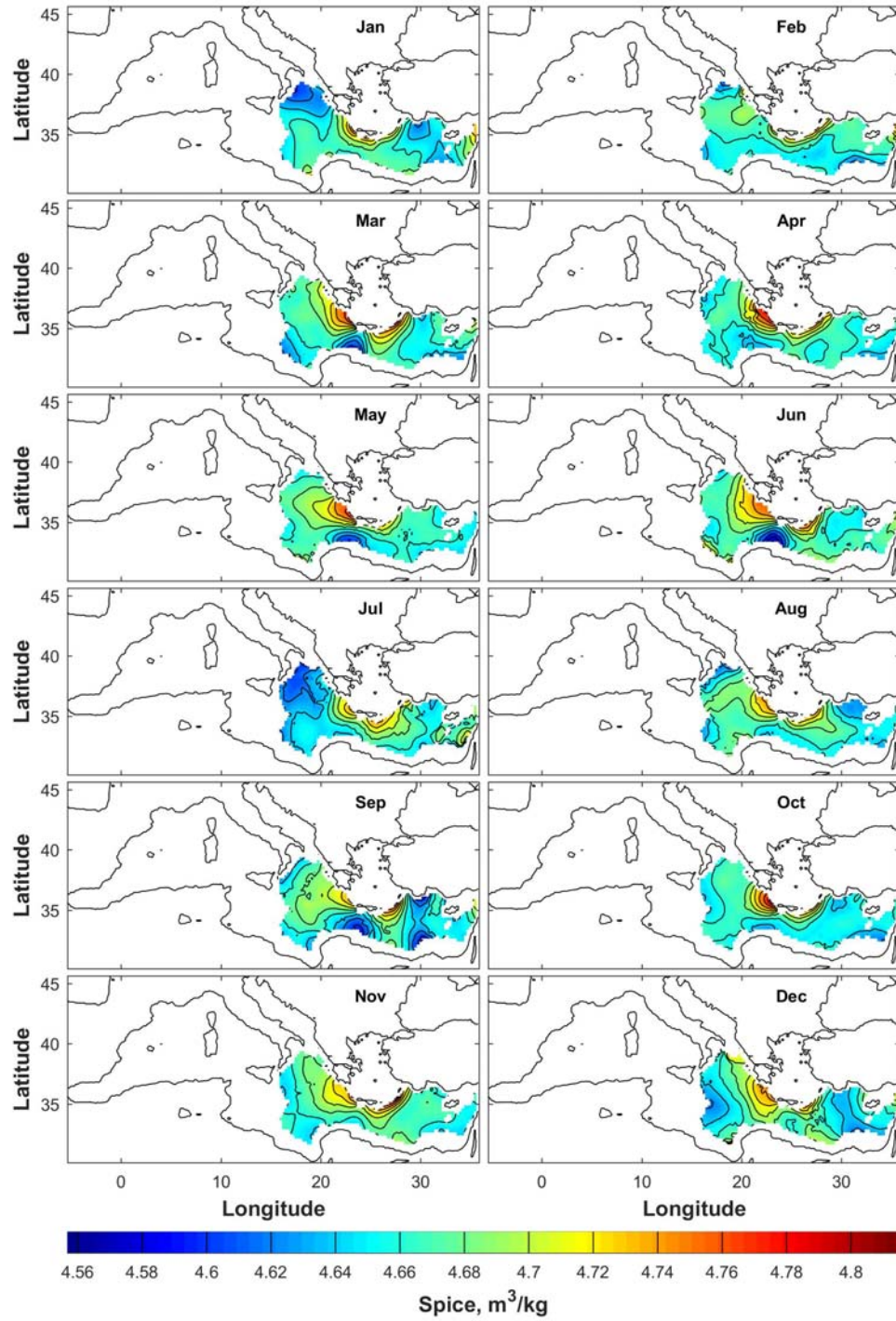
Figure 18.   SMG-WOD Multi-year Monthly Averaged Spiciness
at 1050 Meters
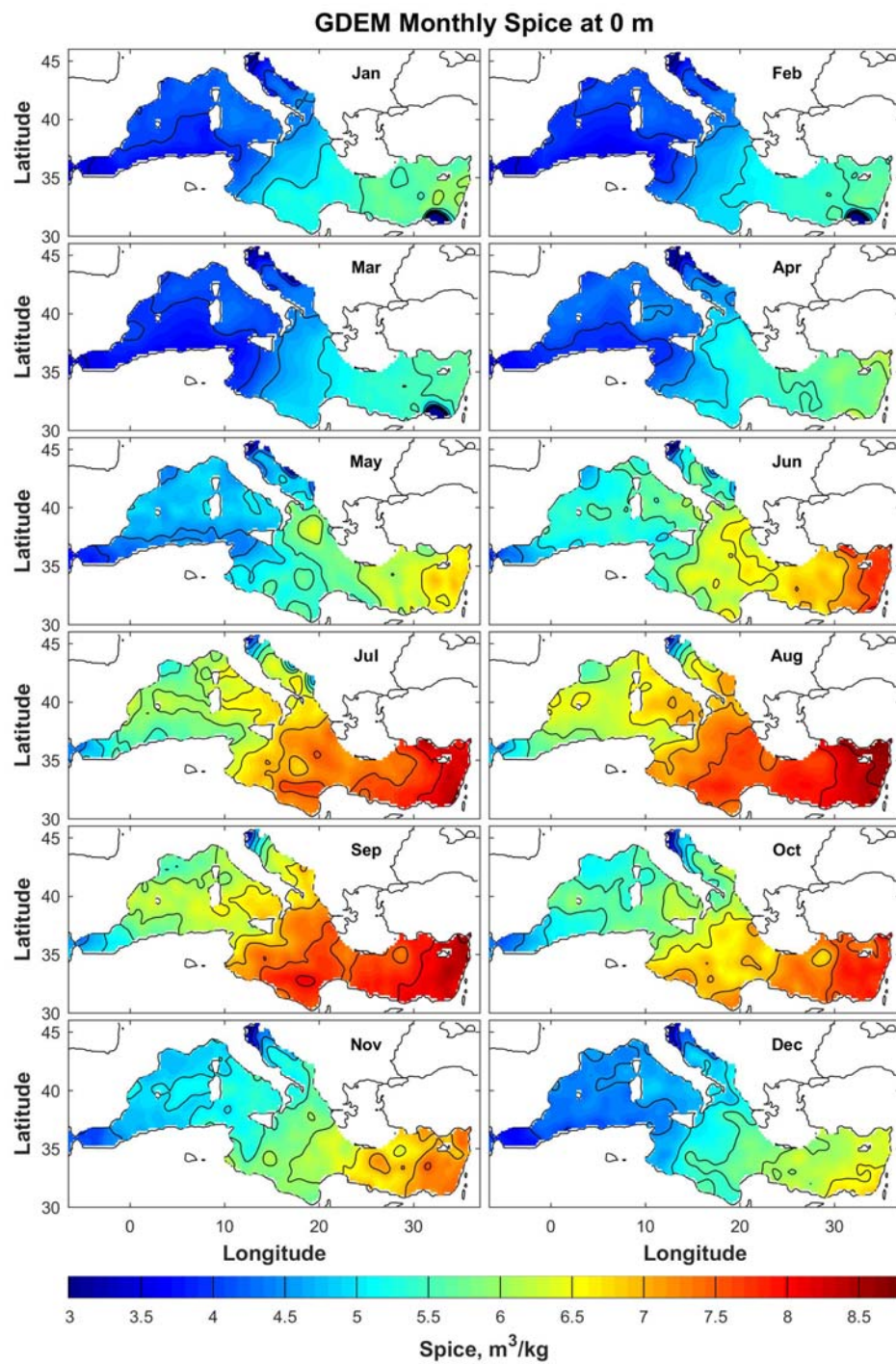
Figure 19.   GDEM Monthly Spice at Zero Meters
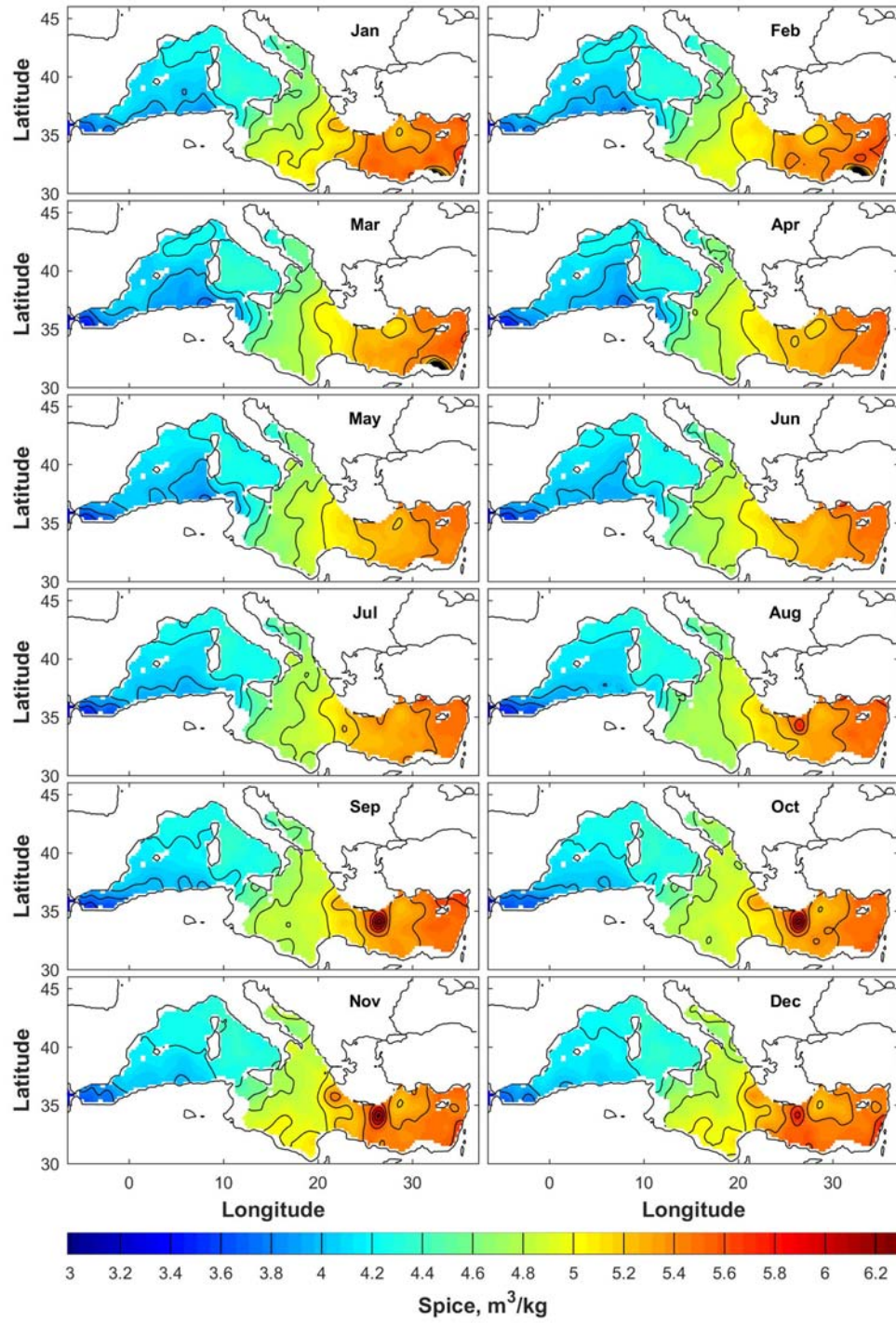
Figure 20.   GDEM Monthly Spice at 100 Meters

B. SOUND SPEED

Although there are an increasing number of naval operations in the Mediterranean Sea, sound speed profiles in the Mediterranean Sea are still lacking. One of the purposes of this thesis was to provide a background on sound speed profiles because the Mediterranean exhibits considerable seasonal and regional variations due to variation of temperature.

1. SMG-WOD MULTI-YEAR MONTHLY AVERAGE

SMG-WOD multi-year averaged fields of sound speed at 0 m and 100 m are displayed to show relation between spice and sound speed. Figure 21 shows the SMG-WOD sound speed at zero meters; the maximum values for spice and sound speed are summarized in Table 6. In the Eastern Basin, the sound speed was higher than in the Western basin. The maximum surface sound speed (1545m/s) was found in the east part of the Eastern Mediterranean Sea where the highest spiciness ($9.1\ m^3/kg$) manifested in the August. The maximum sound speed in the southern part of the central Mediterranean Sea was approximately 1542 m/s as observed close to the coast of Libya. For this location, spice was about $8.6\ m^3/kg$. The sound speed in the Western Mediterranean Sea, where the spice is $6.7\ m^3/kg$, was about 1535 m/s. As seen from Table 6, which summarizes these results, spice and sound speed are directly proportional to each other. Table 7 presents maximum values of sound speed and spice at 0 m in January, which are also correlated.

Table 6.　　Sound Speed and Spiciness at Zero Meters in August

Region	Spice	Sound Speed
Eastern part of the Eastern Mediterranean Sea	$9.1\ m^3/kg$	1545m/s
Southern part of central Mediterranean Sea	$8.6\ m^3/kg$	1542 m/s.
West of Sardinia Island	$6.7\ m^3/kg$	1535 m/s

Table 7.   Sound Speed and Spiciness at 0 meter in January

Region	Spice	Sound Speed
East Part of the Eastern Mediterranean Sea	5.6 m^3/kg	1520 m/s
Southern part of central Mediterranean Sea	5.4 m^3/kg	1518 m/s
West of Sardinia Island	3.7 m^3/kg	1510 m/s
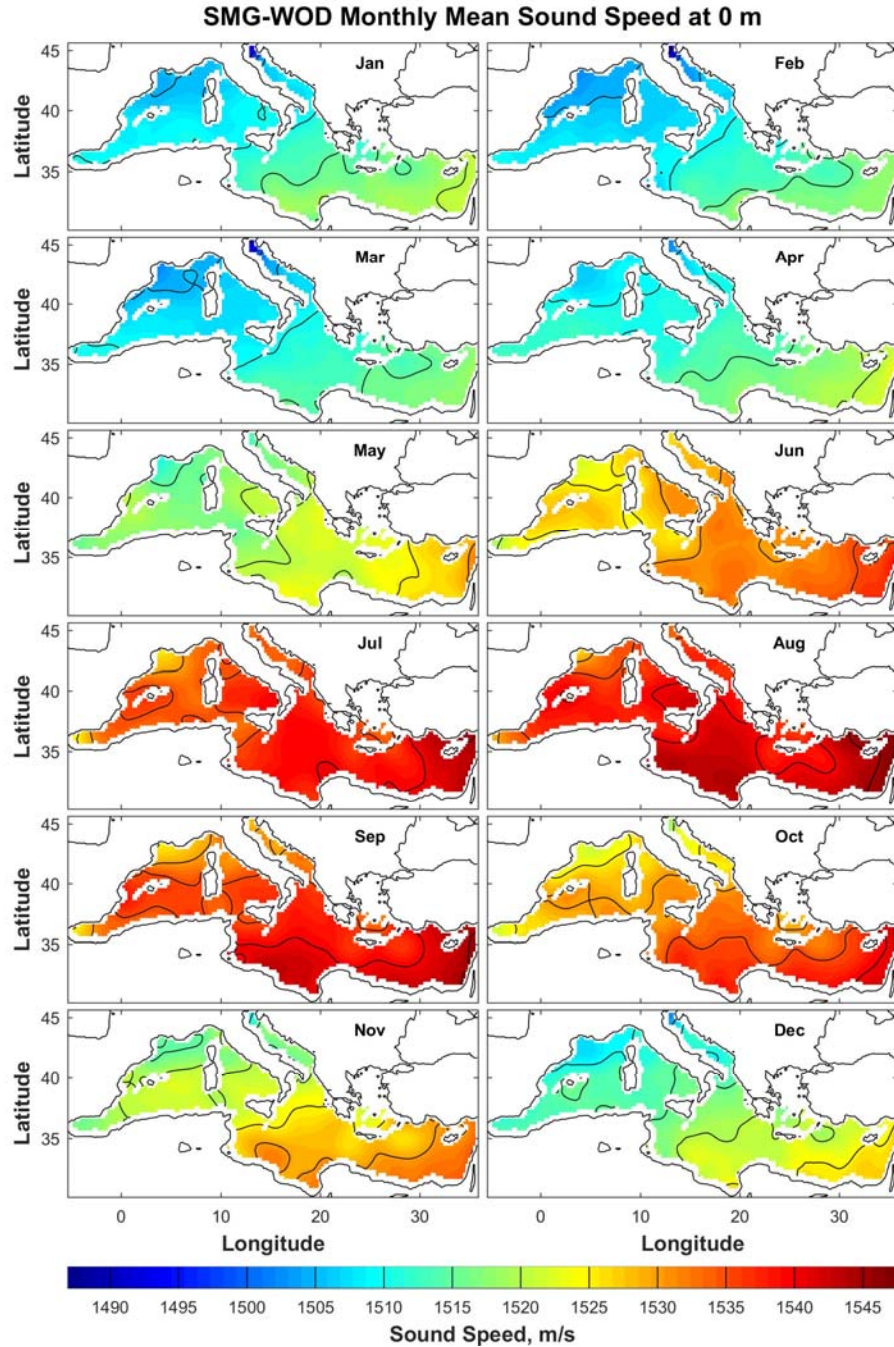
Figure 21.   SMG-WOD Monthly Mean Sound Speed at Zero Meters

Figure 22 shows the SMG-WOD sound speed at 100 meters; the maximum values for spice and sound speed for August and January are summarized in Tables 8 and 9. See Appendix D for a comprehensive collection of the SMG-WOD multi-year averaged monthly fields of sound speed and spice for deeper layers.

Table 8.   Sound Speed and Spice at 100 Meters in August

Region	Spiciness	Sound Speed
East Part of the Eastern Mediterranean Sea	$5.6\ m^3/kg$	1520 m/s
Southern part of central Mediterranean Sea	$4.6\ m^3/kg$	1517 m/s
West of Sardinia Island	$4.2\ m^3/kg$	1508 m/s

Table 9.   Sound Speed and Spiciness at 100 Meters in January

Region	Spice	Sound Speed
East Part of the Eastern Mediterranean Sea	$5.8\ m^3/kg$	1522 m/s
Southern part of central Mediterranean Sea	$4.8\ m^3/kg$	1515 m/s
West of Sardinia Island	$4\ m^3/kg$	1508 m/s
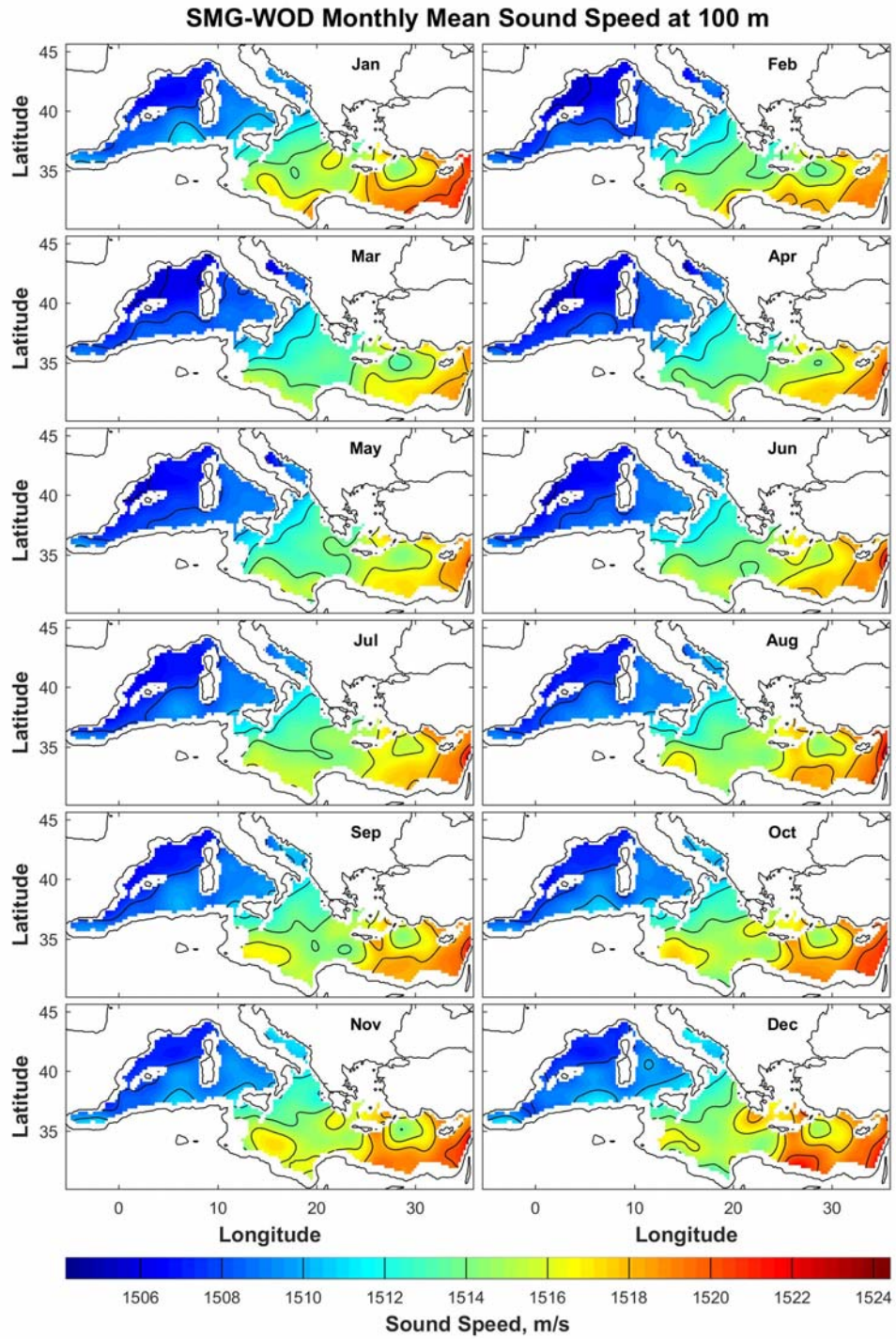
Figure 22.   SMG-WOD Monthly Mean Sound Speed at 100 Meters

2. GDEM MONTHLY FIELDS

We analyzed the monthly sound of the GDEM at same depths to compare the results of the two models. The GDEM monthly sound speed at 0 meters and 100 meters are plotted in Figures 23 and 24. Other results are provided in Appendix E. Tables 10–13 summarize maximum values for spice and associated sound speed. The maximum surface sound speed (1545 m/s) was found in the eastern part of the Eastern Mediterranean Sea. This is in agreement with the SMG-WOD multi-year averaged data.

Table 10.　Sound Speed and Spiciness at Zero Meters in August

Region	Spiciness	Sound Speed
East Part of the Eastern Mediterranean Sea	$9.1\ m^3/kg$	1545m/s
Southern part of central Mediterranean Sea	$8.6\ m^3/kg$	1542 m/s.
West of Sardinia Island	$6.7\ m^3/kg$	1535 m/s

Table 11.　Sound Speed and Spiciness at Zero Meters in January

Region	Spiciness	Sound Speed
East Part of the Eastern Mediterranean Sea	$5.7\ m^3/kg$	1522 m/s
Southern part of central Mediterranean Sea	$5.3/kg$	1519 m/s
West of Sardinia Island	$3.8\ m^3/kg$	1510 m/s

Table 12.　Sound Speed and Spiciness at 100 Meters in August

Region	Spiciness	Sound Speed
East Part of the Eastern Mediterranean Sea	$5.5\ m^3/kg$	1519 m/s
Southern part of central Mediterranean Sea	$4.7\ m^3/kg$	1516 m/s.
West of Sardinia Island	$4.2\ m^3/kg$	1507 m/s

Table 13.　Sound Speed and Spiciness at 100 Meters in January

Region	Spiciness	Sound Speed
East Part of the Eastern Mediterranean Sea	$5.7\ m^3/kg$	1521 m/s
Southern part of central Mediterranean Sea	$4.9\ m^3/kg$	1517 m/s
West of Sardinia Island	$4.1/kg$	1503 m/s

GDEM Monthly Sound Speed at 0 m
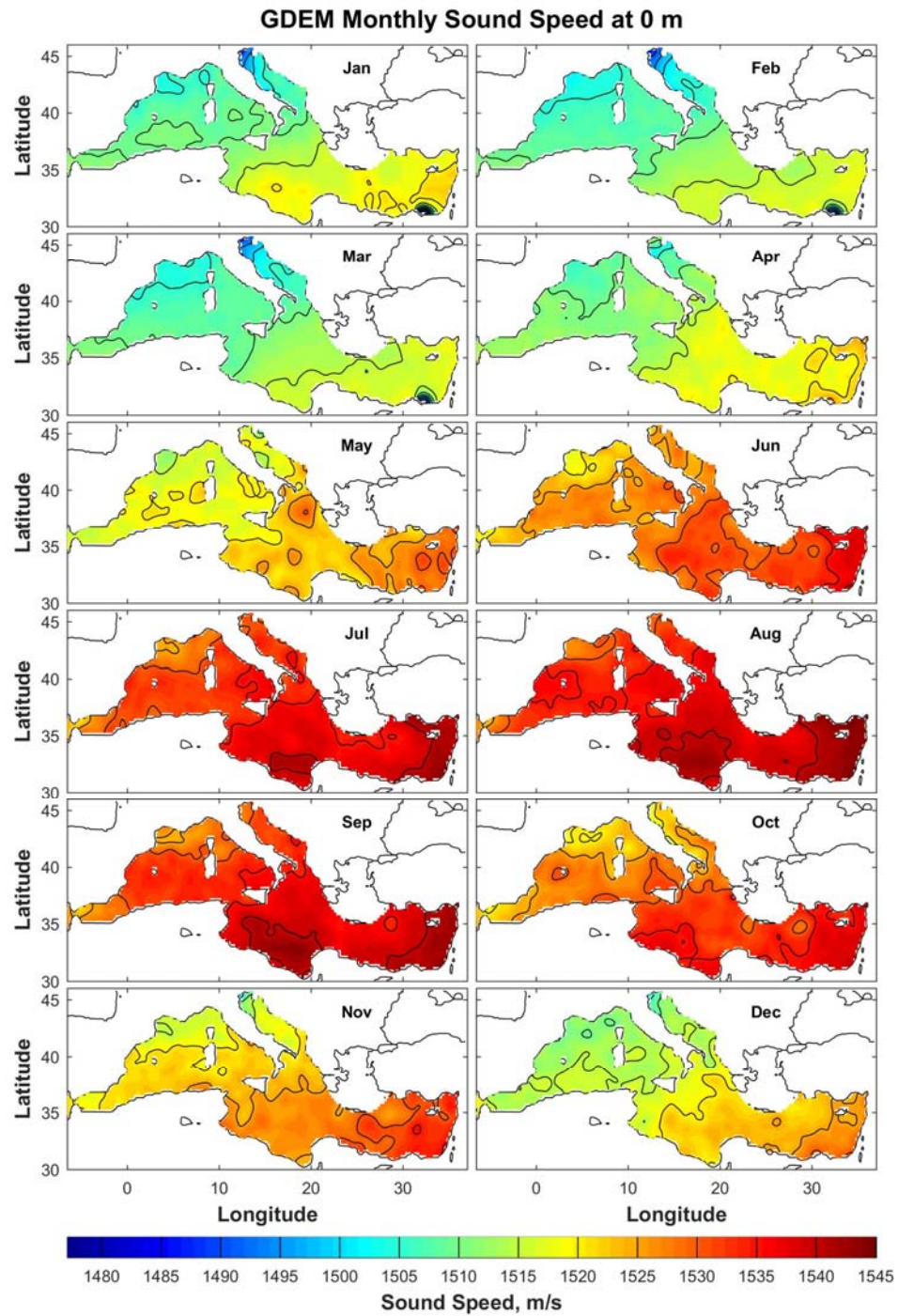
Figure 23.   GDEM Monthly Sound Speed at Zero Meters
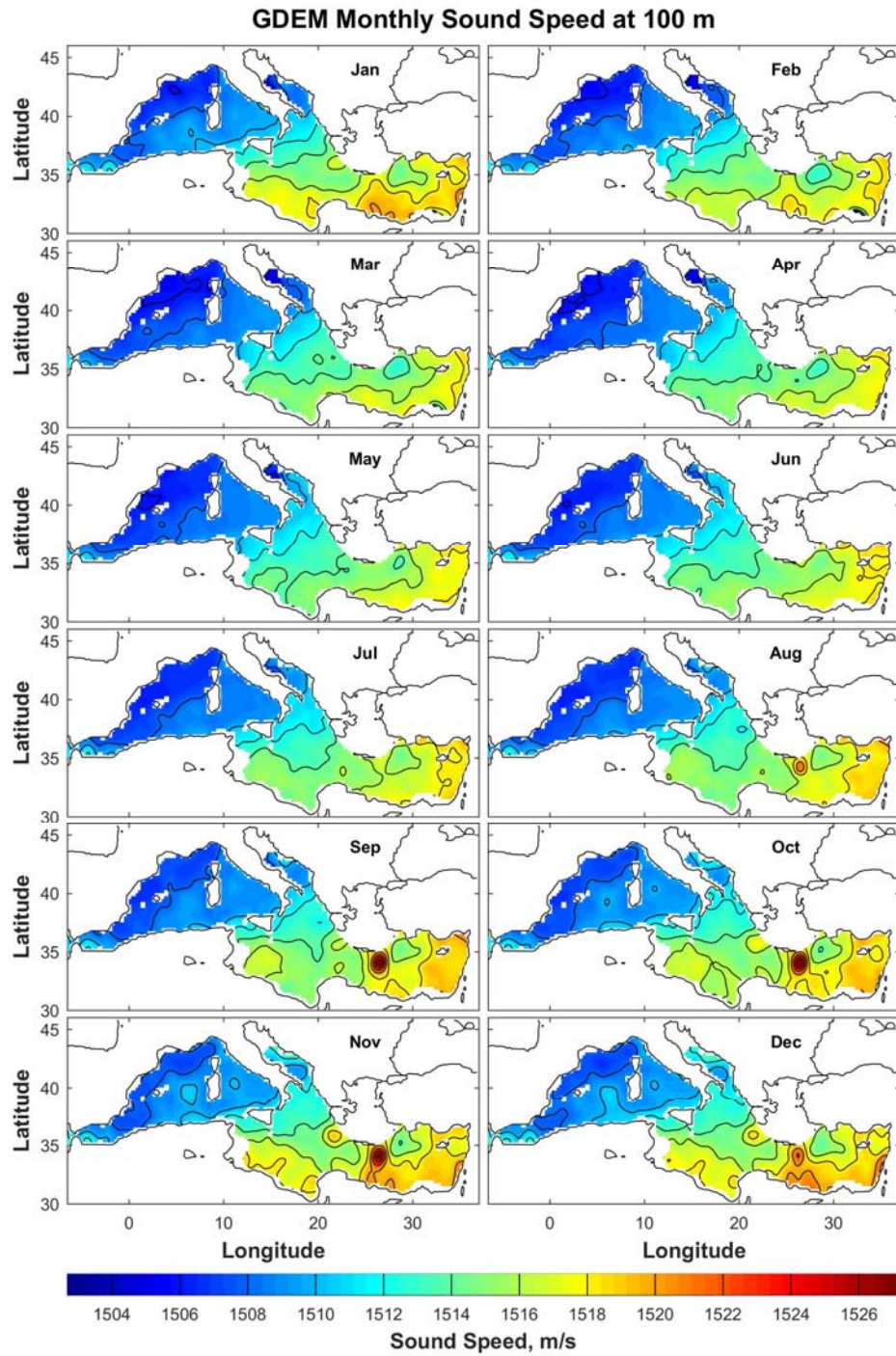
Figure 24.   GDEM Monthly Sound Speed at 100 Meters

Unless pressure dominates, the maximum sound speed is usually found in regions where maximum spiciness exists. Therefore, we decided that the spiciness variable could be used to compare the water masses for sound speed in regions where pressure does not dominate. In deep layer, the sound speed will be so high. Thus, although we see very low spiciness in deep layers, the sound speed will be so high due to pressure effects. In addition, there was a slight difference in spiciness values of the GDEM and SMG-WOD; however, the SMG-WOD did not perform well in coastal regions.

C.   ACOUSTIC PROPAGATIONS AND SOUND SPEED PROFILES (SSP)

Three fundamental layers exist in the ocean according to sound speed (Figure 25). The surface layer is the most variable layer in the ocean. It can be affected by winds and currents among other variables. It is also called a well-mixed layer. The main thermocline layer is located between the surface layer and deep isothermal layers. It is the layer where in the temperature changes rapidly with increasing depth. Under the main thermocline, the temperature is relatively constant; however, sound speed starts to increase due to the pressure effect.

In this research, the surface layer is the main layer of the interest. It is also referred to as seasonal layer. It is greatly influenced by the temperature. During the summer, the surface waters warm more quickly than the deeper waters. Thus, there is a sharp negative gradient below the surface water. This is common in Mediterranean Sea due to very warm, and thin Levantine Surface Water that forms in August.

In summer seasons, sound channels can occur below the main thermocline. At the lowest of the main thermocline, the sound speed reaches its minimum value; which can also be the axis of the sound channel. Figure 26 depicts the sound channel. According to Snell's law, as sound passes through different water layers, the ray will bend toward the region where sound speed is slower, thus creating a propagation path. The sound speed reaches its minimum at the axis of the thermocline. Therefore, sound will bend toward the axis of the thermocline.
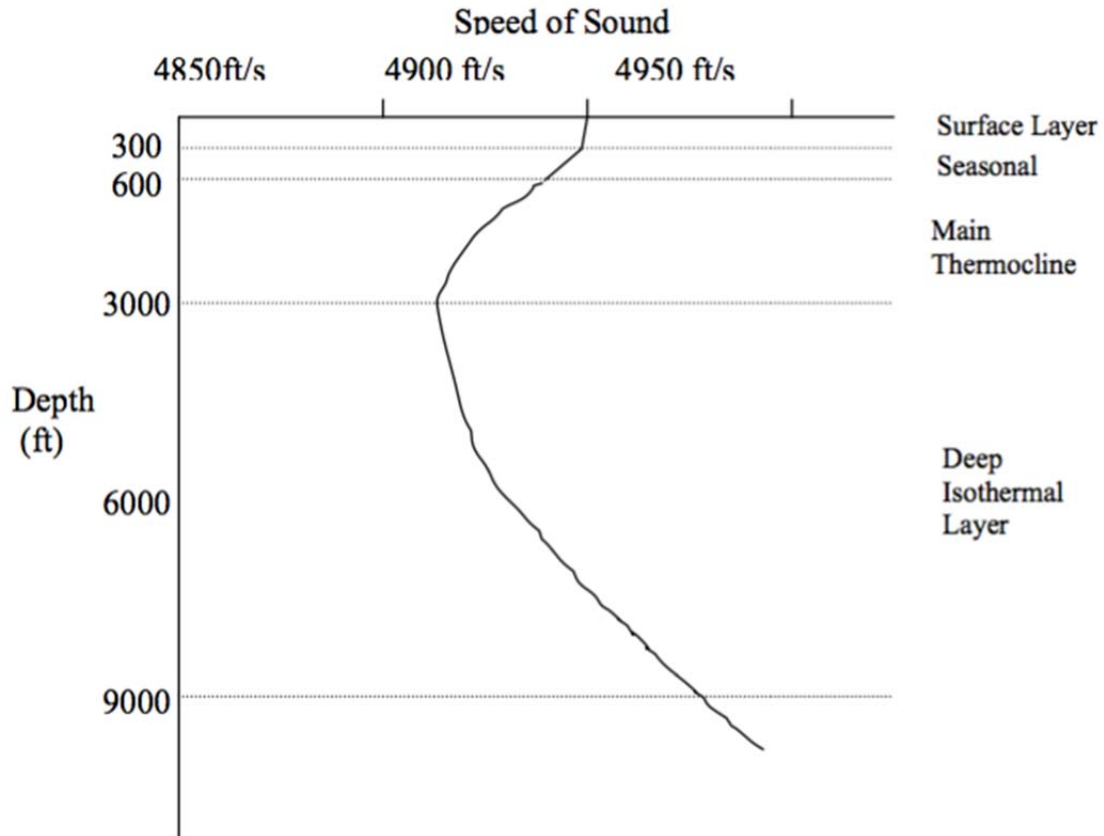
Figure 25. Three Main Layers in the Ocean. Adapted from Kalmbach (2011).

During the winter seasons, there are very strong winds in the Mediterranean region. Due to strong winds and cooling, a large scale mixing in winter makes the temperature of the surface layer almost vertically constant. Under the seasonal layer, the sound speed can decrease rapidly with depth within the main thermocline. Beneath the main thermocline, a deep isothermal layer exists. For the isothermal case, sound speed starts to increase due to pressure effects. These cases may cause a shadow zone, which Figure 27 depicts.
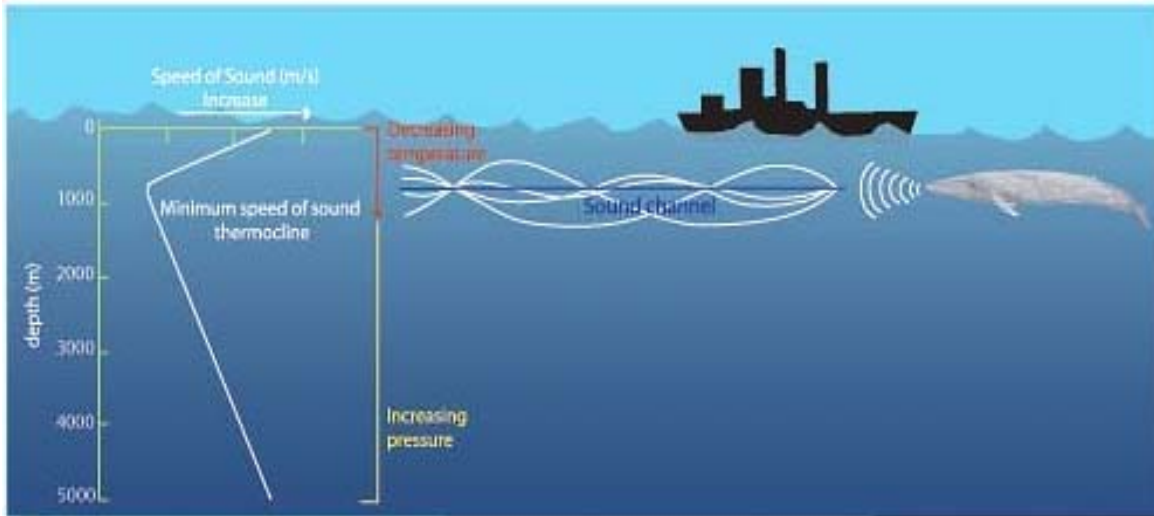
Figure 26.   Sound Channel. Adapted from the Office of
Ocean Exploration and Research (2001).
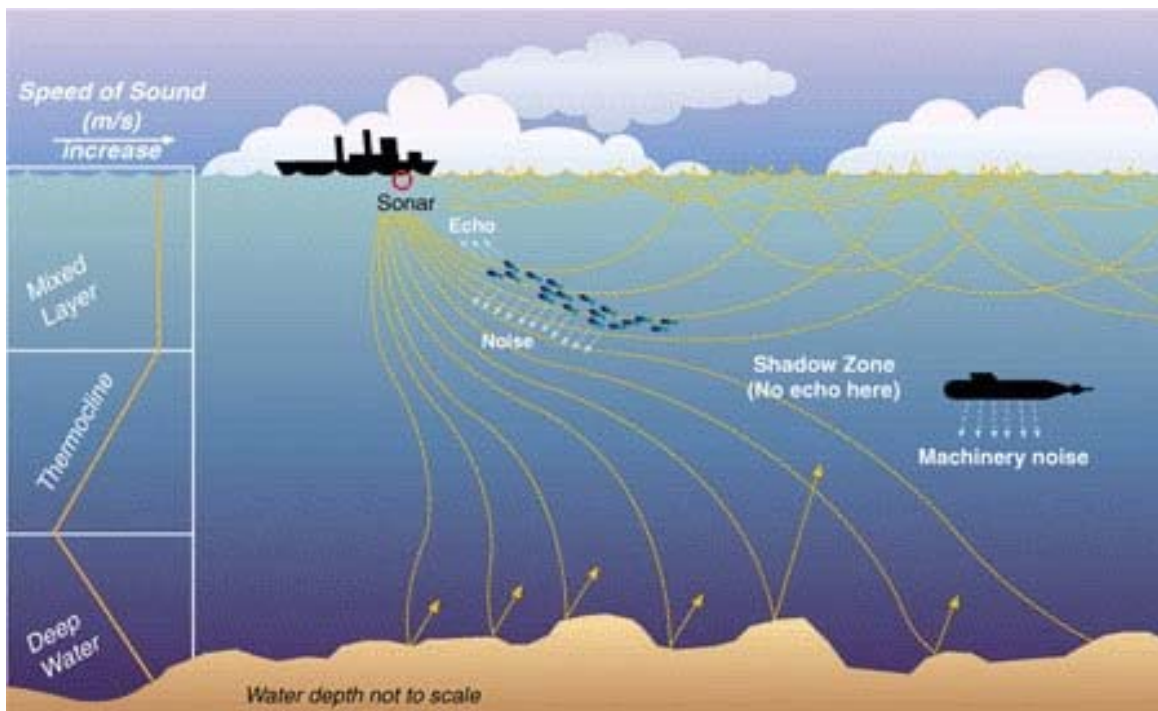
Figure 27.   Shadow Zone. Adapted from DOSITS (2014).

D. SOUND SPEED PROFILES

The total and monthly mean SSPs for the SMG-WOD and GDEM are calculated at five points of interest (Figure 28) selected in the Western ("E"), Central ("B" and "D") and Eastern ("A" and "C") Mediterranean Sea to cover the whole basin and analyze the regional variations. Table 14 provides the coordinates, bottom sediment types and depths for these points. Seasonal variability in SMG-WOD and GDEM SSPs is analyzed for each point.
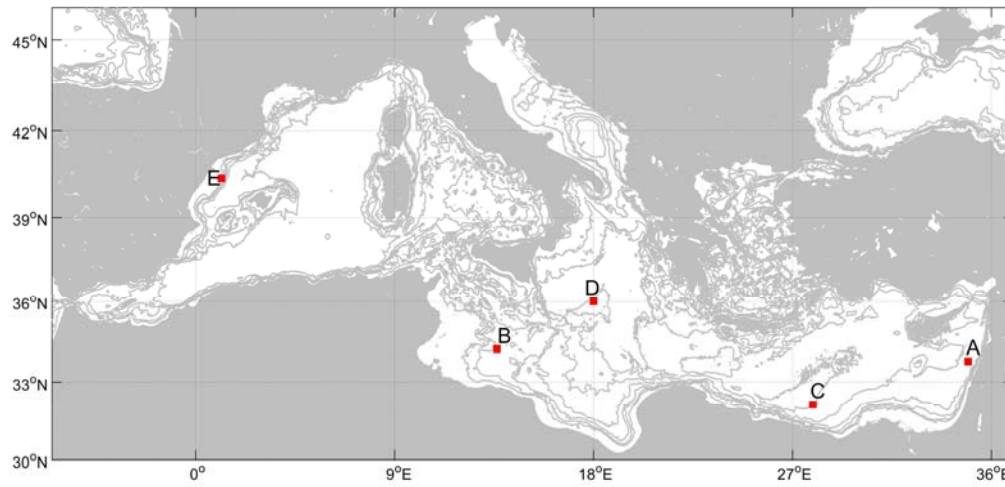
Figure 28.   Locations of Analysis Points

Table 14.   Points A through E

Location	Latitude (N)	Longitude (E)	Depth (m)	Bottom Sediment	Region
A	33.7794	34.939	1000	clay	Eastern
B	34.2399	13.6275	200	very fine sand	Central
C	32.1361	27.9229	1000	sandy mud	Eastern
D	36	18	1000	very fine silt	Eastern
E	40.3946	1,1739	70	sandy mud	Western

1.   Point A (Eastern Mediterranean Sea)

Summer and fall seasons exhibit a sharp negative gradient in sound speed due to strong surface heating, extending down to approximately 80 meters. Then, the sound

speed continues to exhibit a weaker negative gradient down to the axis of the sound channel, layered at a depth of 400 meters where the minimum sound speed (1515 m/s) exists. Beneath the sound channel, between 400 and 1000 m, the sound speed shows a positive gradient due to increased pressure.

The total mean for SMG-WOD SSPs and GDEM SSPs at point A located in the Eastern Mediterranean Sea are plotted in Figure 29a. The corresponding SMG-WOD multi-year monthly averages and standard deviations are shown in Figure 30 along with the GDEM monthly mean SSP.
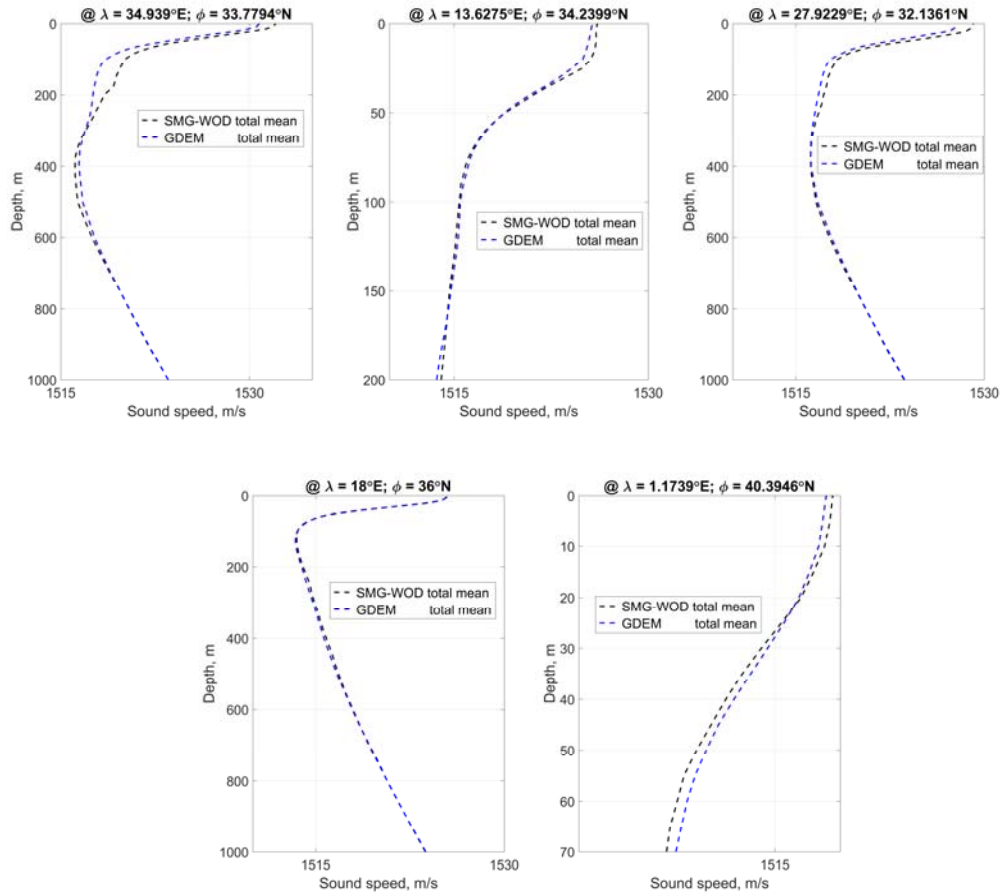
Figure 29.   Total Mean SSP

SMG-WOD SSP multi-year monthly average and GDEM monthly means correspond well in surface layers and isothermal deep layers. Below the surface layers to the depth of 250 meters, the SMG-WOD SS is about 3 m/s higher than the GDEM

50

monthly mean. The SMG-WOD standard deviation is rather small as expected. However, it does not mean that the inter-annual variability is small since the standard deviation is not a full representation of possible outliers or non-periodic inter-annual and decadal oscillations.

January through March exhibits well-mixed surface layers due to elevated mixing. Surface waters are not heated as much as in summer and fall. Thus, the mean sound speed at the surface is lower in winter. Below the surface waters to the depth of 400 m, the sound speed exhibits a negative gradient. Below 400 m, the sound speed shows a positive gradient due to pressure effects. The sound channel is located at 400 m in August. Convergence zones are resent during all seasons.

The greatest variance between monthly mean and total mean exists in the upper layers, particularly from January through March. The greatest variance is about 12 m/s in March and February. It is about 9 m/s in the January. In the summer and fall , there is a slight difference between the monthly mean and total mean in all layers.

2. Point B (Central Mediterranean Sea)

The total means for SMG-WOD SSPs and GDEM SSPs at point B located in the Central Mediterranean Sea are plotted in Figure 29b. The corresponding SMG-WOD multi-year monthly averages and standard deviations are shown in Figure 31 along with the GDEM monthly mean SSP.

January through April exhibit an almost uniform gradient from the surface to the bottom layer. This was assessed as slightly positive gradient. Below 100 meters, it shows a very week negative gradient due to temperature effects. In April, it exhibits a very weak negative gradient down to 60 meters resulting from some surface heating. Beneath 60 meters, a very week positive gradient exists. The surface duct is present from December to April due to lower sound speed at the surface. In addition, we expect to see the sound bending downward from May to November due to high sound speed at the surface. Because the sea is shallow there, this case will create bottom bounce profiles.
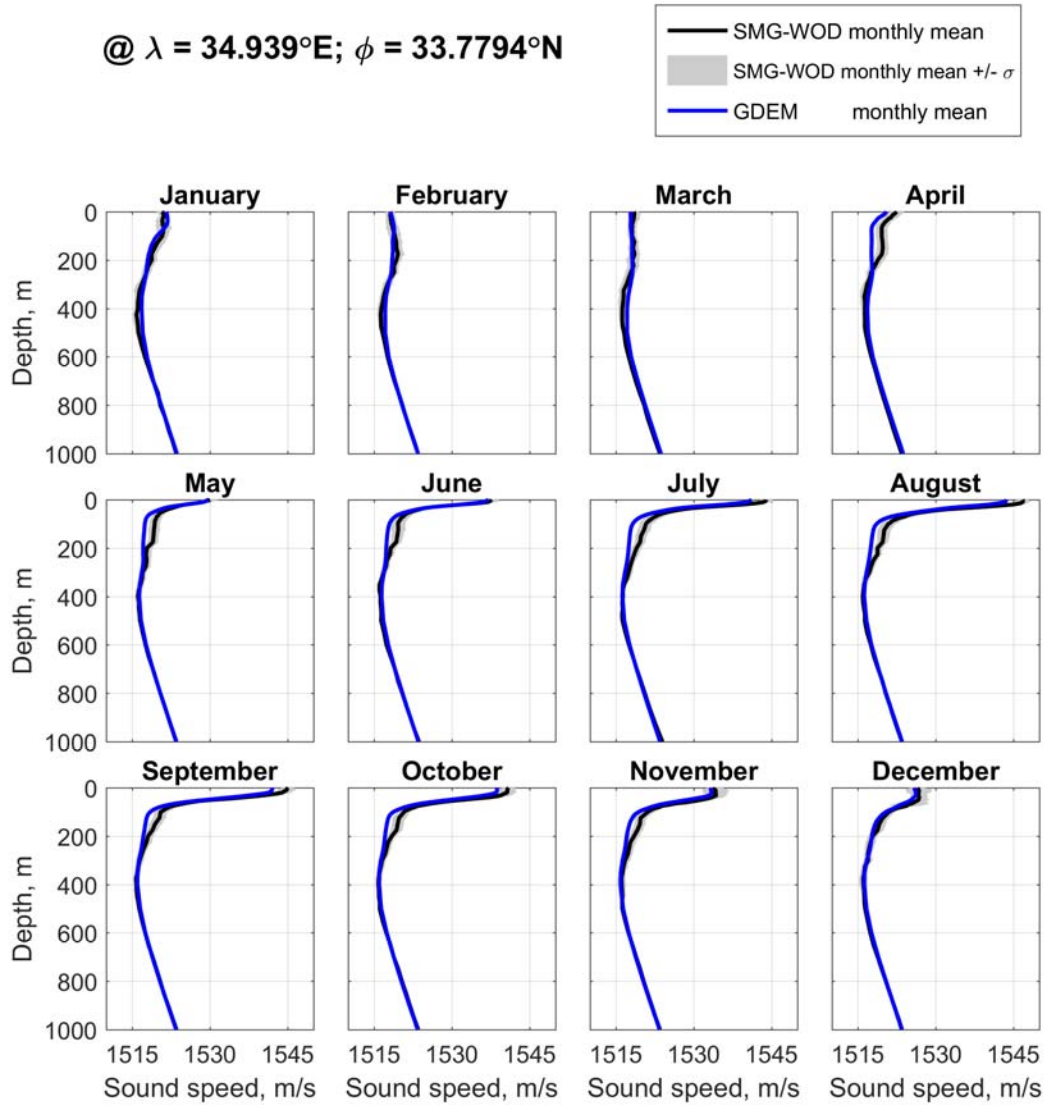
Figure 30.   Mean Sound-Speed Profiles (Point A)

@ λ = 13.6275°E; ϕ = 34.2399°N
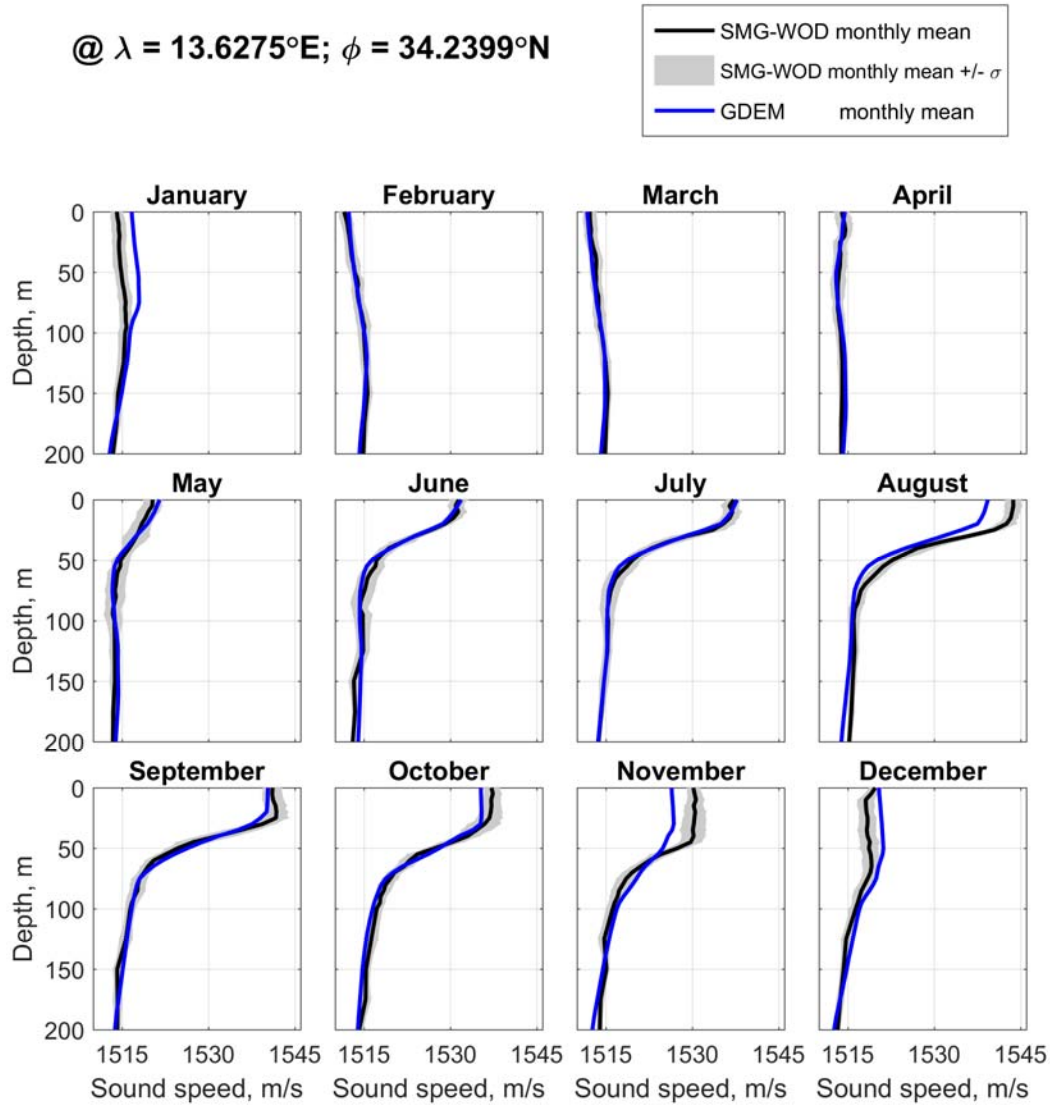
Figure 31. Mean Sound-Speed Profiles (Point B)

In May, surface heating starts and the heat increases into summer and early fall. This creates a very strong negative gradient in the upper layer, especially in August. Sound speed decreases with depth rapidly down to 60 m. Then it shows a very weak negative gradient or uniform distribution down to the bottom.

The maximum sound speed (1545m/s) is found at the surface in the August. The minimum sound speed (1508 m/s) is found at the surface in February. The greatest variance between the monthly means and total means exist in the upper layers,

53

particularly in August and September with 14 m/s and in February and March with 13 m/s.

Weak surface duct propagation can be expected in January through March due to slightly positive gradient. The rays will bend upward and reflect through the bottom. This reflection can create trapping layers above 100 m. The sound can propagate over a long distance in trapping layers. This is a very disadvantageous environment for submarines that sail at periscope depth. Figure 32 illustrates the surface duct propagation.
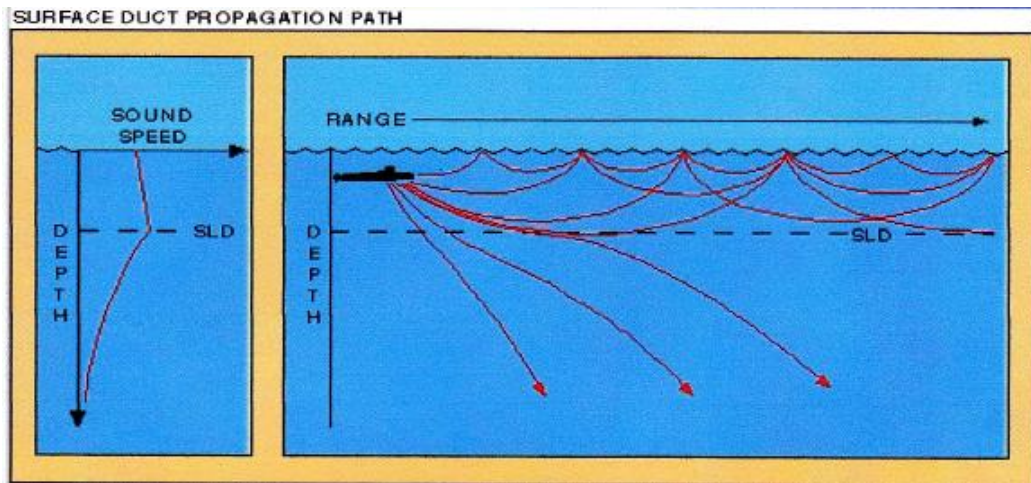
Figure 32. Surface Duct Propagation. Adapted from the Department of Oceanography, Naval Postgraduate School (2015).

3. Point C (Eastern Mediterranean Sea)

The total means for SMG-WOD SSPs and GDEM SSPs at point C located in the Eastern Mediterranean Sea are plotted in Figure 29c. The corresponding SMG-WOD multi-year monthly averages and standard deviations are shown in Figure 33 along with the GDEM monthly mean SSP.

The summer season exhibits a sharp negative gradient in the surface layer. The sound speed decreases rapidly from the surface to 80 m. Then a thermocline occurs below 80 m extending to a depth of 400 m, where the minimum sound speed exists. At the lowest depth of the thermocline, a sound channel is observed. In June, the sound speed reaches a minimum at two levels, 80 and 400 meters. Thus, we expect to see sound

channels at these depths. Having two sounds channels is a strong indicator that sound will propagate over a long distance.

A weak positive gradient is observed in the upper layer in January, February and March. Positive gradient increases from January to March. In March, the positive gradient extends down to 200 m.

Below the upper layer with the positive gradient of sound speed, a negative gradient is observed. The minimum sound speed is reached at the depth of 400 meters. In February and March, there are two minimum sound speed levels, at the surface and 400 meters. Below 400 meters, sound speed increases constantly with depth. This environment may cause a surface duct propagation at the surface.

The greatest variance between monthly mean total means exist in the upper layers, particularly in February and March. Again, there is a difference between monthly means in the thermocline, which must be the result of different vertical resolutions between the two datasets.
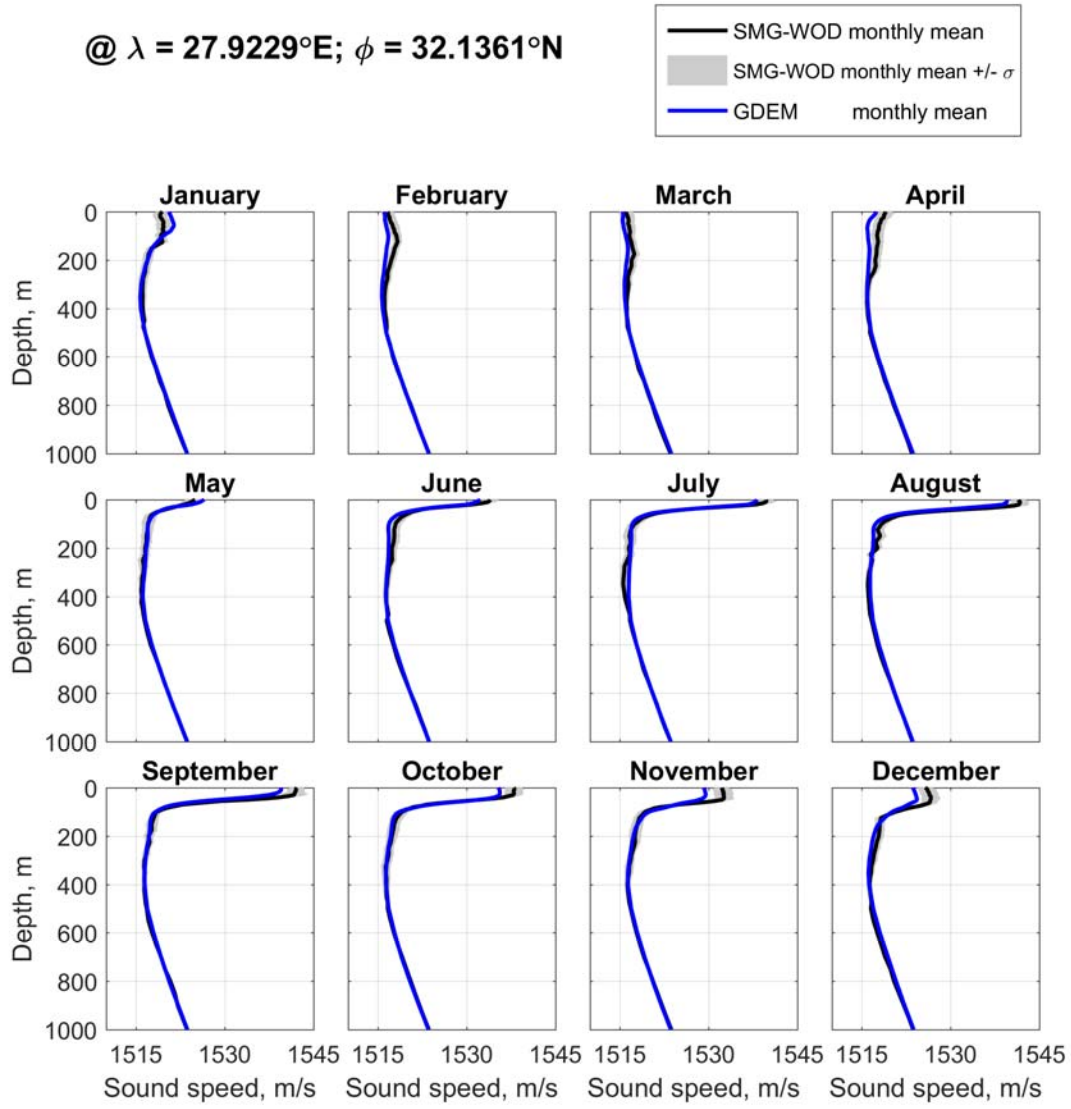
Figure 33. Climatological Monthly Mean Sound Speed Profiles (Point C)

4.   Point D (Eastern Mediterranean Sea)

The total means for SMG-WOD SSPs and GDEM SSPs at point D located in the Eastern Mediterranean Sea are plotted in Figure 29d. The corresponding SMG-WOD multi-year monthly averages and standard deviations are shown in Figure 34 along with the GDEM monthly mean SSP.

A negative gradient in the surface layer exists April through November, followed by a uniform gradient in the surface layer extending to 20 meters in December. Then it shows a negative gradient down to about 80 meters. The sound speed decreases rapidly from surface to the depth of 80 meters. The strongest negative gradient occurs in August due to surface heating. The sound speed reaches its minimum at a depth of 80 meters in all months except for February. This pattern may create a surface sound channel. The minimum sound speed occurs at the surface in February. Point D shows a positive gradient in all depths as exhibited in the Arctic Ocean. Figure 35 presents the sound propagation in the Arctic Ocean.
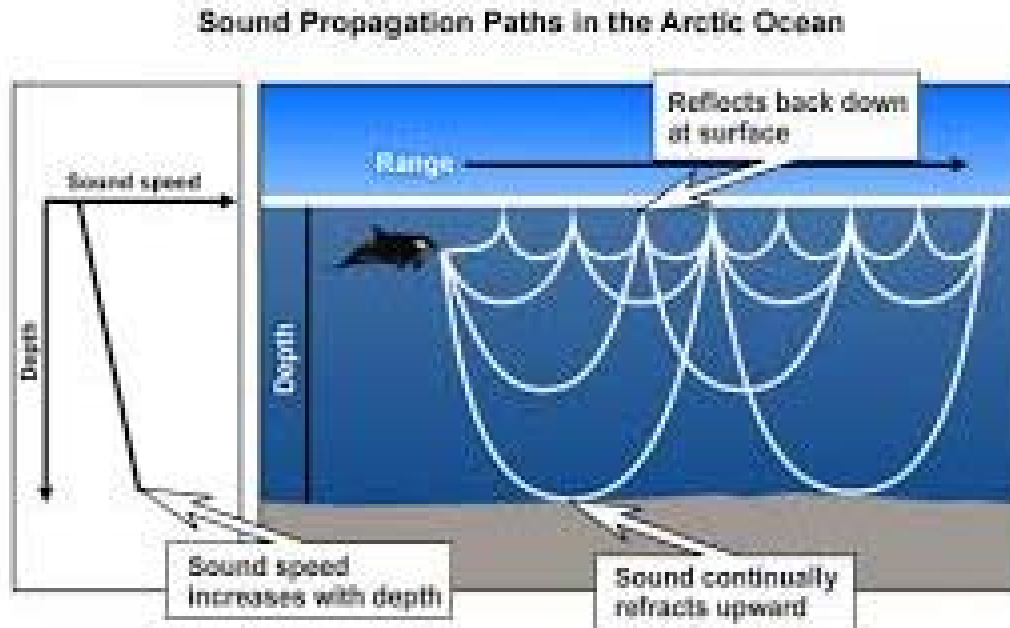
Figure 34.   Sound Propagation in the Arctic Ocean

57

In March, the SMG-WOD shows a minimum sound speed at the surface, but the GDEM shows it at a depth of 80 meters as in other months.

The greatest variance (approximately 17 m/s) between monthly and total means exists in the upper layers, particularly from January to March.
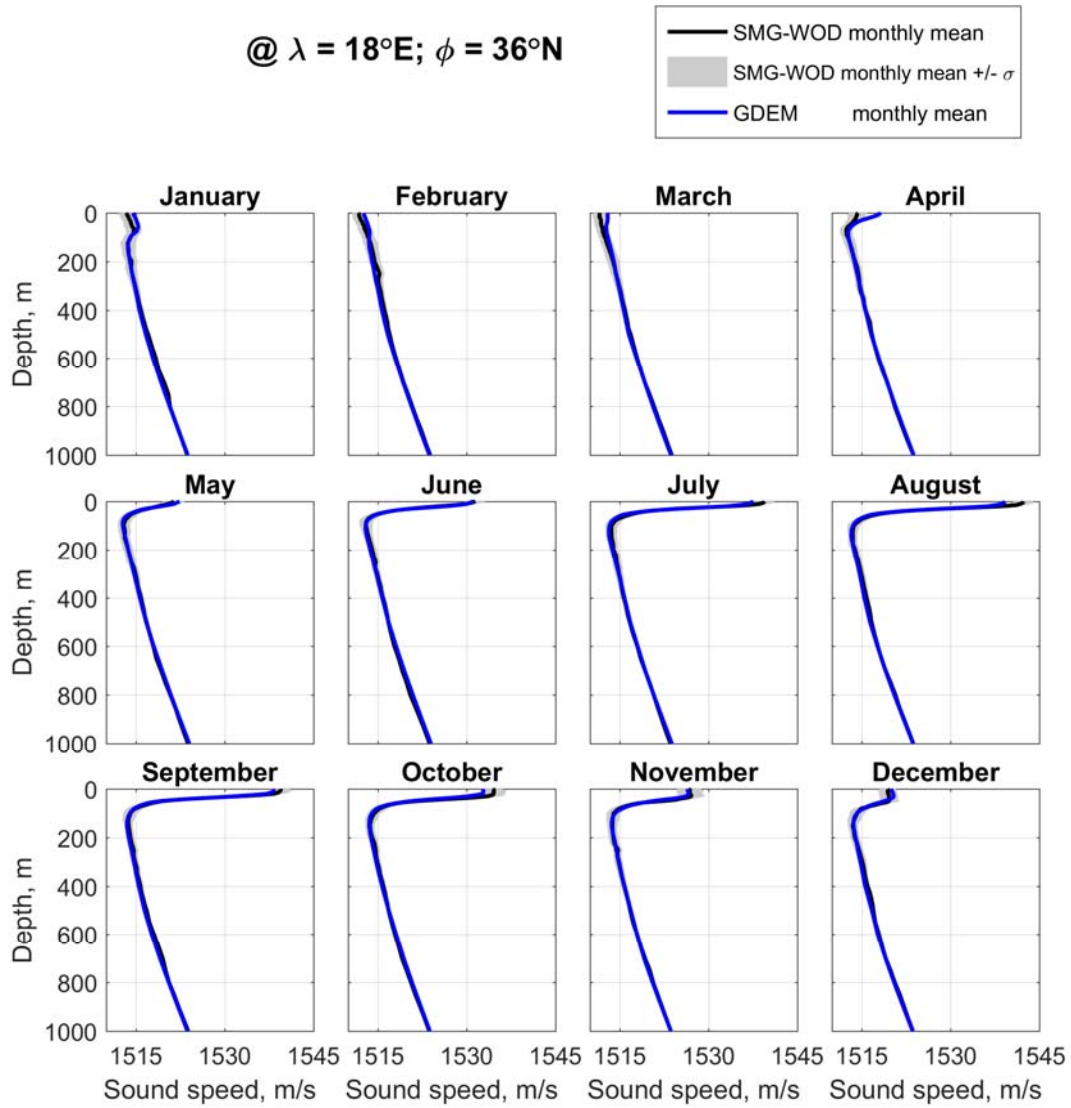
Figure 35.   Climatological Monthly Mean Sound Speed Profiles (Point D)

5.   Point E (Western Mediterranean Sea)

The total means for SMG-WOD SSPs and GDEM SSPs at point E located in the Western Mediterranean Sea are plotted in Figure 29e. The corresponding SMG-WOD multi-year monthly averages and standard deviations are shown in Figure 36 along with the GDEM monthly mean SSP.
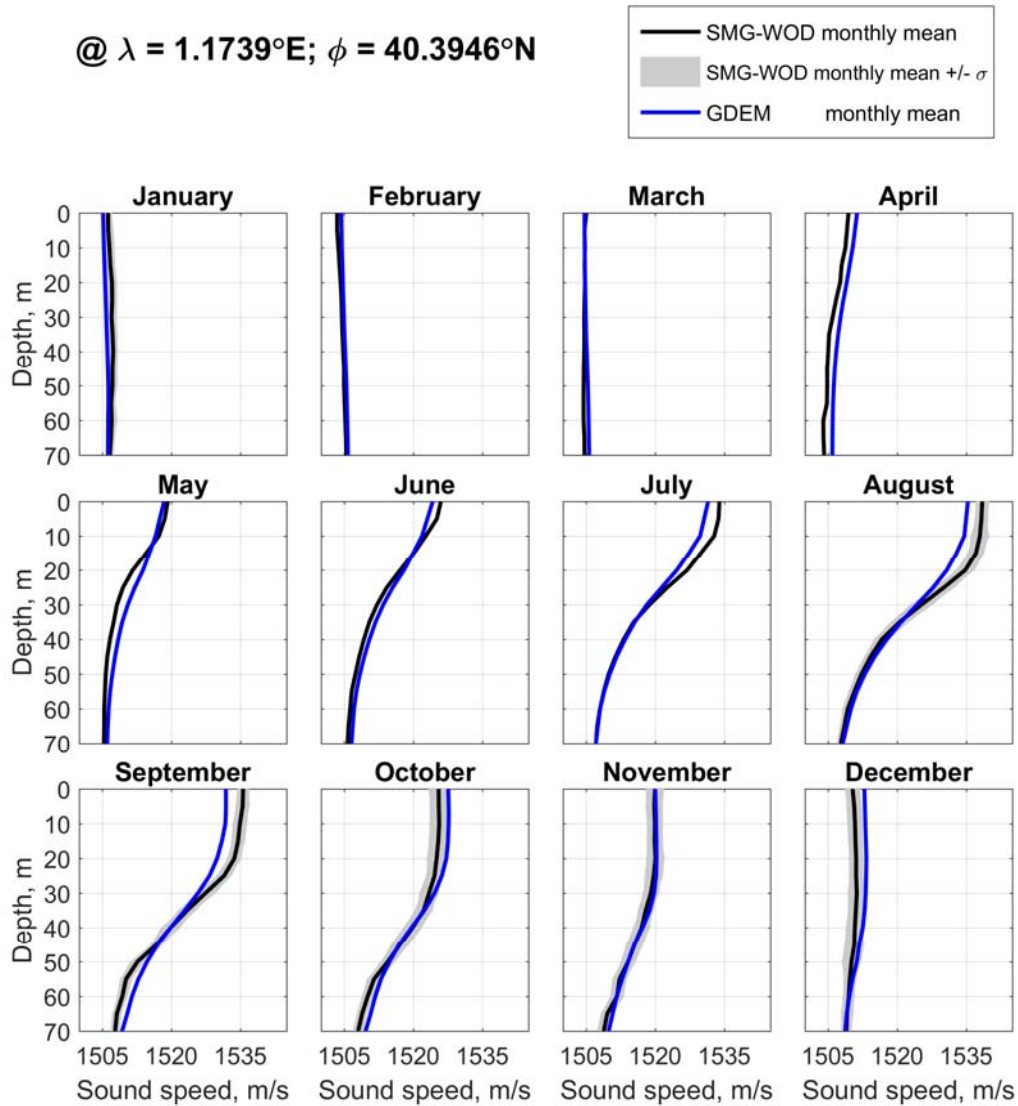

Figure 36.   Climatological Monthly Mean Sound Speed Profiles (Point E)

In December through March, monthly means are almost uniform due to strong and cold winds. Wind stirring mixes the surface layer and creates an isothermal surface layer of water. It is well-mixed and very shallow. Thus, thermocline does not exist in these months. Surface heating starts in April and increases until August as expected. Maximum mean values (1535 m/s) are found in August. The August profile shows a stronger negative gradient. The SMG-WOD standard deviation is very small here, and the annual SSPs is close to mean monthly values. The greatest variance (approximately 15 m/s) between monthly mean and total mean occurs in August and September in the upper of a depth of 30 meters. The minimum variance occurs in May in the upper 10 m layer and in June the deeper layer at the depth of 20 m. The maximum variance is observed two months later, in August, due to significant heating.

Table 15 summarizes expected acoustic propagation types and months when maximum seasonal variations are observed.

Table 15.   Possible Propagation Types and Maximum Variations

Location	Region	Depth (m)	Month	Possible Propagation Type	Maximum Variation
A	Eastern	1000	August	Sound Channel (400 m)	February and March
A	Eastern	1000	January	Sound Channel (400 m)	February and March
B	Central	200	August	Sound Bends Downward	August
B	Central	200	February	Weak Surface Duct	August
C	Eastern	1000	August	Sound Channel (400 m)	February and March
C	Eastern	1000	March	Surface Duct	February and March
D	Eastern	1000	August	Sound Channel (80 m)	January - March
D	Eastern	1000	February	Surface duct	January - March
E	Western	70	August	No Sound Channel or Duct	August
E	Western	70	January	No Sound Channel or Duct	August

At points A, C and D it is possible to see convergence zones in layers deeper than those shown in Table 15. Maximum variance in the Eastern Mediterranean Sea occurs in January through March; for the central and the Western Mediterranean Sea, the maximum variance occurs in the August.

E.   MEAN TRANSMISSION LOSS -GDEM

Transmission loss has been modeled using Bellhop for a 3500 Hz sound source located at 40 m and 101 evenly distributed receiver depths, along a west-east path for maximum propagation range of 70 nm, using GDEM monthly mean sound speed profiles. To be able to see how sound propagates in the Mediterranean Sea will provide us with information on where the submarines can be detected. Figures 37–41 show transmission loss for each month at points A–E.

a.   *Point A*

We expected to see a sound channel at a depth of 400 m in January and August; however, Figure 37 shows no sound channel in August. In August, sound rays propagated downward to 1600 m due to a very high sound speed at the surface. Then, they refracted upward due to high speed at a depth of 1600 meters. Therefore, sound rays created convergence zone at the surface at an approximately 35 km range and submarines could have been detected from long distances where the convergence path occurred. Also, there was a direct path near the surface within an 8 km range, and the TL was about 80–85 dB. Thus, submarines could also have been detected near the surface within an 8 km range. Between 8 km and 35km, it is difficult to detect submarines due to the very large shadow zone.

For January, we detected a surface duct propagation within the 17 km range and a convergence zone at the 35 km range. Thus, submarines could have been detected within the 17 km range at the surface. They also could have been detected from long distances where the convergence path occurred. For February and March, we detected a surface duct within the 45 km range and a sound channel convergence zone at a depth of 750–1700 meters. The convergence path occurred at the 32 km range. Thus, submarines could have been detected at the surface from long distances.

61
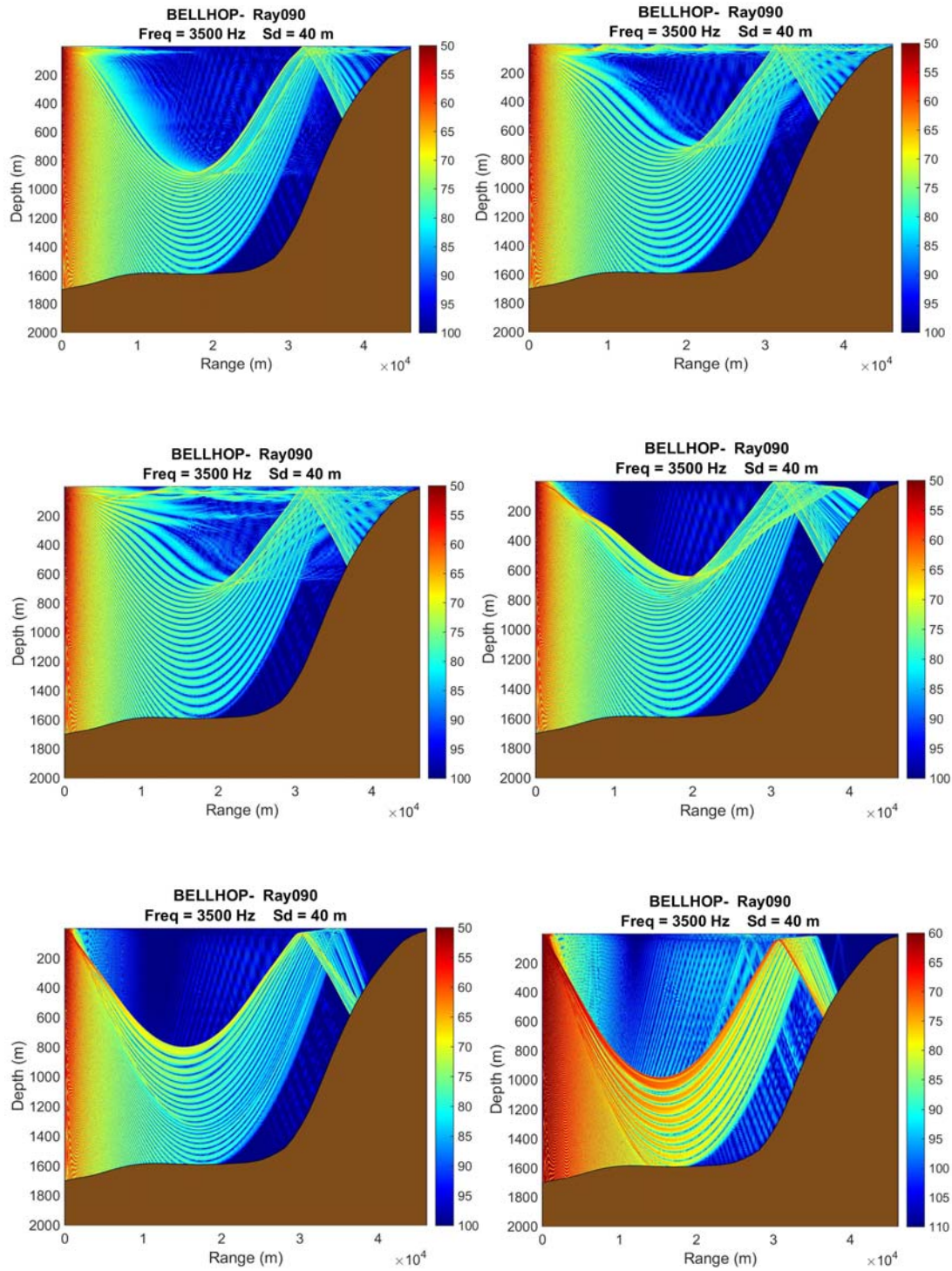
Figure 37.   Monthly Mean TL Calculated from BELLHOP model at Point A
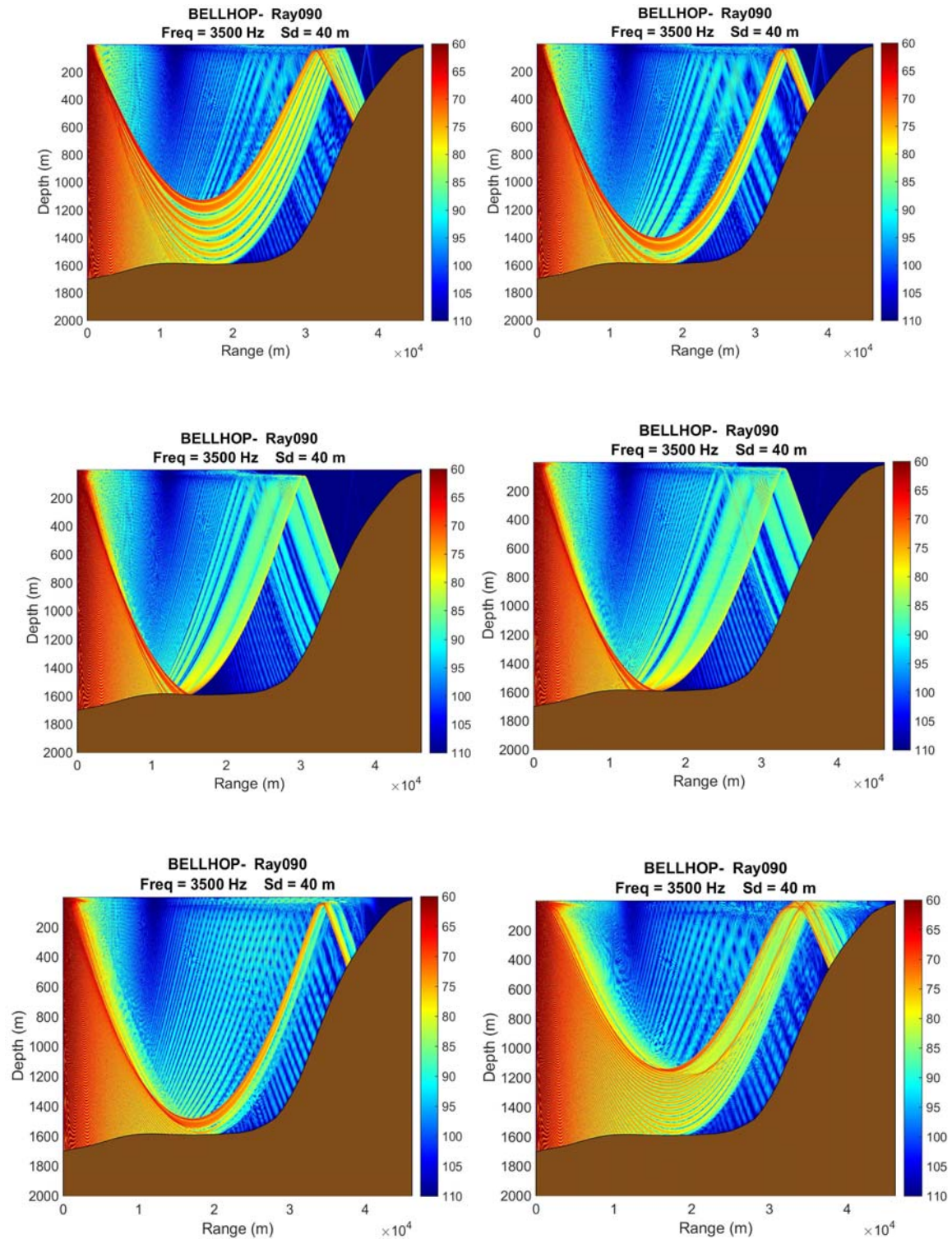
Figure 37 (cont'd.).   Monthly Mean TL Calculated from BELLHOP model at Point A

For September and October, bottom bounce occurred. Sound struck the bottom and reflected upward to the surface at the 25–32 km range. For June and July, there was a very large shadow zone, which extended to a depth of 700 meters within the 32 km range. These results mostly correspond to the convergence zone expected from mean sound speed profiles, but not for sound channel

These convergence zones are of main concern for USW. There are many submarine detection tactics based on convergence zones. Point A provides a high possibility of detecting submarines at long distances.

b.   *Point B*

We expected to see a surface duct in February and sound to bend downward in August. From January through April, a surface duct propagation was modeled along the long distances (Figure 38). After April, the sound started to bend downward due to heating at the surface and bottom-bounce occurred due to the shallow water environment. December exhibited both a surface duct and bottom bounce. These results agrees with what expected from mean sound speed profiles.
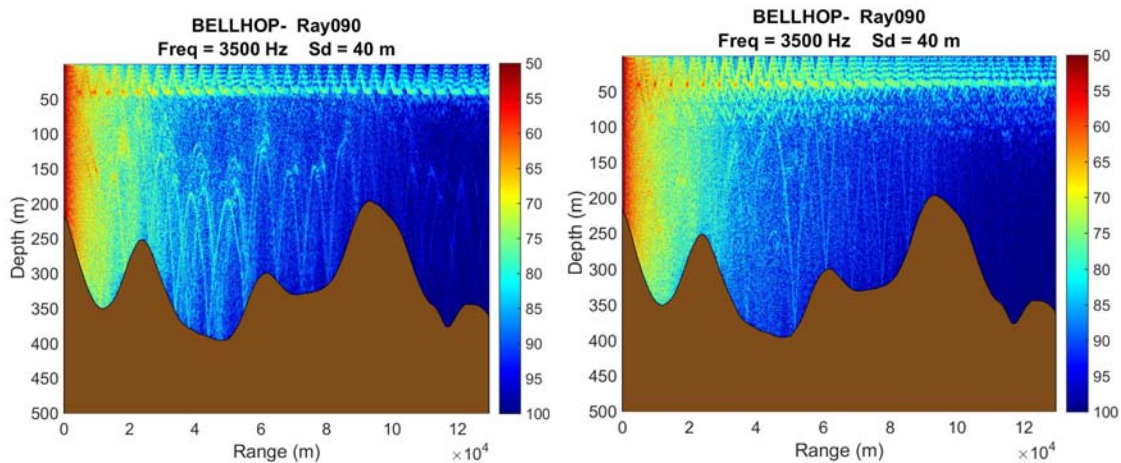
Figure 38.   Same as Figure 37 except for Point B
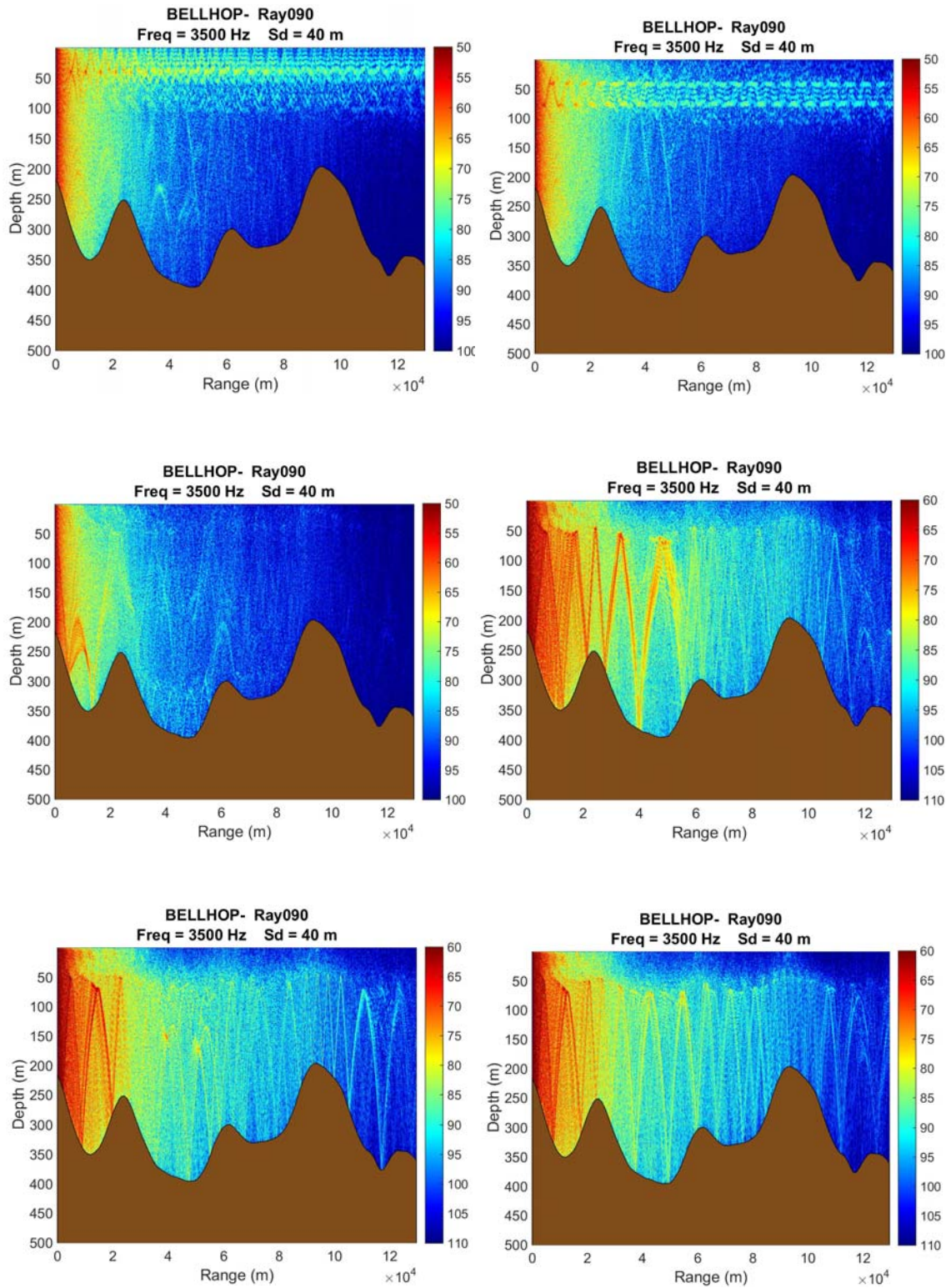
Figure 38 (cont'd).   Same as Figure 37 except for Point B

65
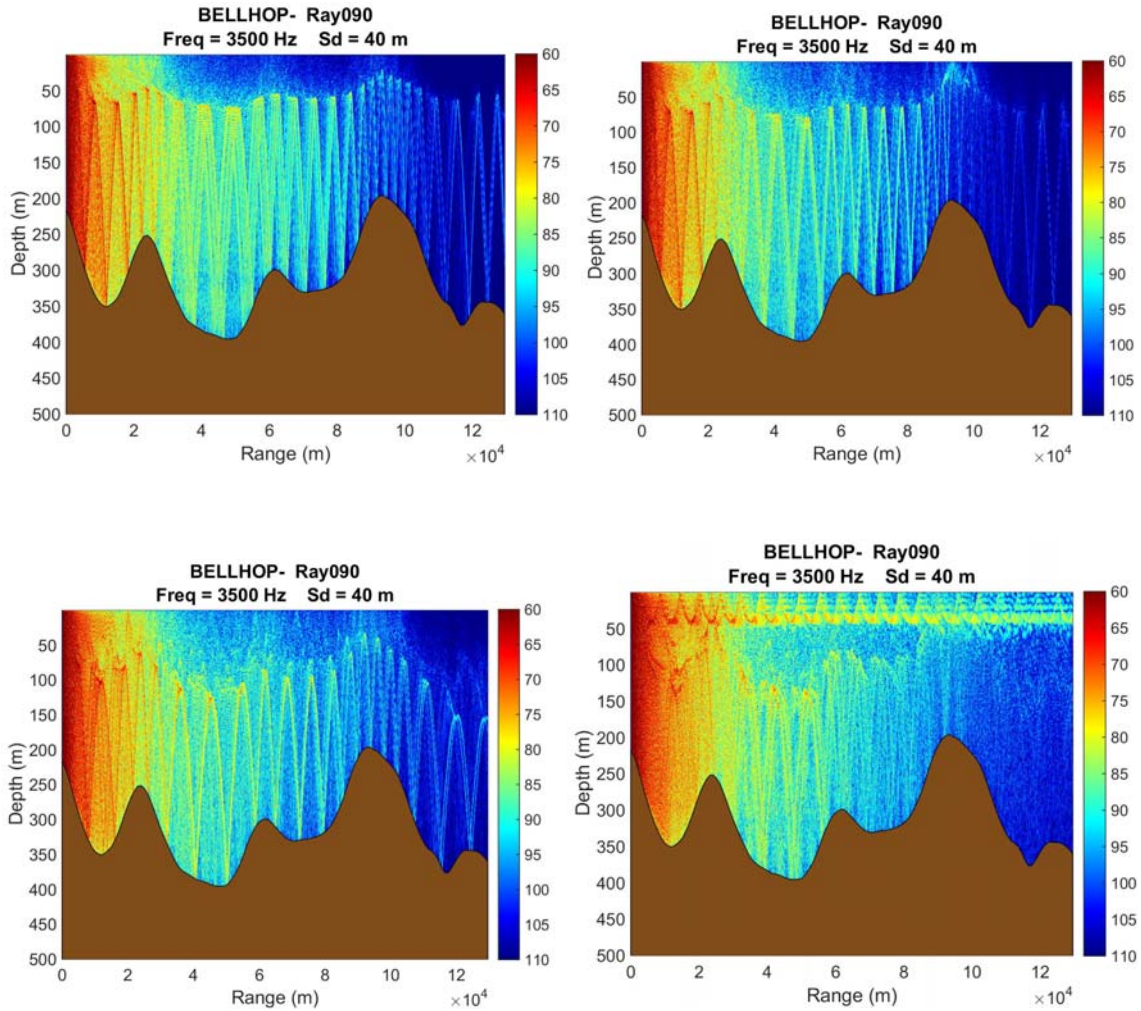
Figure 38 (cont'd).   Same as Figure 37 except for Point B

c.   *Point C*

We expected to see surface duct in March and a sound channel at 400 meters in August. We also expected the convergence zone due to deep layer in Point C. From December through April, there are a surface duct and convergence zones in each figure (Figure 39). The strongest surface duct occurred in March as we expected. However, we did not see a sound channel in August as we expected. From May through November, a convergence zone but no sound channel was detected. The upper limiting ray of convergence zones varied between 500 and 1700 meters; maximum upper limiting ray of the convergence zone took place in September and October, and the minimum upper

limiting ray of the convergence zone occurred in March. Shadow zones, created by convergence zones, would have been a good place to avoid detection.
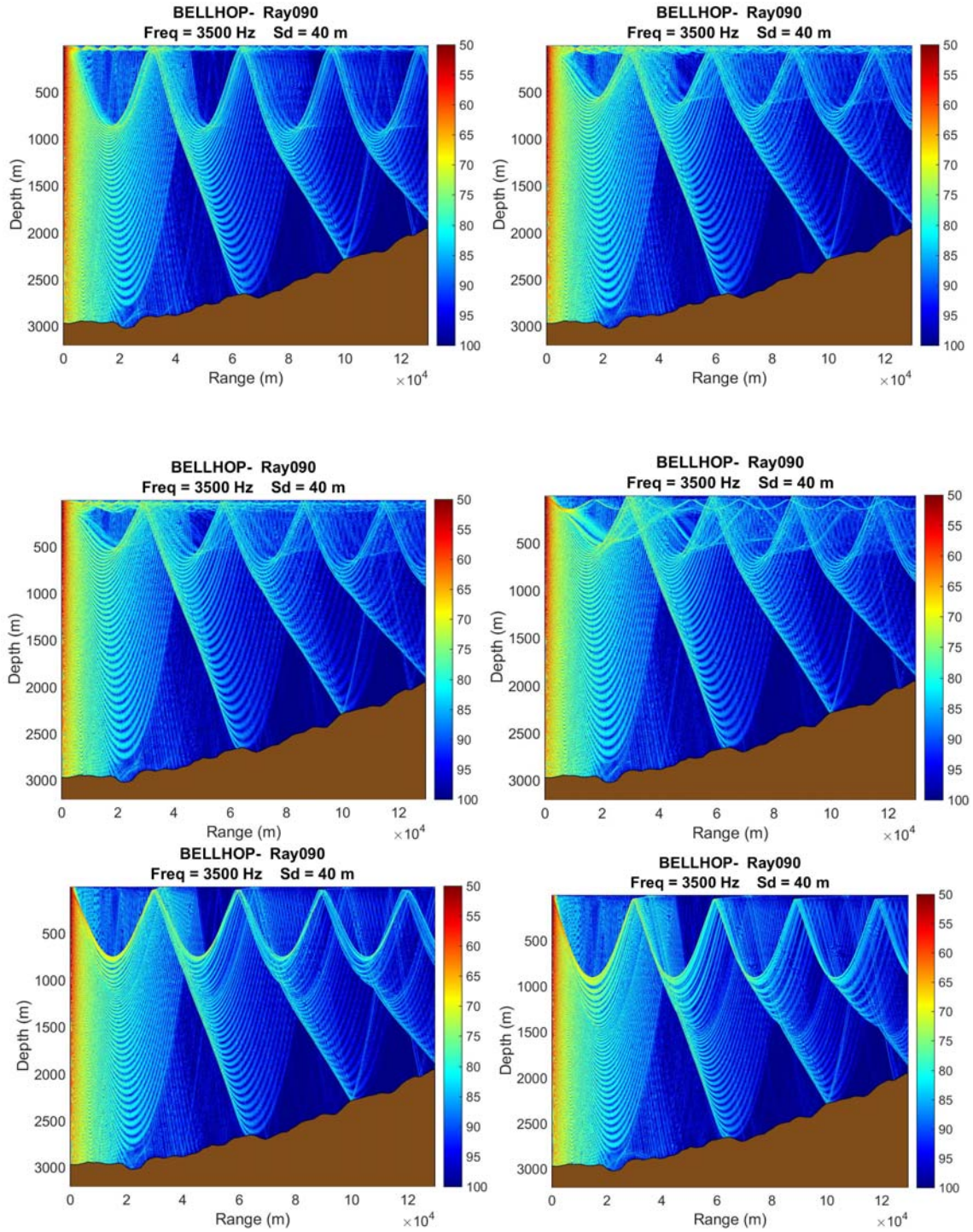
Figure 39.　Same as Figure 37 except for Point C
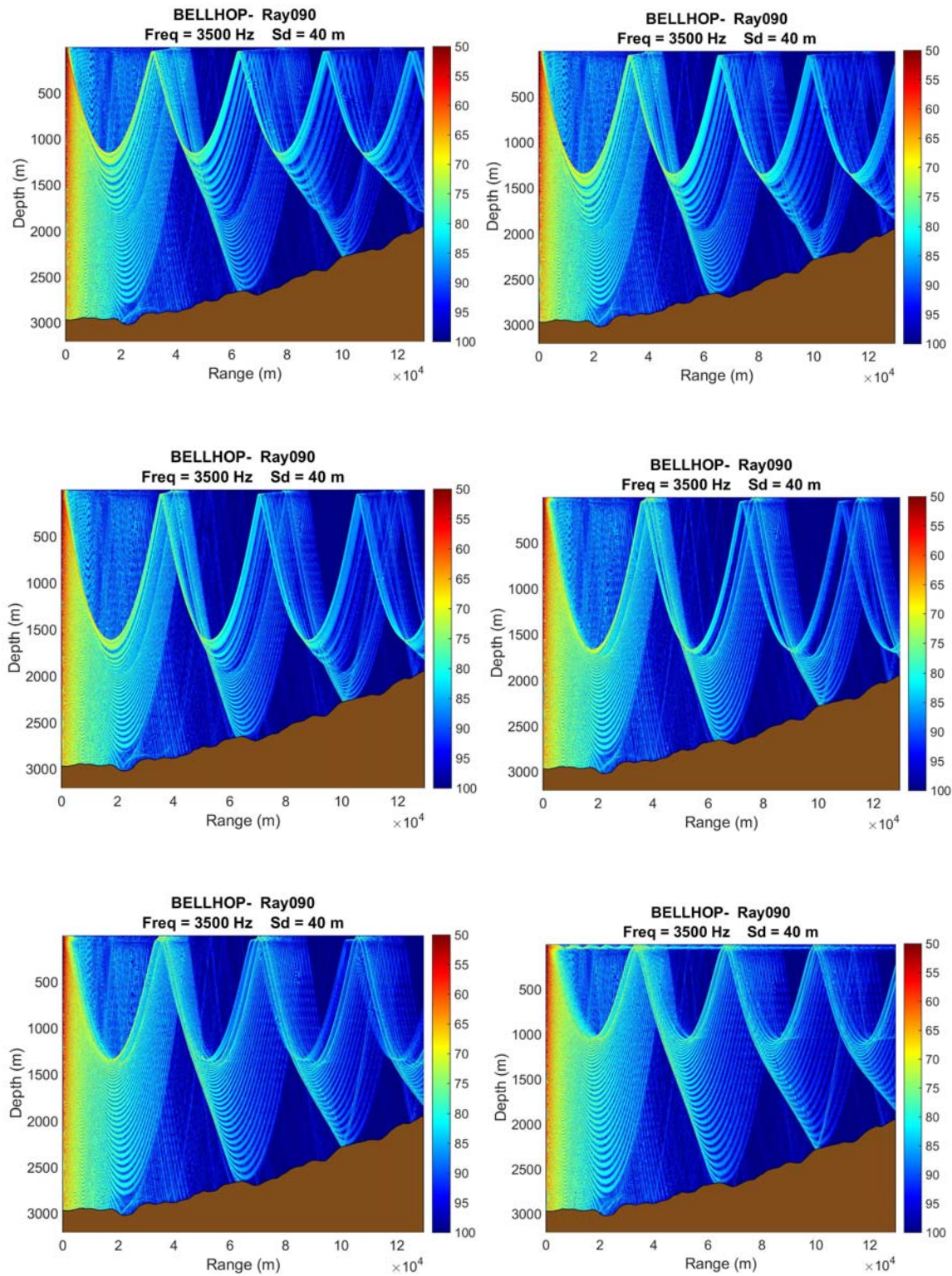
Figure 39 (cont'd).   Same as Figure 37 except for Point C

d. *Point D*
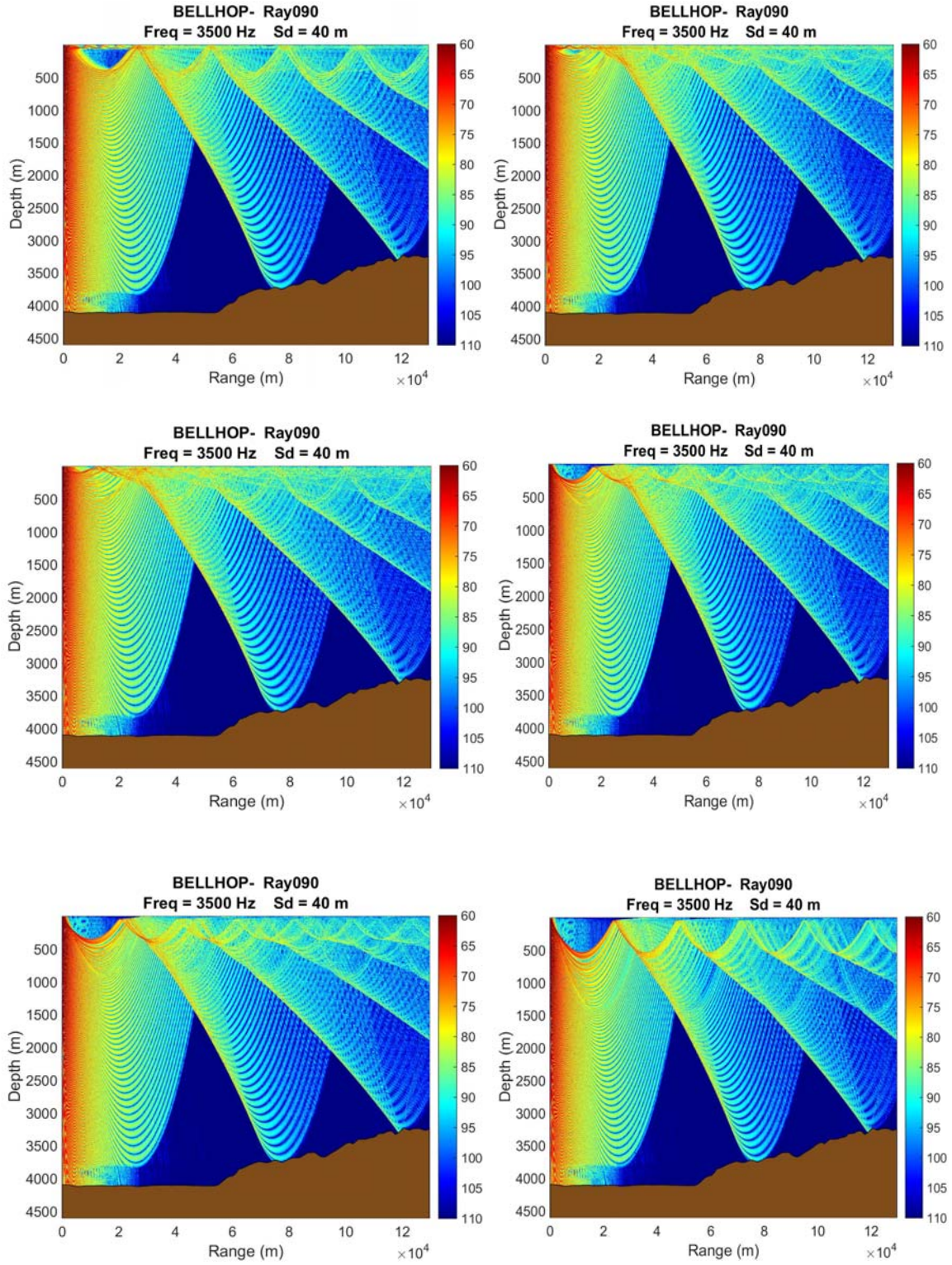
Figure 40.   Same as Figure 37 except for Point D
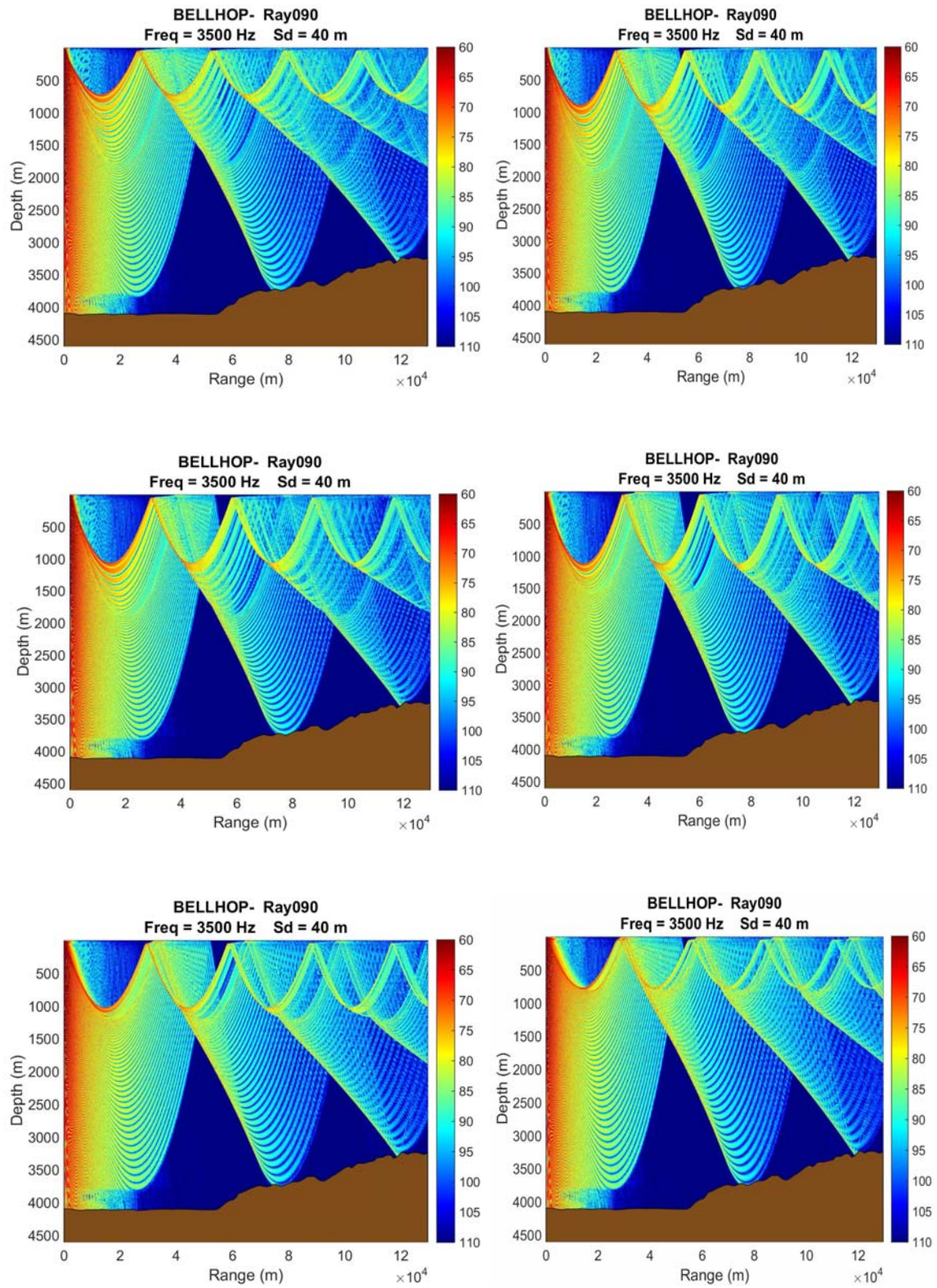
Figure 40 (cont'd.).   Same as Figure 37 except for Point D

From January through March, a surface duct and a deep convergence zone occurred. These results agree with our expectation from the mean sound speed profiles as the Arctic Ocean profile exhibits surface duct and convergence zones together as long as there are deep layers. From April through December, we expected to see a sound channel at a depth of 80 meters in conjunction with convergence zones. However, because of a very sharp negative gradient from surface down to 80 meters, where sound speed reaches its minimum, we only observed convergence zones. The upper limiting ray of convergence zones varied between 300 and 1200 meters; the maximum upper limiting ray of convergence zone took place in September and October, and the minimum upper limiting ray of the convergence zone occurred in April.

e.   *Point E*

In the shallow water, a direct path was modeled (Figure 41). Sound bends downward and bounced from the bottom to the surface. The 20 km range exhibited a deep layer, and a surface duct emerged from January through March due to low speed at the surface. In April, surface sound channels took place at the 100 meters. From May through December, the sound channel deepens, and a weak sound channel occurs at 200 meters. However, the TL was significant in these sound channels. The surface duct and sound channels are not as strong as those occurring in January through May. Thus, would have been possible to detect submarines at the surface at very long distances from January through April, but not from May through December.
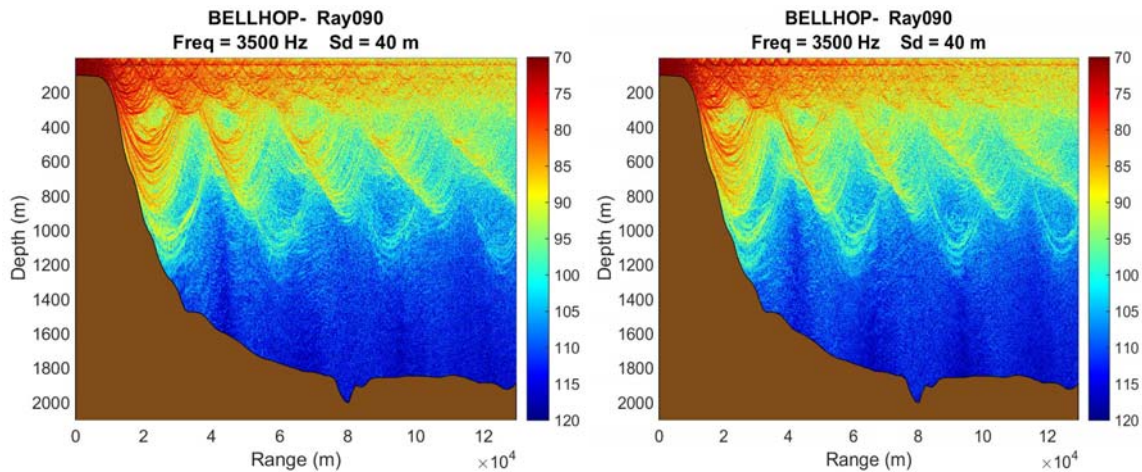
Figure 41.   Same as Figure 37 except for Point E
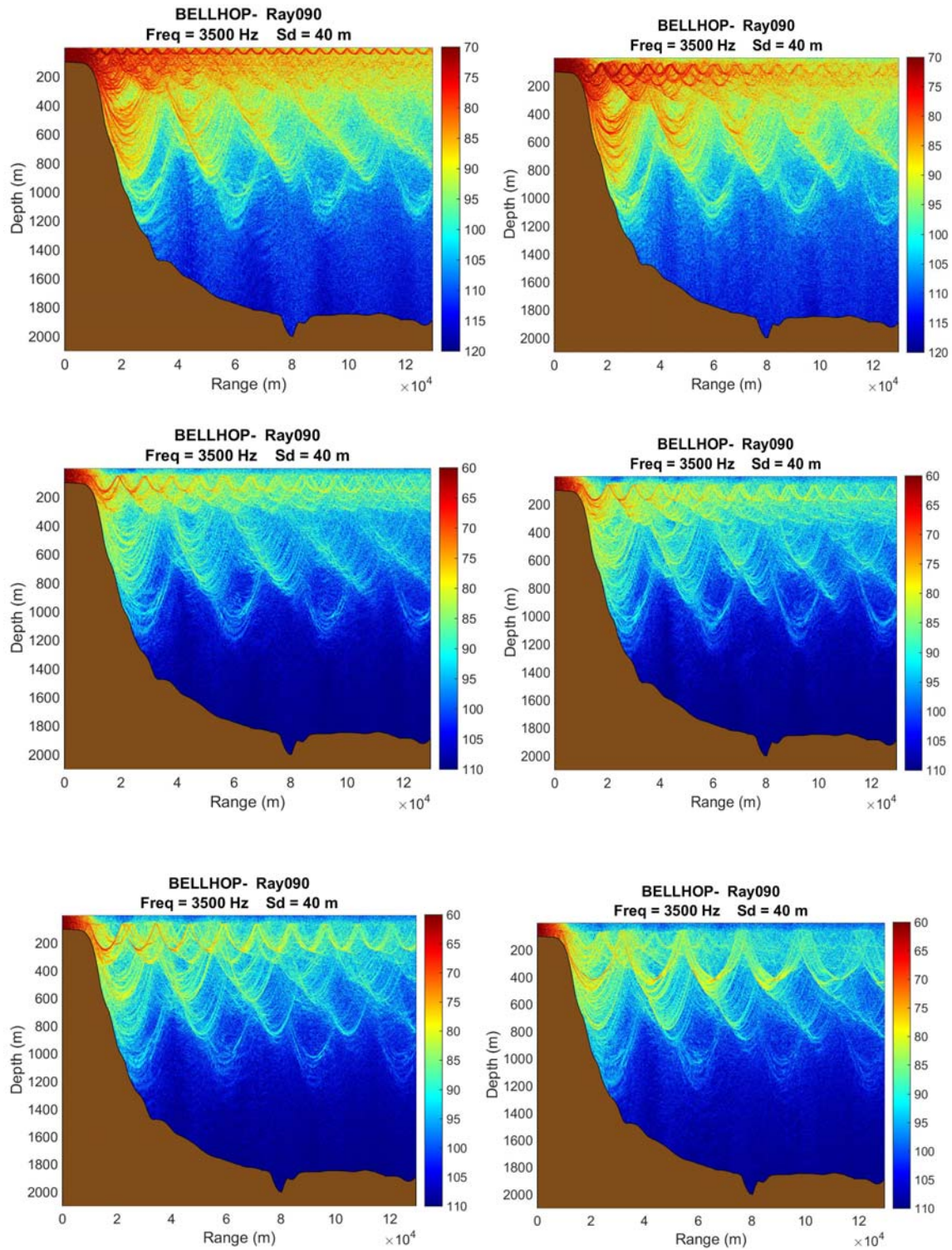
Figure 41 (cont'd.).   Same as Figure 37 except for Point E
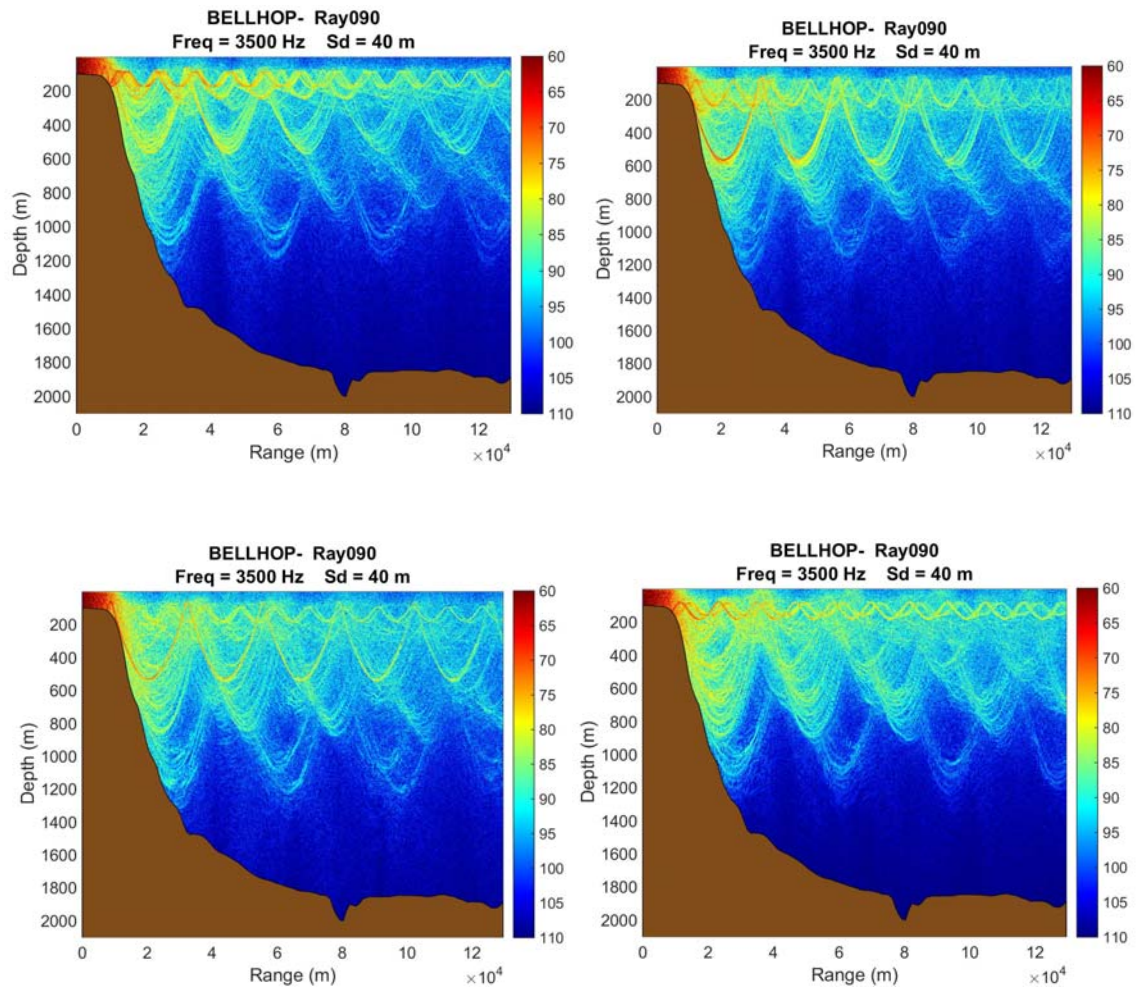
Figure 41 (cont'd.).   Same as Figure 37 except for Point E

2. GDEM AND SMG-WOD COMPARISON

January and August have been chosen to analyze the range and patterns of sound propagation, as well as TL. In Figures 41–46, GDEM modeling results are shown in the left panels, and the SMG-WOD modeling results are shown in the right panels.
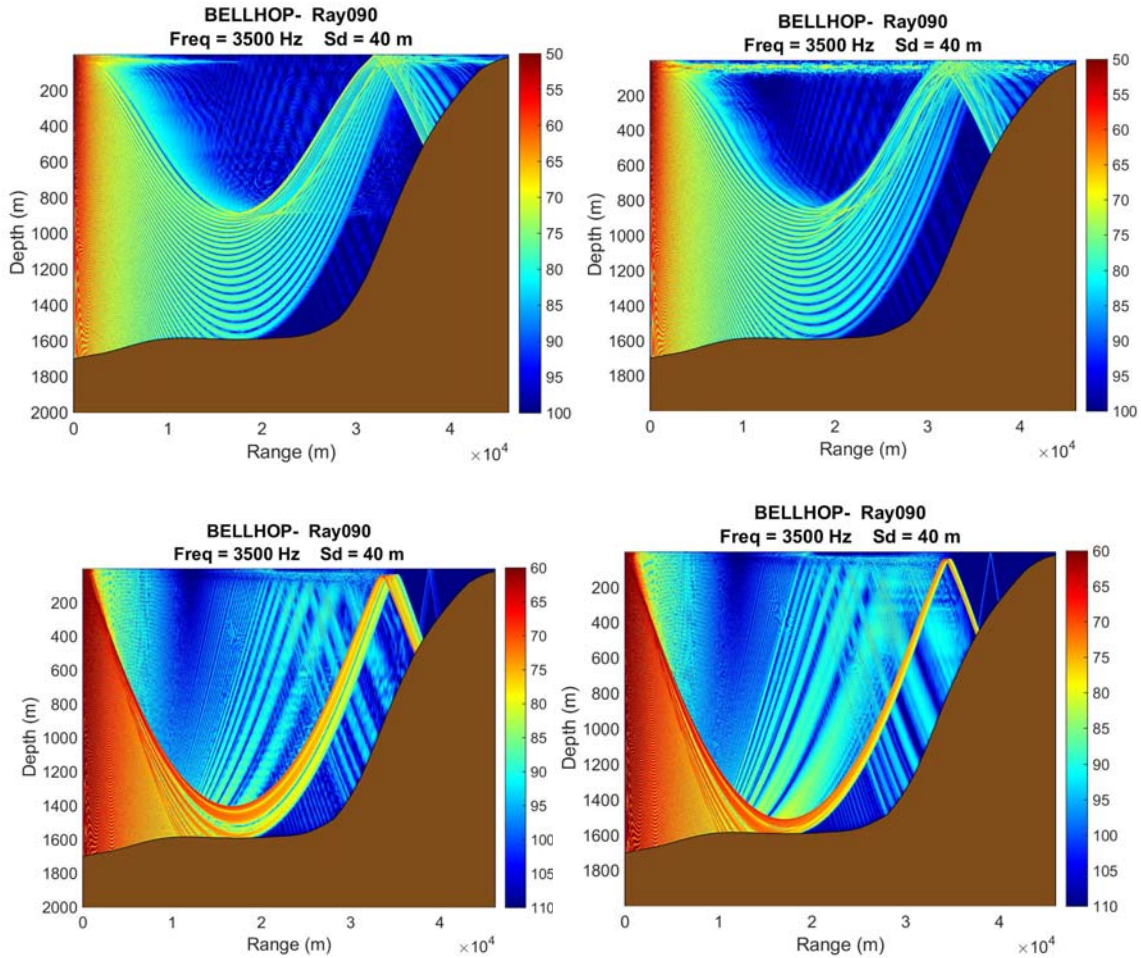
Figure 42.   Point A January (upper) and August (lower)

At the point A location in January (Figure 42, upper panels), the sound propagation patterns were similar to each other. The SMG-WOD (right) exhibited surface duct propagation along the 45 km range. However, the GDEM (left) only showed a surface duct up to the 17 km range, but it exhibited another surface duct after the convergence path at the 32 km range. The upper and lower limiting rays of convergence

between the datasets were in agreement. However, there was a slight difference between their TLs in the shadow zones. The GDEM reflects a slightly lower TL in the shadow zones. In August (Figure 42, lower panels), sound propagation patterns were similar to each other. However, there was a slight difference in TL in the direct path. The upper limiting ray of the convergence zone was 150 meters deeper in SMG-WOD (right) than in the GDEM (left). Lower TL is modeled with SMG-WOD in shadow zones. In August (Figure 43, lower panels) higher attenuation is modeled at surface, and lower attenuation is modeled in the deep layer. Both the datasets produced shorter propagation ranges in August than in January.
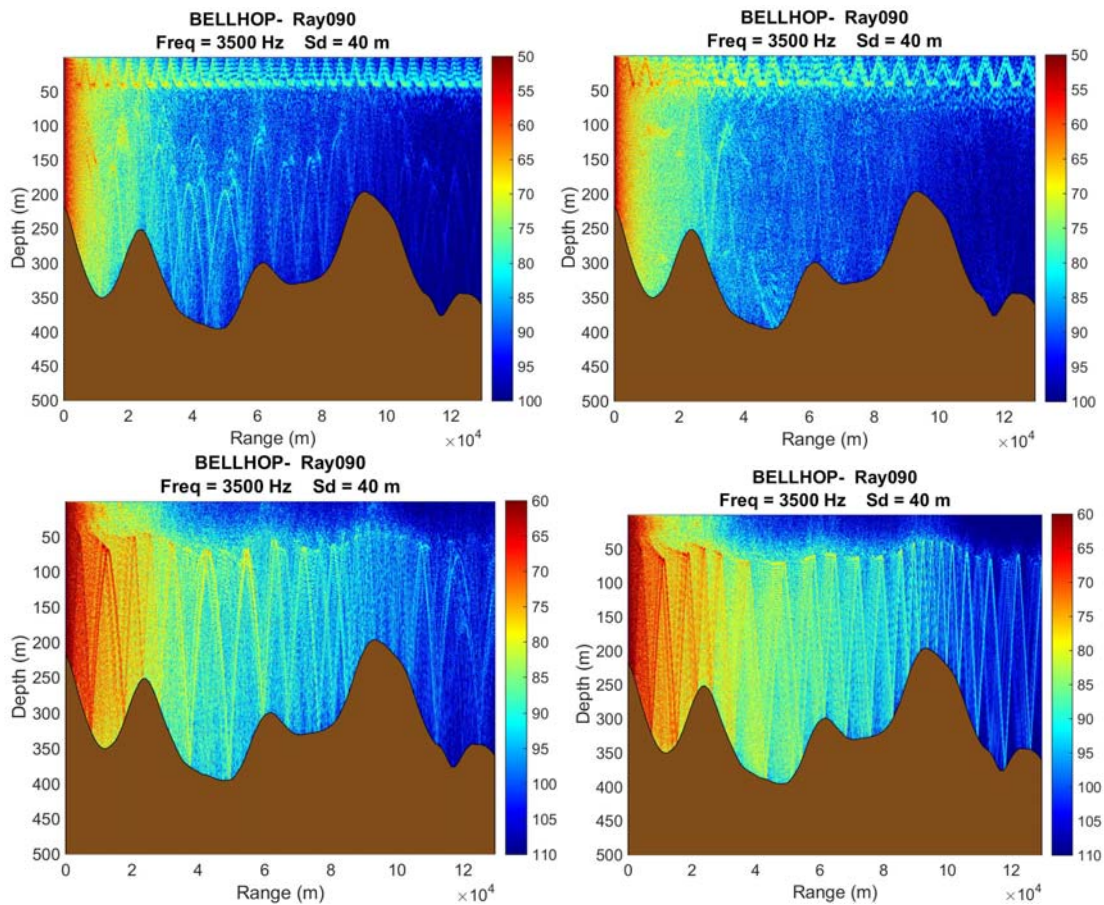
Figure 43.   Point B January (upper) and August (lower)

At the point B location in January (Figure 43, upper panels), sound propagation patterns were similar to each other. Both models produced a surface duct at the same depth and range. After the 22 km, a bottom bounce pattern was observed for both the models; however, GDEM (left) exhibited a clearer bottom bounce regime. TL was almost the same in both the models. Additionally, SMG-WOD (right) exhibited a surface duct with thicker profiles. In August (Figure 43, lower panels), the sound propagation patterns were very much like for both the datasets. The bottom bounce pattern was observed in each figure and there was no surface duct after the 38 km range at the surface. The GDEM (left) exhibited a clearer bottom bounce regime, and TL was somewhat higher in GDEM. The SMG-WOD bottom bounce pattern (right) propagates further than the GDEM with thicker sound profiles. In August, higher attenuation values occurred at the surface and lower attenuation occurred in the deep layer, which produces shorter ranges than in January.
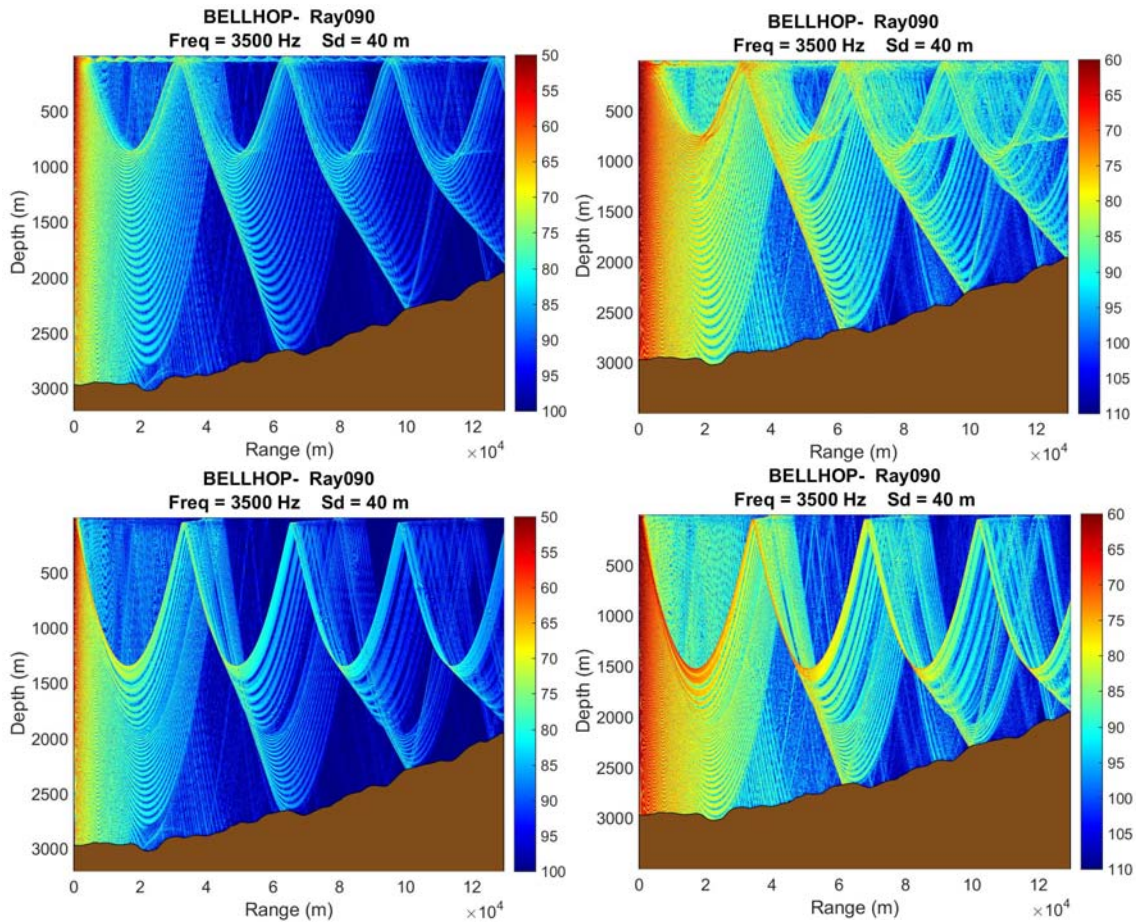
Figure 44.   Point C (upper) and August (lower)

At the point C location in January (Figure 44, upper panels), both the datasets produced the similar surface duct and convergence zones with only a slight difference in TL (exaggerated because of different colorbars). Additionally, the SMG-WOD (right) showed a surface duct with thicker profiles. In August, both the models produced similar convergence zones with a light difference in TL. In August, there are higher attenuation values at the surface but lower attenuation in the deep layer, which results in shorter ranges than January.
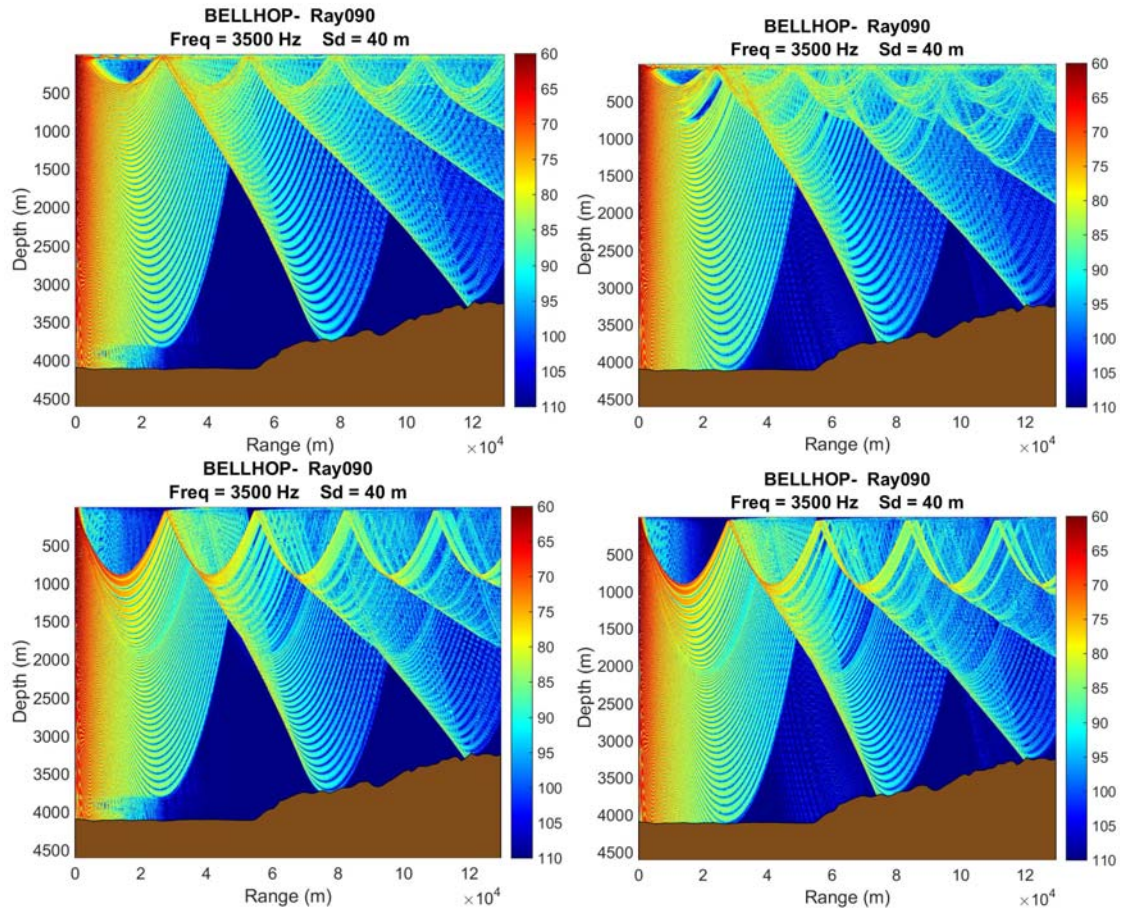
Figure 45.   Point D (upper) and August (lower)

At the point D location in January (Figure 45, upper panels), both the datasets produced a surface duct, sound channel and convergence zones; however, there are some notable differences. The maximum lower limiting ray of the convergence zone extended deeper in the SMG-WOD (right) at the 22 km range. There was also a higher the TL in shadow zones in GDEM (left). After the 40 km range, there were different types of

convergence zones in the SMG-WOD. In August (Figure 45, lower panels), the maximum lower limiting ray of the convergence zone extended deeper in the SMG-WOD at the 22 km range. The GDEM had a higher TL in deep shadow zones but lower TL in surface shadow zones. The maximum lower limiting ray of the convergence zone extended deeper in SMG-WOD than in the GDEM in the bottom layer
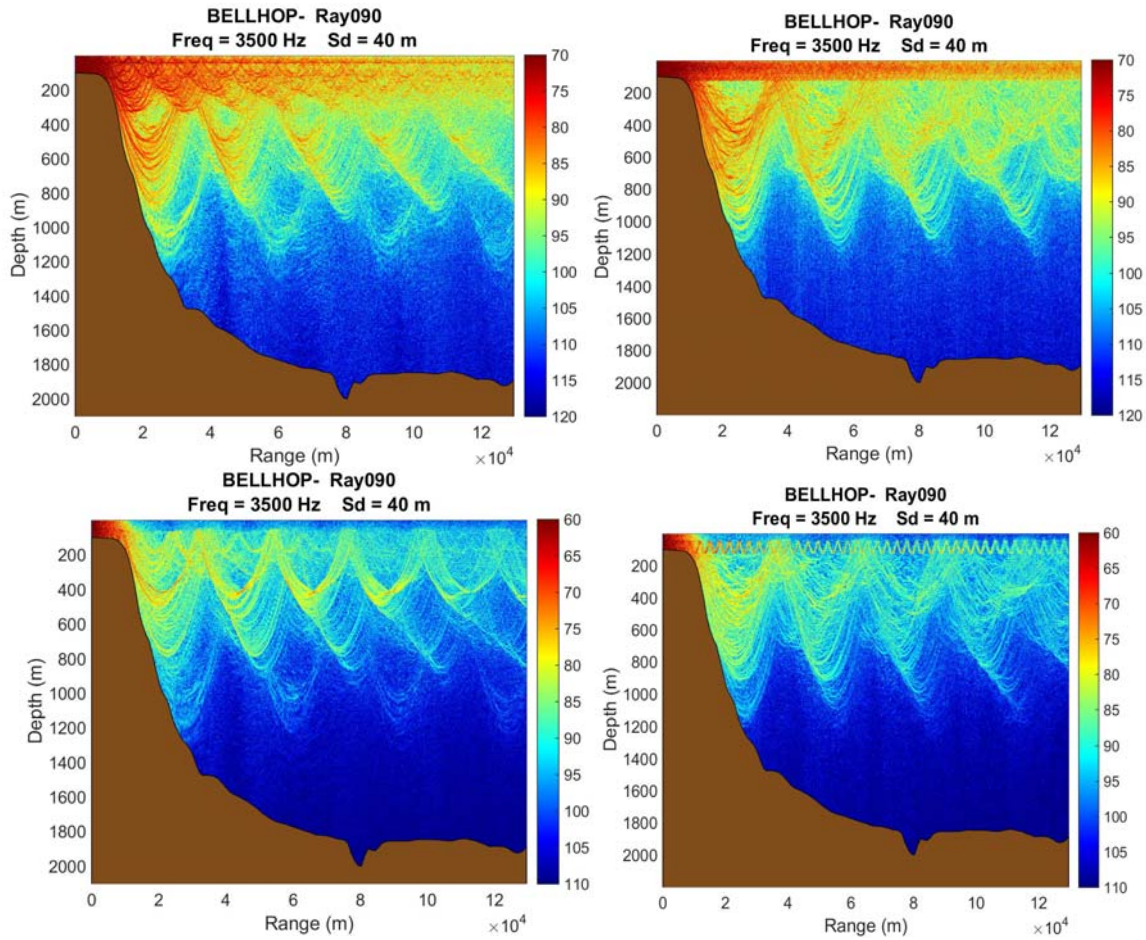
Figure 46.   Point E (upper) and August (lower)

At the point E location in August (Figure 46, lower panels), the sound propagation patterns were similar to each other. Both of the figures show a surface sound channel and convergence zone. The direct path took place in shallow water. Then, a weak sound channel occurred at 200 meters. The SMG-WOD (right) exhibited lower TL in the sound channel and higher TL in the convergence zone. The lower limiting ray of convergence zones penetrated deeper in GDEM than in SMG-WOD.

78

VI. INTERANNUAL VARIABILITY

A. TIME VARIATIONS OF (T, S, SS) PROFILES

Temperature, salinity, and sound speed profiles at the five selected locations are described in this section. The (T, S) data are obtained from the SMG-WOD dataset and the SS profiles are calculated using the Medwin equation.

1. Temperature

Figures 47–51 showed temporal variability of SMG-WOD temperature from 1960–2014 with one-month resolution for points A-E. The temperature profiles at all the locations exhibit strong seasonality associated with surface heat fluxes and variations in the vertical structure of water column. However, this seasonality was strongly modulated by inter-annual and decadal variability as described below for each location.
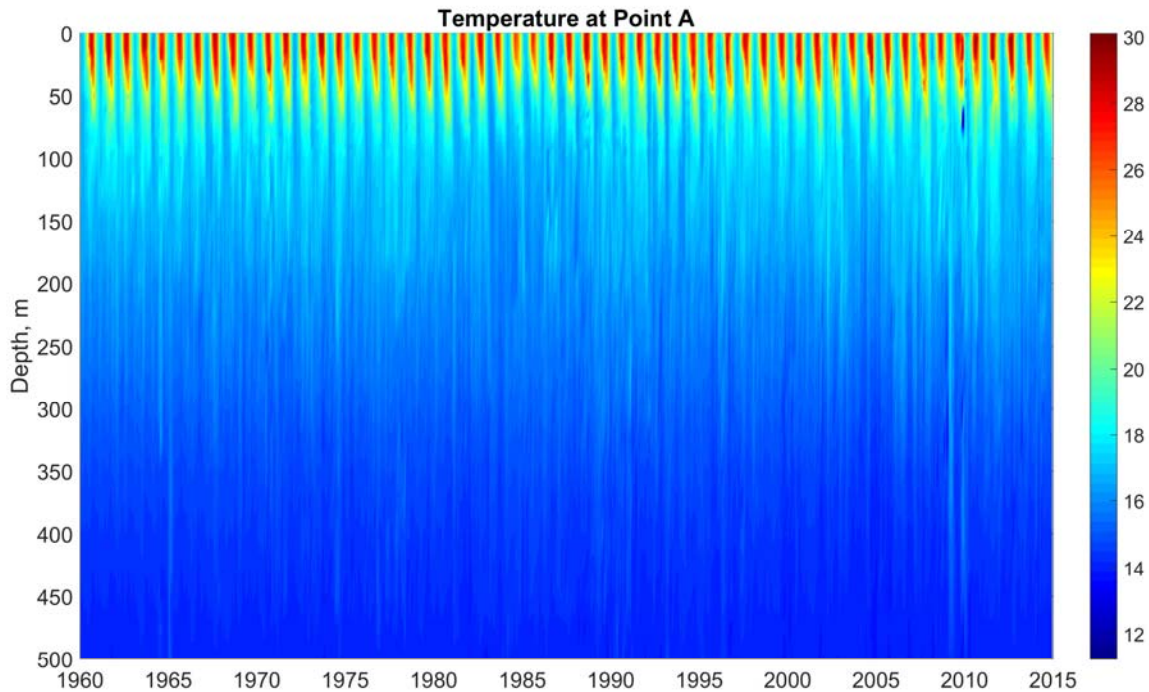
Figure 47.   Temporal Variability of SMG-WOD Temperature at Point A

At point A (Figure 47) the inter-annual variability is evident in the variations of summer temperatures at sea surface, the depth of the mixed layer and the strength of the thermocline. The temperature was colder between 1980 and 1990 at the surface and in the intermediate layer, with shallower summer mixed layer observed in 1985–1986. The temperature increased between 1990 and 2014. Temperature between 1960 and 1980 was also warmer than 1980 to 1990, however, it was not warmer than period between 1990 and 2014. Strong variations of temperature with higher temperatures propagating down to 500 meters were observed in 2009–2010.
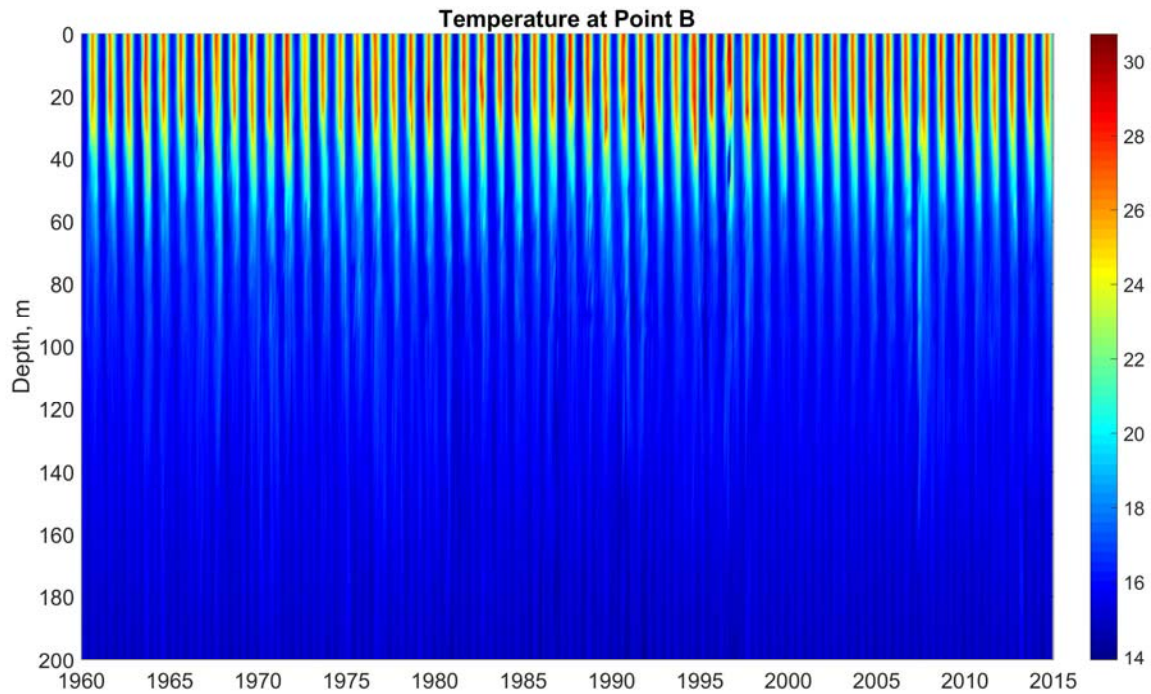
Figure 48.   Temporal Variability of SMG-WOD Temperature at Point B

Point B shows some important variations between specific years (Figure 48). Temperature at the surface between 1997 and 1998 was warmer than in other years. Also, warmer water between 2007 and 2008 extended down to 180 meters.
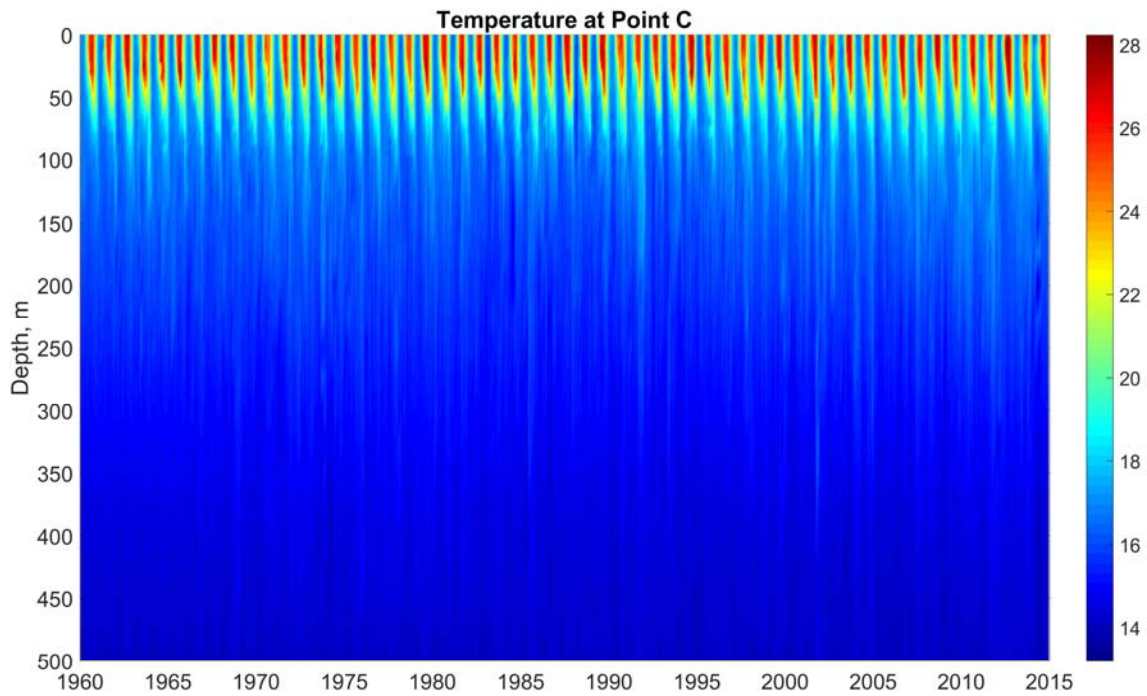
Figure 49.   Temporal Variability of SMG-WOD Temperature at Point C

At Point C (Figure 49) the temperature at the surface exhibited a strong decadal variability. Especially between 2000 and 2014, the surface water gets warmer and this warmer water penetrate to deeper layers than in other years. An anomalously deep penetration of warm water down to 300 meters was observed during summer 1992. Interestingly, it was accompanied by colder than usual surface temperature and rather shallow mixed layer at the end of spring. An anomalously warm surface water but no deepening of the warm surface layer was observed during the summer 2012
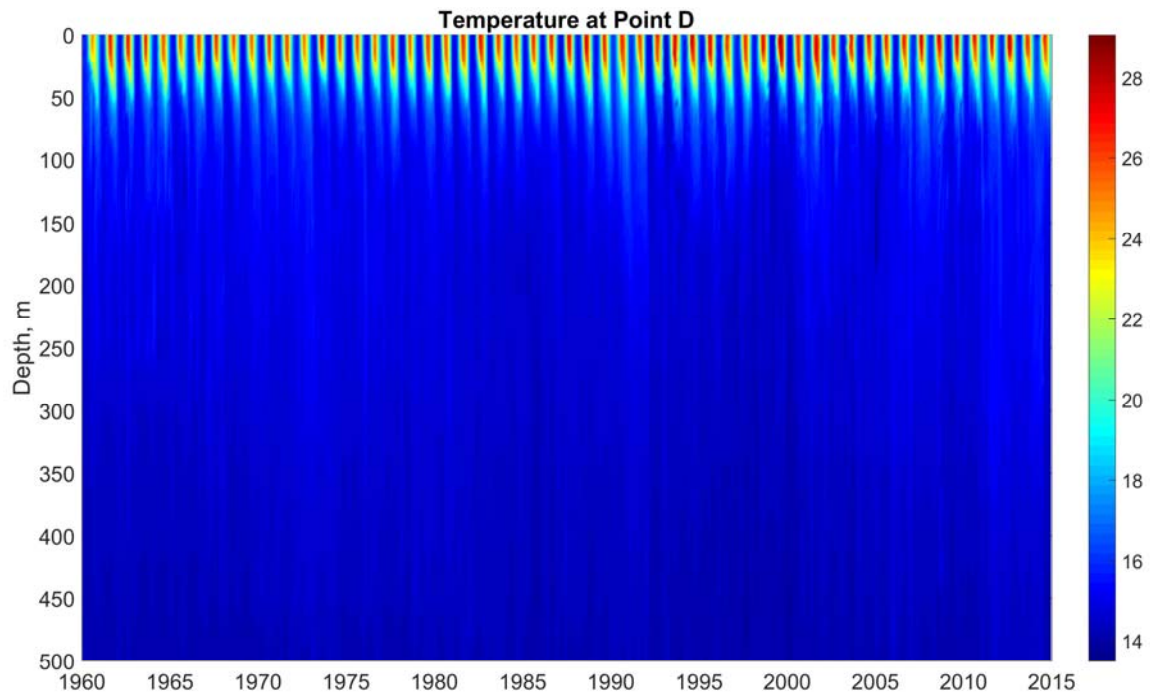
Figure 50.   Temporal Variability of SMG-WOD Temperature at Point D

At Point D (Figure 50), a strong contrast existed in summer surface temperatures before and after 1980. The temperature at the surface started to increase after 1980. Before the 1980, the surface water is about 24 °C. Then it gets warmer at the surface and reaches 29 °C. Between 2000 and 2014 years, the warmer water starts to penetrate down to 400 meters.
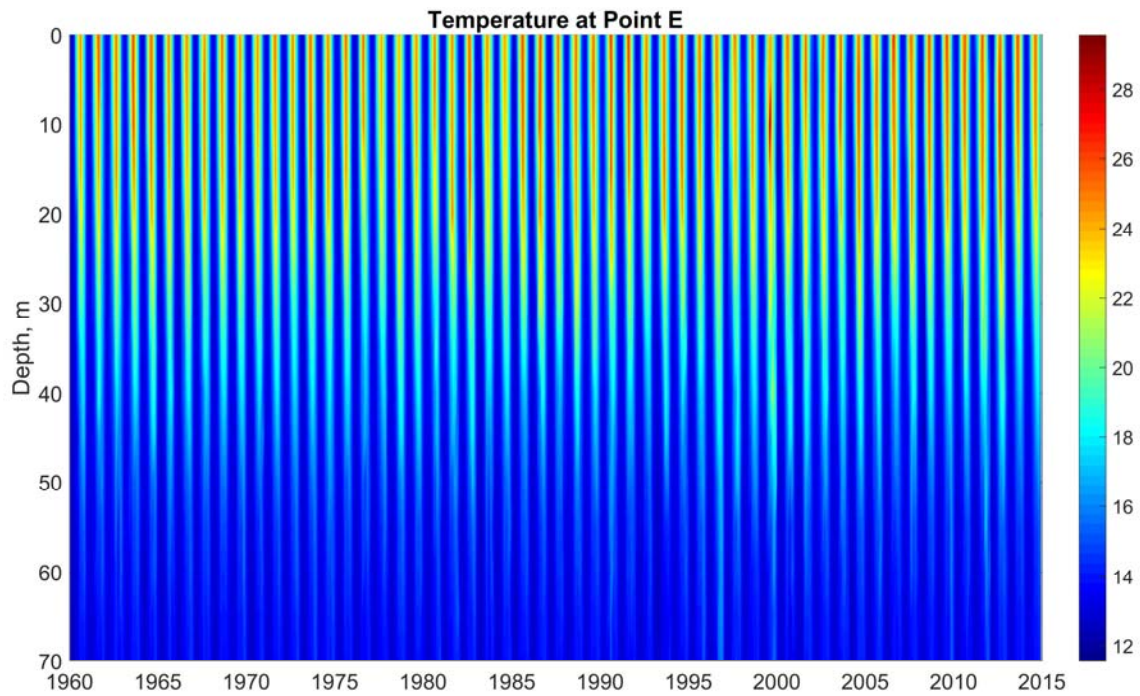
Figure 51.   Temporal Variability of SMG-WOD Temperature at Point E

Temperature increased between 1990 and 2014. The waters between surface and a depth of 20 meters reached the higher temperature than previous years; however, the warmer water penetrated to deeper layer between 1997 and 1998. Sea surface temperatures between 1960 and 1990 were lower than later decades.

2.   Salinity

Figures 52–56 show temporal variability of SMG-WOD salinity from 1960–2014 with one-month resolution for points A-E. While some seasonality is seen in the salinity profiles, the inter-annual and decadal variability is much stronger, most likely associated with inter-annual and decadal variability of freshwater fluxes and water mass formation.
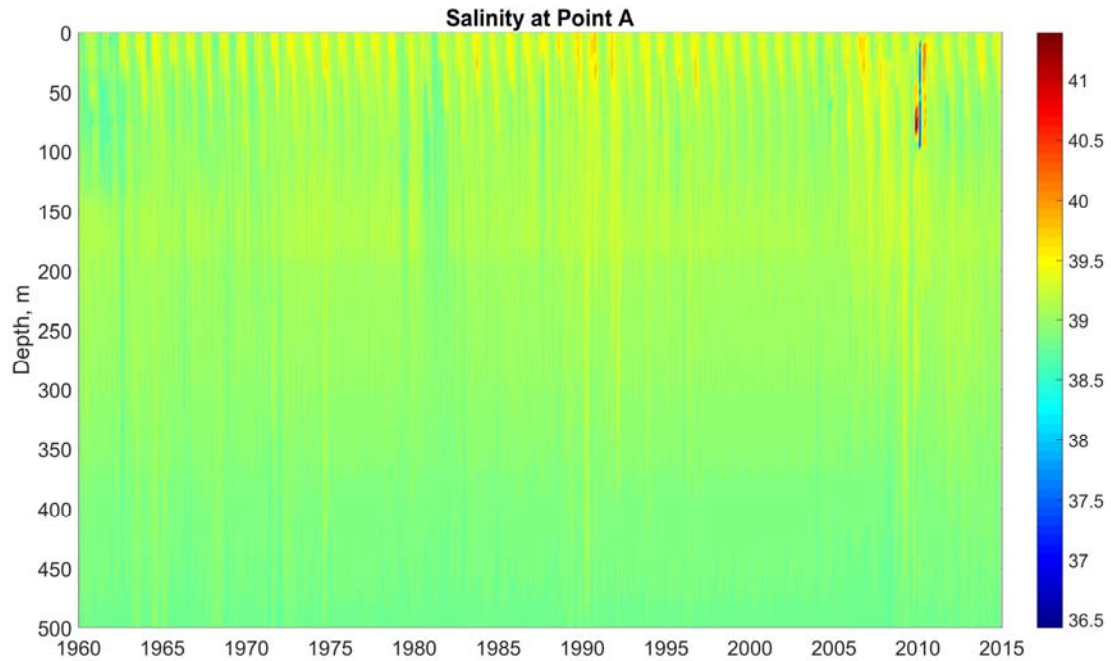
Figure 52.   Temporal Variability of SMG-WOD Salinity at Point A

The salinity showed inter-annual variations between 1960 and 2014 (Figure 52). Overall, point A is becoming saltier from 1960s. The inter-annual and decadal variability at this location seems to be synchronized with the inter-annual variability of temperature (Figure 47). Specifically, the salinity increased between 1990 and 1995, and between 2008 and 2014. It did not increase between 1995 and 2008.
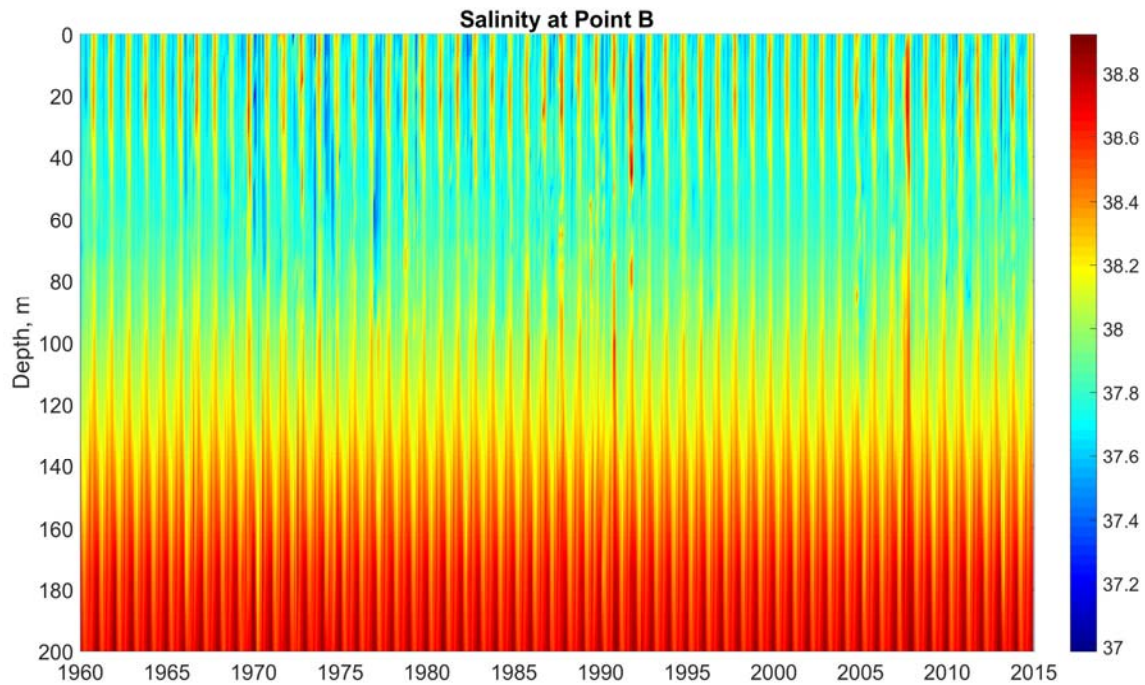
Figure 53.   Temporal Variability of SMG-WOD Salinity at Point B

Point B has saltier water below about 80 m (Figure 53). That must be due to less saline Modified Atlantic Water at the surface. The salty layer exhibited a very robust seasonality with an episodic increase in salinity in 2007. At the surface, there is high inter-annual variations in salinity; however, the salinity did not show steady increase between 1960 and 2014. The salinity decreased at the surface at some years between 1970 and 1990. These values were lower than values between 1960 and 1970. After 1990, the salinity increased, especially between 2007 and 2008.
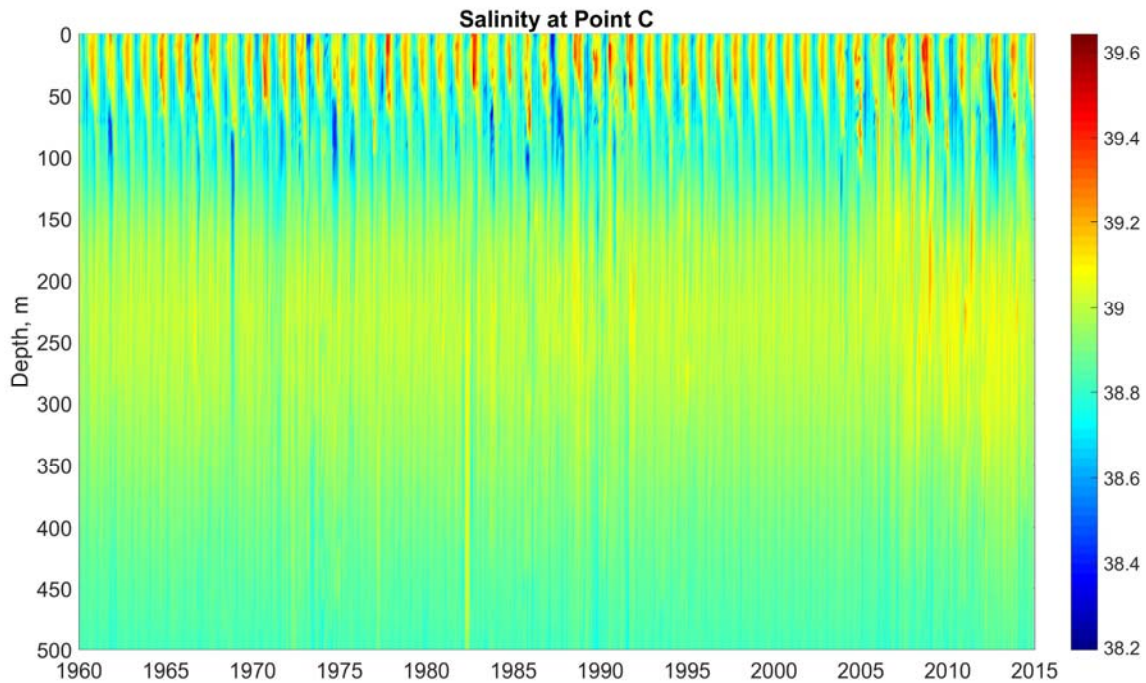
Figure 54.   Inter-annual Salinity Variations at Point C

At point C, a three-layer structure was observed with highly seasonal upper layer down to about 50 meters on average, salinity minimum between 50 and 100 meters and a saltier water below (Figure 54). The upper layer demonstrated higher salinity during summer associated with high evaporation. The inter-annual variability in surface heat and freshwater fluxes drove inter-annual variability in the upper layer, except between 1990 and 2005. 2005–2010 was probably the most anomalous period with extremely high salinity at sea surface and several fresh water intrusions below 50 meters. After 2005, salinity also started to increase below 150 meters.
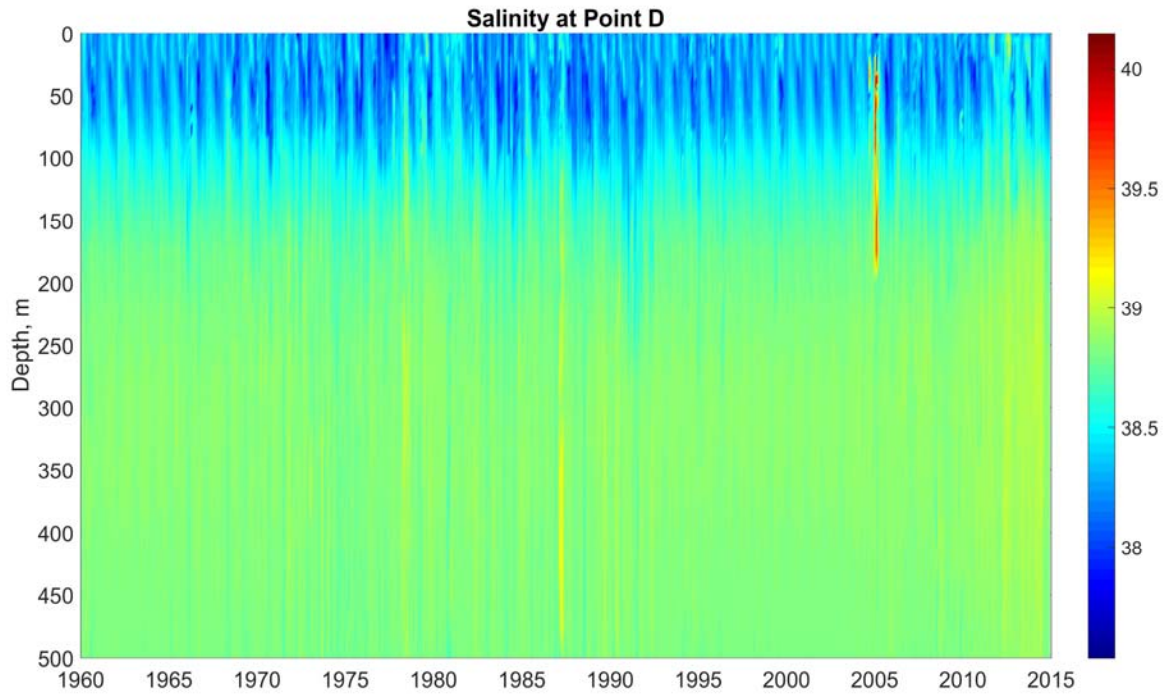
Figure 55.   Temporal Variability of SMG-WOD Temperature at Point D

At point D (Figure 55), there is an apparent two-layer haline structure with fresher layer of about 100 meters thick laying on top of the water column. The two layers were separated by rather strong halocline. While some seasonality is evident in the upper layer, there were high inter-annual variations between surface 100-meter layer and the rest of the water column. The salinity at the surface decreased between 1980 and 1995. After 1995, the salinity started to increase. It reached its maximum value at 2007. The salinity increases in all layers between 2010 and 2014. The deep layer showed its highest inter-annual variations between 2010 and 2014. In 2005 an intrusion of salty water was seen in the subsurface layer between 30 and 200 meters.
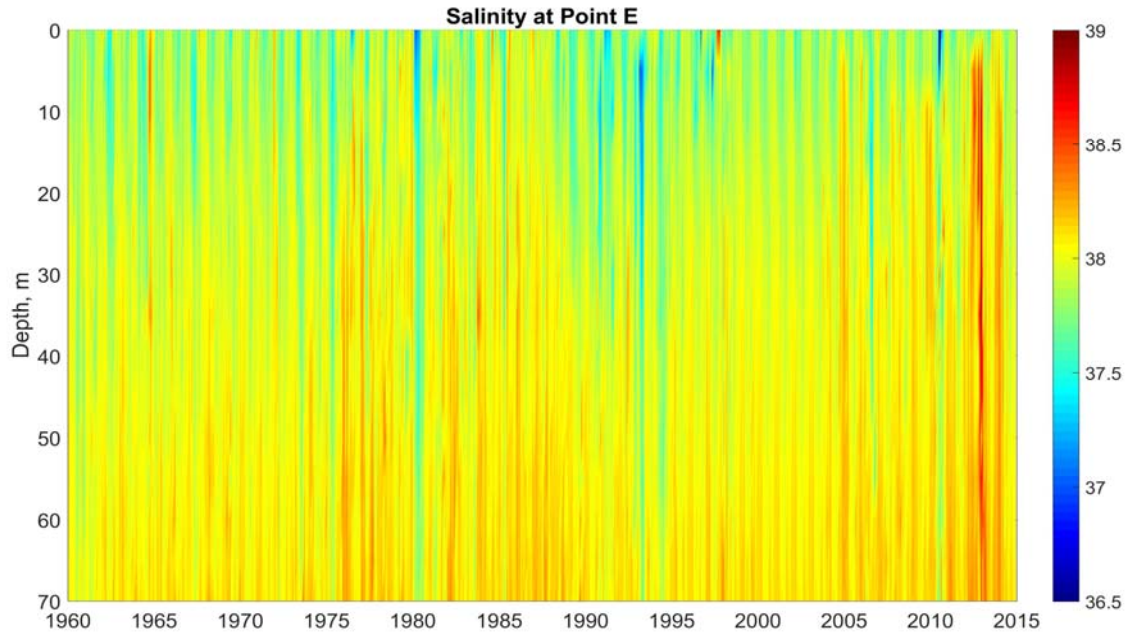
Figure 56.   Temporal Variability of SMG-WOD Temperature at Point E

Point E (Figure 56) exhibits high inter-annual variability in all depths. After 1975, the salinity started to increase until 1990. It decreases rapidly between 1990 and 1995. After the 1995, the salinity started to increase again in all layers. The salinity reached its maximum value between 2010 and 2014. Besides these long-term trends, occasional intrusions of anomalously fresh water in 1980, 1993 and 2011.

3.   Sound Speed

Figures 57–61 show temporal variability of SMG-WOD sound speed from 1960–2014 with one-month resolution for points A-E. Comparison of sound speed (Figures 57–61) and temperature (47-51) variability shows that the upper layer sound speed is determined by temperature as expected, while the lower level is determined by the pressure and shows neither seasonal nor inter-annual variability. It is however expected that strong inter-annual variability of salinity will affect the inter-annual variability of sound speed.
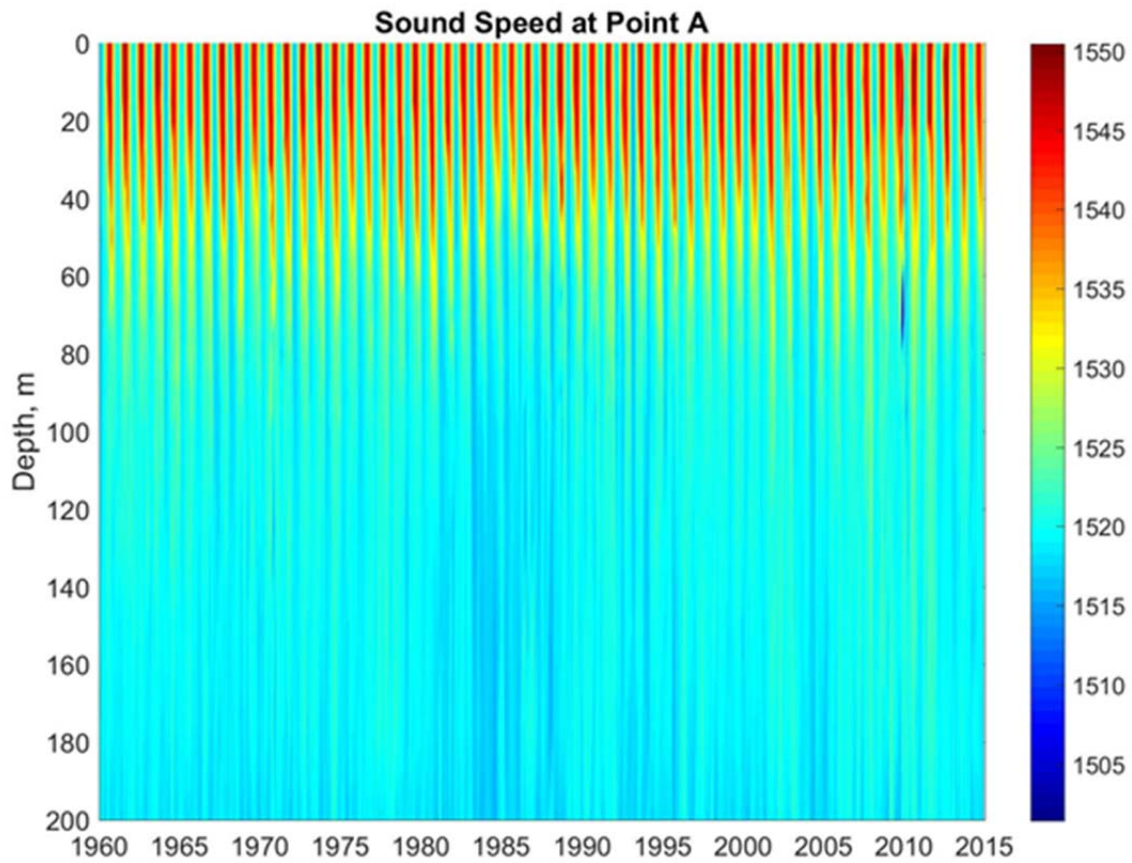
Figure 57.   Temporal Variability of SMG-WOD Sound Speed at Point A

At point A (Figure 57) the sound speed at the surface was almost same. Below a depth of 40 meters, the sound speed shows higher inter-annual variations. The sound speed decreases between 1980 and 1990. The sound speed reaches its maximum values between 2000 and 2014. These results agreed with temperature and salinity results of Point A because both of them increases between 2000 and 2014.
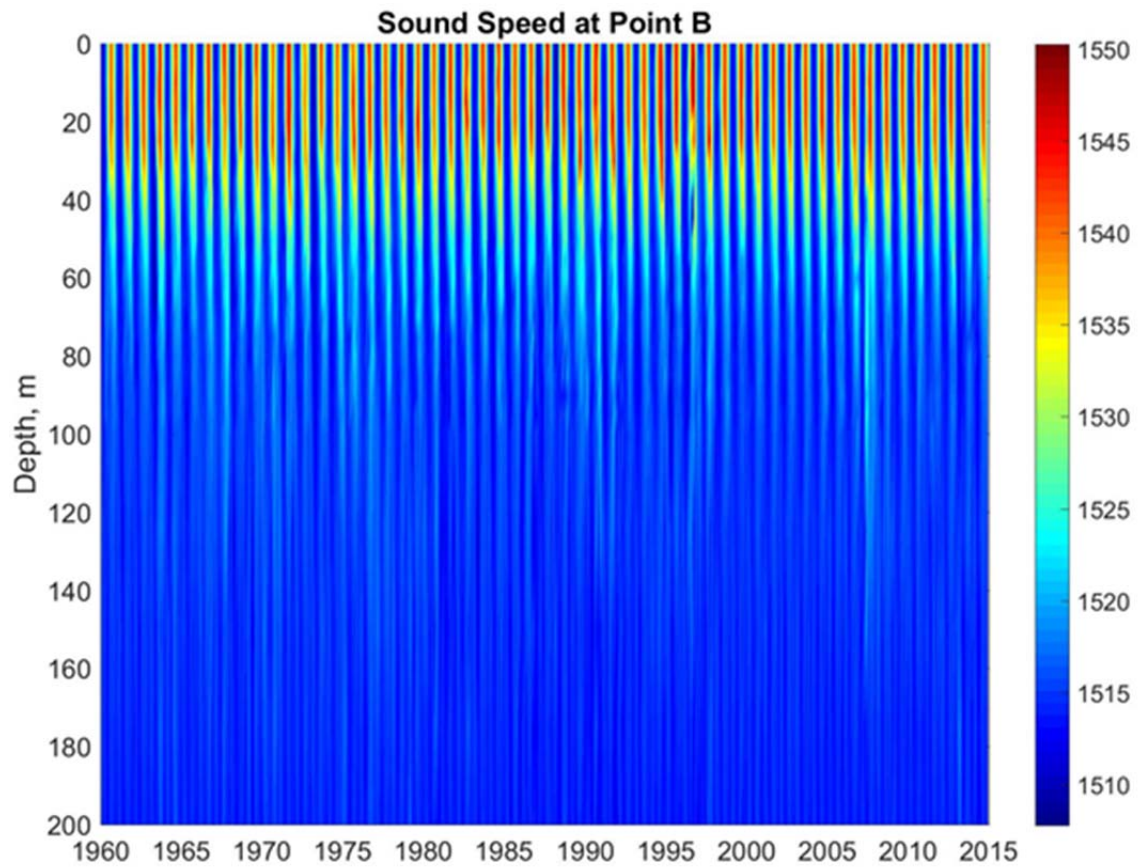
Figure 58.   Temporal Variability of SMG-WOD Sound Speed at Point B

The Point B (Figure 58) show some higher variations in temperature and salinity in specific years. Higher sound speed penetrated to a deeper layer between 2007 and 2008. Sound speed reached its maximum at the surface between 1995 and 1998.
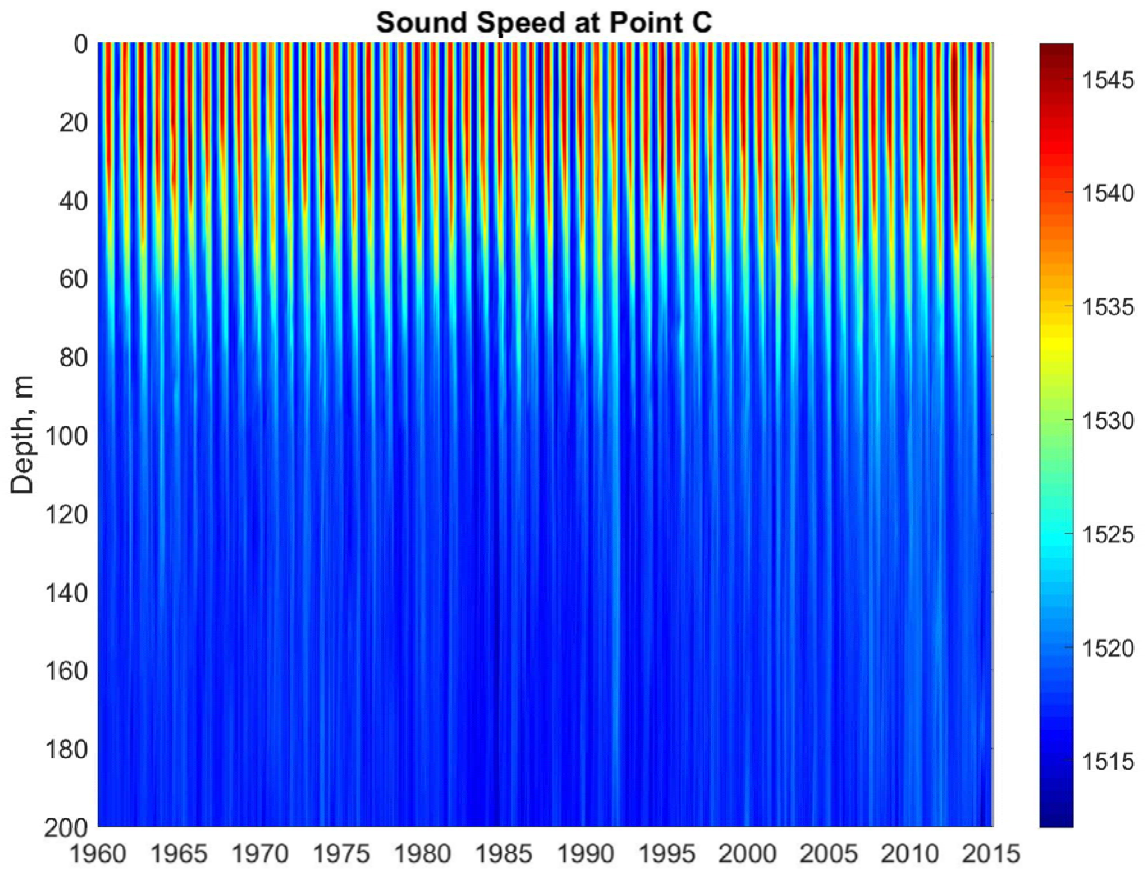
Figure 59.   Temporal Variability of SMG-WOD Sound Speed at Point C

At point C (Figure 59) sound speed shows decadal oscillations at the surface. There were higher variations below 80 meters. After 2005, we found higher sound speed at this depth. Also, we found higher sound speed at the same depth in 1992. The sound speed also increased at the surface between 2000 and 2014. The sound speed reached its minimum value between 1980 and 1985.
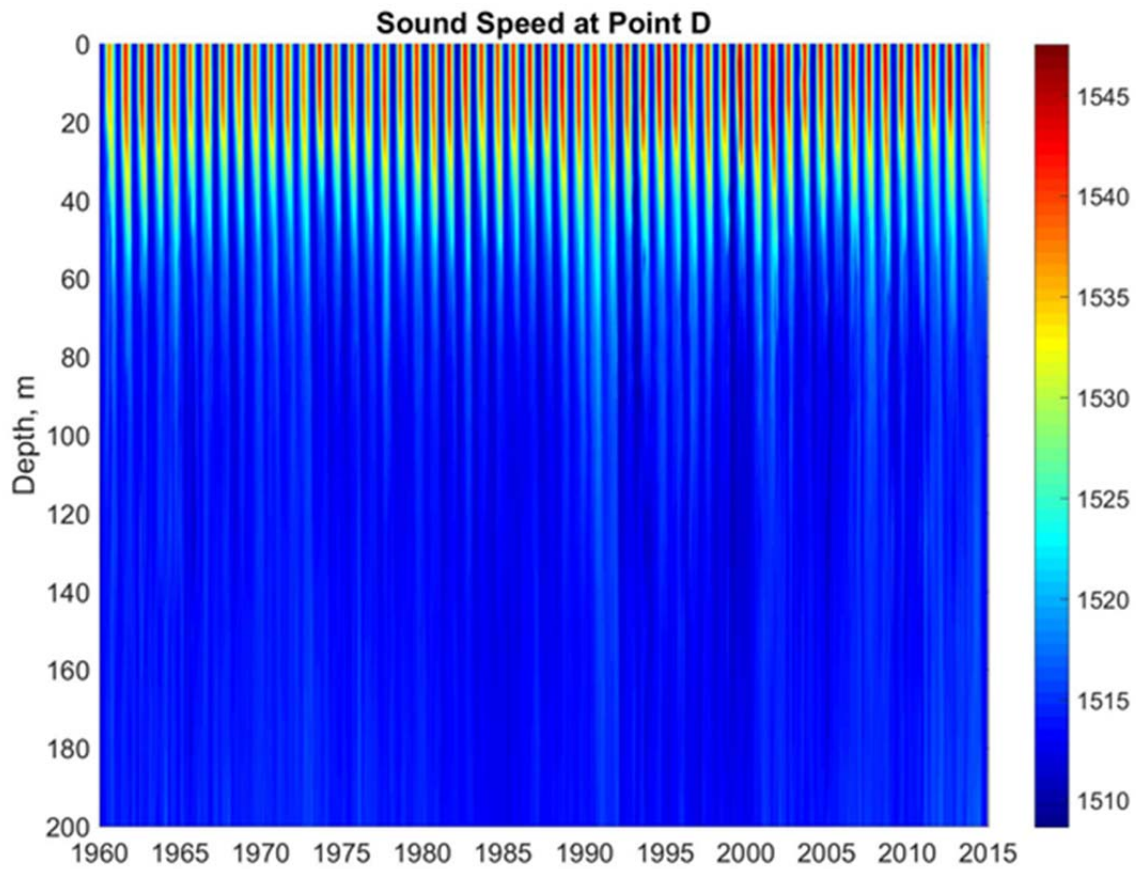
Figure 60.   Temporal Variability of SMG-WOD Sound Speed at Point D

At point D (Figure 60) the sound speed decreased between 1980 and 2000, with an exception of 1990 and 1992. There are very low sound speed values at deeper layers during these years. From 2000 to 2014, the sound speed increased at all depths, especially between 60 and 200 meters.
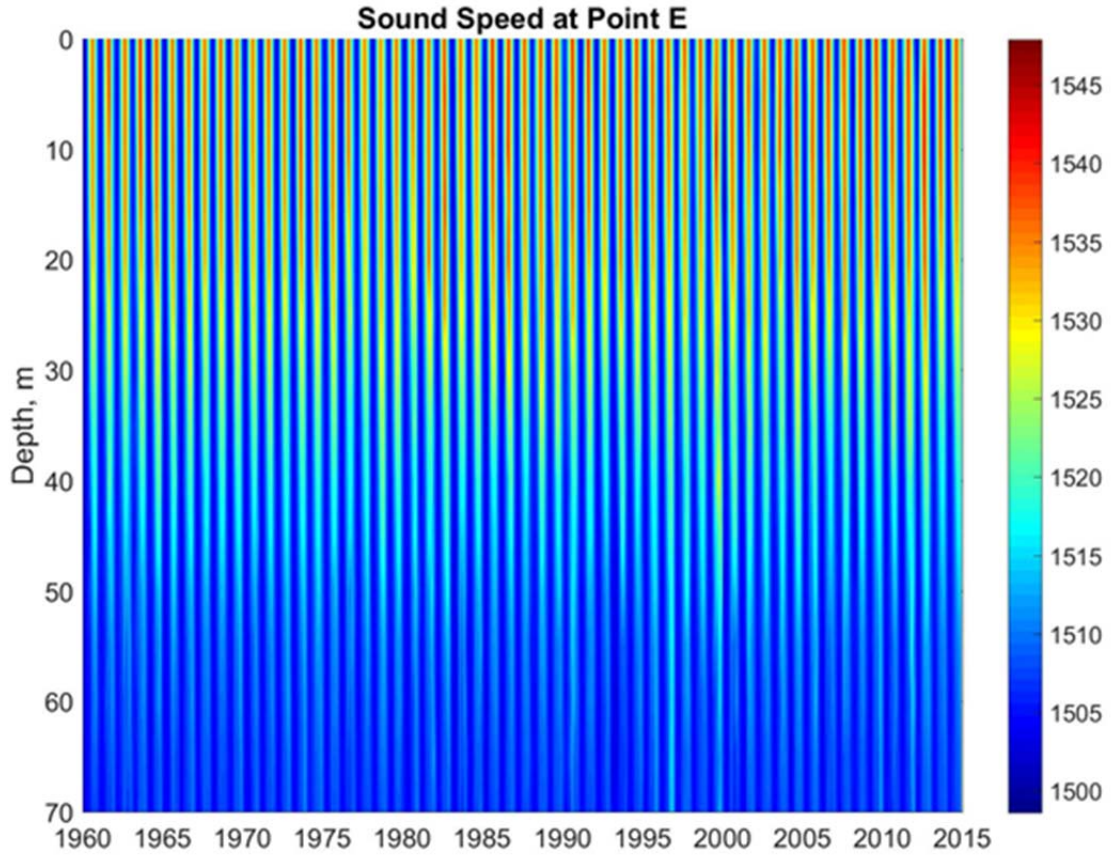
Figure 61.   Temporal Variability of SMG-WOD Sound Speed at Point E

At point E (Figure 61) the sound speed between 1960 and 1990 is lower than during later decades. It starts to increase slightly after 1990 and reaches its maximum between 2010 and 2015.

B.   EOF ANALYSIS

Empirical orthogonal functions (EOF) analysis was conducted to identify the inter-annual variability of the sound speed profiles relative to the multiyear averaged profiles, $\hat{c}(z_i, \tilde{t}_p)$, from the SMG-WOD data between 1960 to 2014 are expanded into EOFs,

$$\hat{c}(z_i, \tilde{t}_p) = \sum_j PC_j(\tilde{t}_p) E_j(z_i),$$

where $E_j(z_i)$ is the jth EOF mode with the unit of m/s; and $PC_j(\tilde{t}_p)$ is the jth principal component without unit. Here, j = 1, 2, …, J; J is truncated number of the EOF modes. Table 16 shows variance contained in the four modes at selected locations.

Table 16. Variances of First Four EOF Modes

Point	Mode 1 %Variance	Mode 2 %Variance	Mode 3 %Variance	Mode 4 %Variance	Cumulative Variance
A	34.1	18.9	13.8	6.1	72.9
B	39.9	17.7	9.4	8.3	75.3
C	42.2	18.3	9.6	7.1	77.2
D	43.9	26.3	9.8	4.1	84.1
E	67.2	19.8	5.3	3.8	96.1

Figures 62 to 66 show the eigenvalues and cumulative variance as percentage of total variability from the first to truncated (30st) mode for the five locations (A, B, C, D, E). In particular, at the point A, it needs 10–11 modes to reach 90% of total variance. At a shallower region (point-E), three modes are required to reach 90% of variance. Point D, which is located to the west of Point A and at the same bottom depth as Point C, demands six modes to reach 90% of the total variance. However, this result may change according to the data scarcity and depths in other regions.
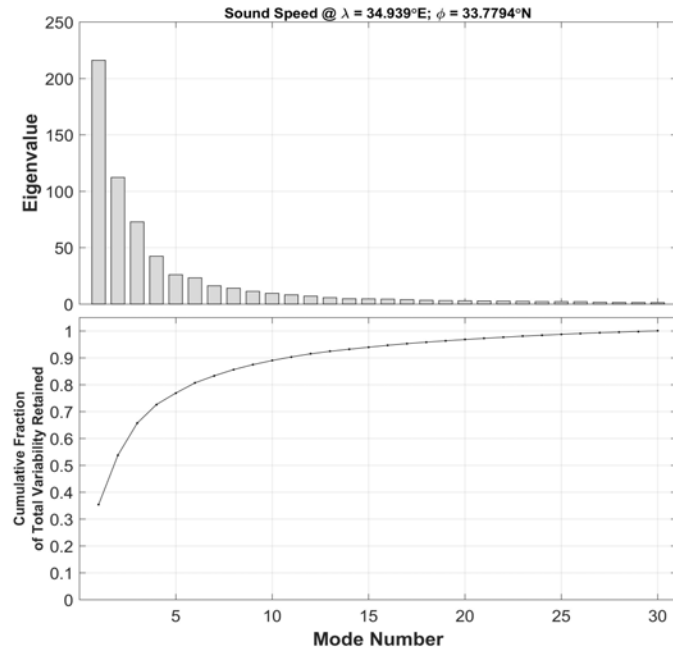
Figure 62.   Point A (Eastern): Eigenvalues and Mode Variance
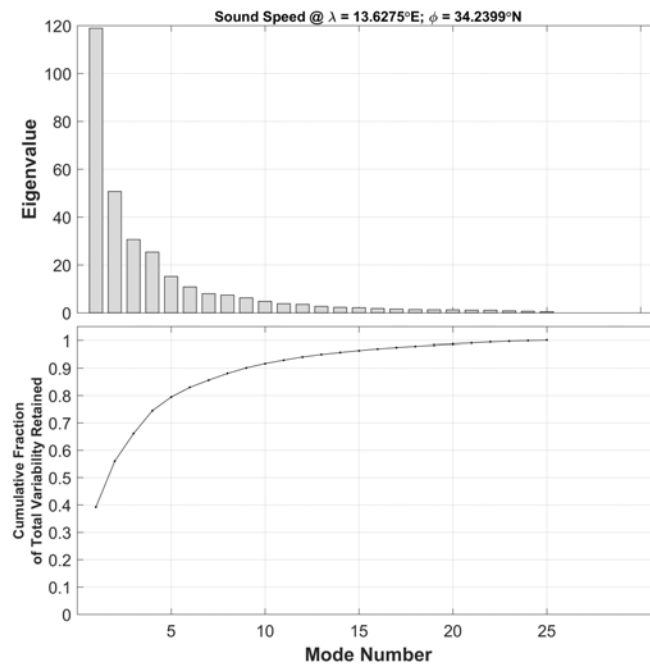
Figure 63.   Point B (Central): Eigenvalues and Mode Variance
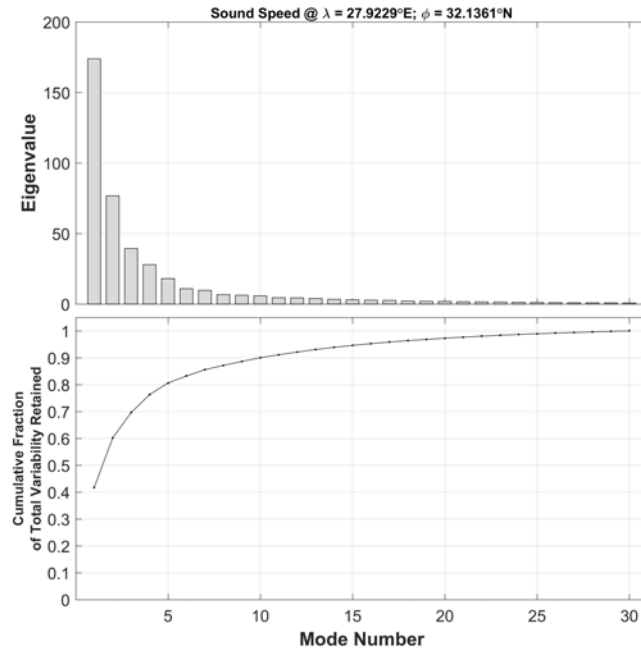
Figure 64.   Point C (Eastern): Eigenvalues and Mode Variance
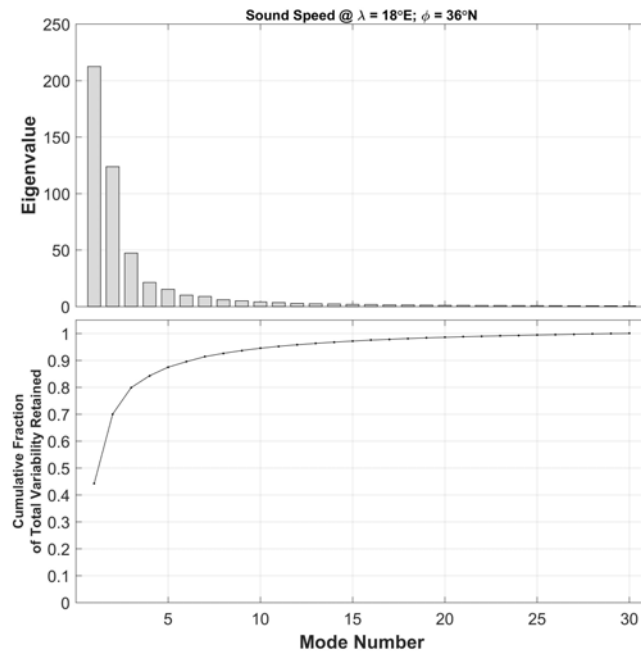
Figure 65.   Point D (Eastern): Eigenvalues and Mode Variance
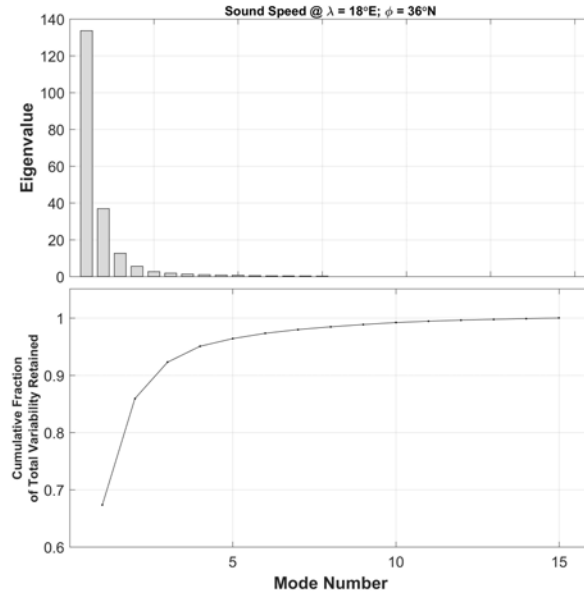
Figure 66.   Point E (Western): Eigenvalues and Mode Variance

Figure 67 and 68 shows four first EOFs and corresponding EOF coefficients (Principal Components) for Point A. Only the first four EOFs are shown because they explain most of the variability in the data. The modes contribute with different sign. Table 17 through 21 demonstrate the results.
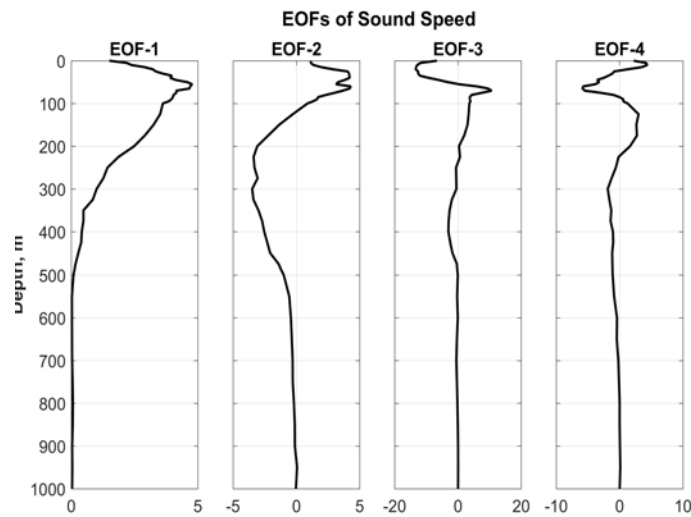
Figure 67.   The First Four EOFs of Point A

97
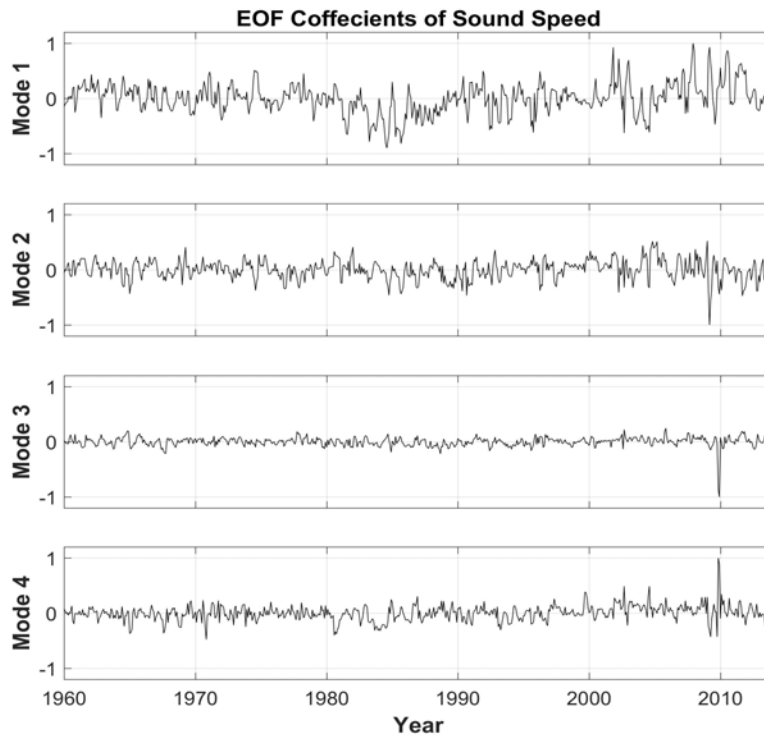
Figure 68.   EOF Coefficients of Sound Speed of Point A

According to the EOF analysis of Point A, we found that sound speed does not change below a depth of 800 meters at that location. We also found that there was a very high variability from 1980 to 1990 and from 2000 to 2014. Therefore, we found that sound speed at the surface was faster between 1960 and 1980; and slower between 1980 and 1990.Those two periods need to be examined in much greater detail to determine what dynamic processes were behind these changes.

Table 17.   EOF Analysis at Point A

Mode Number	EOF Mode		PC		Sound Speed
	Depth	Value	Time	Value	
1	20	Positive	1960-1980 2000-2014	Positive	Increase
	80	Positive			Increase
	300	Positive			Increase
	800	Zero			No change
1	20	Positive	1980-1990	Negative	Decrease
	80	Positive			Decrease
	300	Positive			Decrease
	800	Zero			No change
2	20	Positive	1960-1980 2000-2008	Positive	Increase
	80	Positive			Increase
	300	Negative			Decrease
	800	Zero			No change
2	20	Positive	1980-1990 2008-2010	Negative	Decrease
	80	Positive			Decrease
	300	Negative			Increase
	800	Zero			No change
3	20	Negative	1960-1970	Positive	Decrease
	80	Positive			Increase
	300-500	Negative			Decrease
	800	Zero			No change
3	20	Negative	2009-2010	Negative	Increase
	80	Positive			Decrease
	300-500	Negative			Increase
	800	Zero			No change
4	20	Positive	1960-1970 1980-1985	Negative	Decrease
	80	Negative			Increase
	300-500	Negative			Increase
	800	Zero			No change
4	20	Positive	2009-2010	Positive	Increase
	80	Negative			Decrease
	300-500	Negative			Decrease
	800	Zero			No change

.
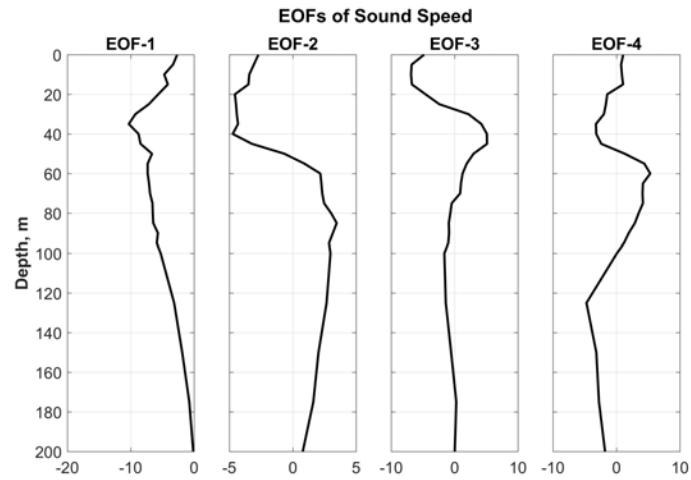
Figure 69.   The First Four EOFs of Point B
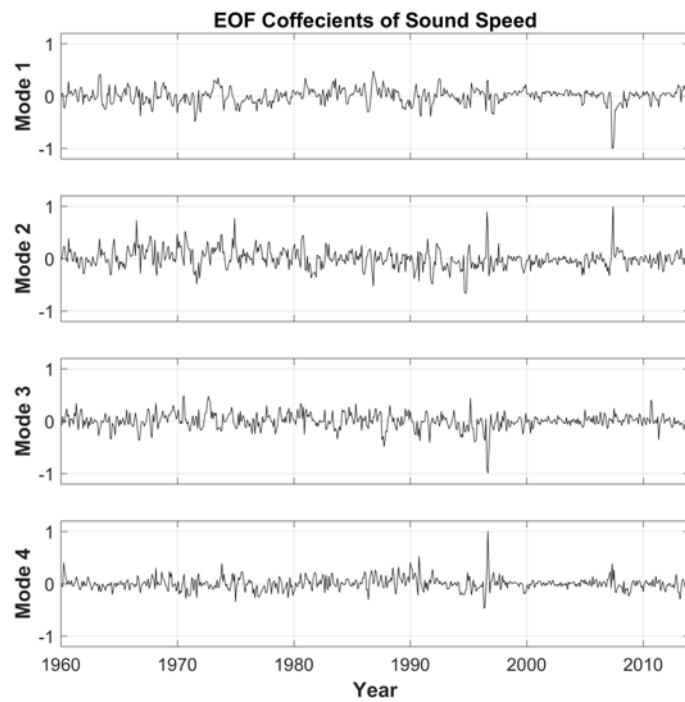
Figure 70.   Coefficients of Sound Speed of Point B

Table 18.　EOF Analysis at Point B

Mode Number	EOF Mode		PC		Sound Speed
	Depth	Value	Time	Value	
1	10	Negative	1960-1970 1980-1990 1997-1998	Positive	Decrease
	60	Negative			Decrease
	80	Negative			Decrease
	140	Negative			Decrease
1	10	Positive	2007-2008 1970-1980	Negative	Decrease
	60	Positive			Decrease
	80	Positive			Decrease
	140	Positive			Decrease
2	10	Negative	1960-1980 1997-1998 2007-2008	Positive	Decrease
	60	Positive			Increase
	80	Positive			Increase
	140	Positive			Increase
3	10	Negative	1970-1980	Positive	Decrease
	60	Positive			Increase
	80	Negative			Decrease
	140	Negative			Decrease
3	10	Negative	1997-1998	Negative	Increase
	60	Positive			Decrease
	80	Negative			Increase
	140	Negative			Increase
4	10	Positive	1960-1970 1980-1992 1997-1998 2007-2008	Positive	Increase
	60	Positive			Increase
	80	Positive			Increase
	140	Negative			Decrease

According to the EOF analysis, Point B has a very high variability for almost all of the period (Figures 69 and 70, and Table 18). However, 2007–2008 and 1997–1998 exhibited the greatest variability. Sound speed throughout all depths decreased during these periods. In addition, sound speed decreased from 1960 to 1980. Those periods need to be examined further to determine what dynamic processes were behind these changes.
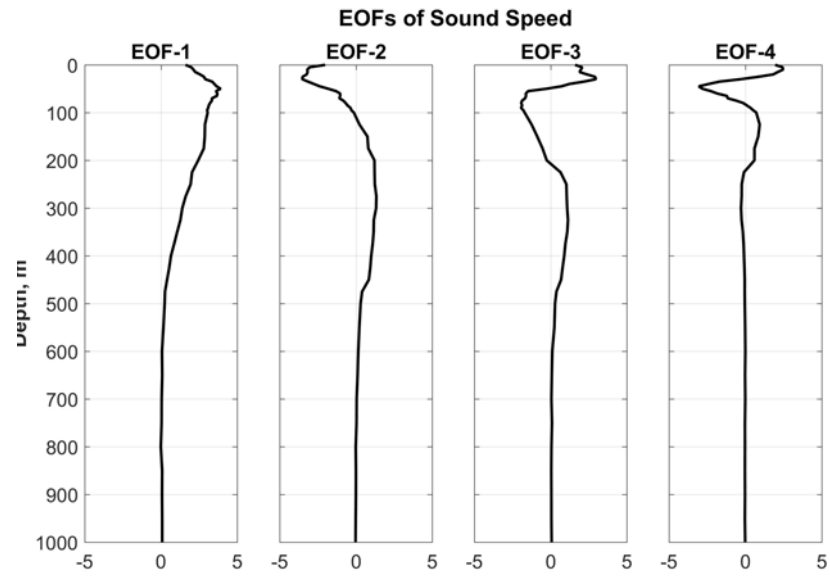
Figure 71.   The First Four EOFs of Point C
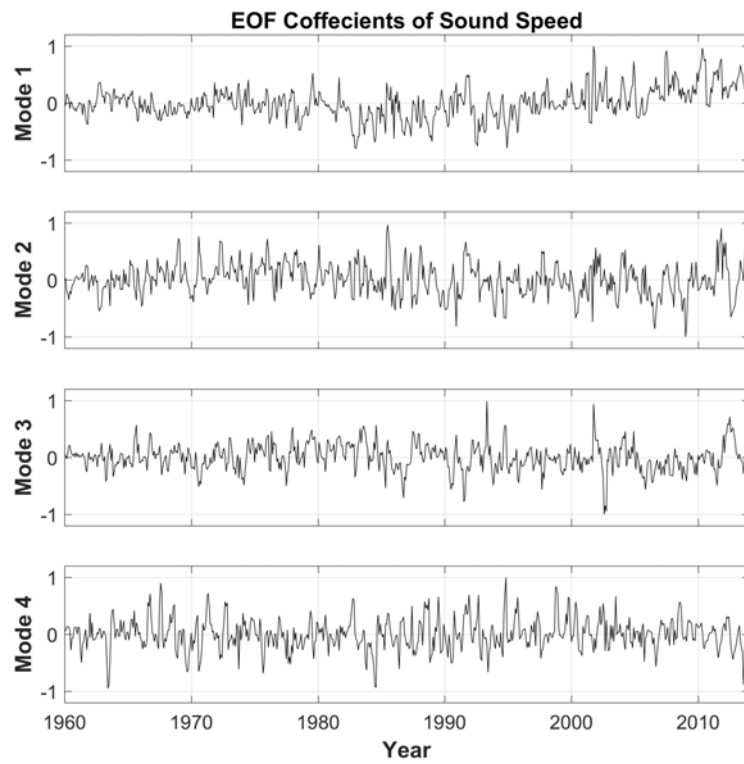
Figure 72.   Coefficients of Sound Speed of Point C

Table 19.   EOF Analysis at Point C

Mode Number	EOF Mode		PC		Sound Speed
	Depth	Value	Time	Value	
1	20	Positive	1980-1995	Negative	Decrease
	80	Positive			Decrease
	300	Positive			Decrease
	600	Zero			No change
1	20	Positive	2000-2014	Positive	Increase
	80	Positive			Increase
	300	Positive			Increase
	600	Zero			No change
2	20	Negative	1968-1989 2010-2014	Positive	Decrease
	80	Negative			Decrease
	300	Positive			Increase
	600	Zero			No change
2	20	Negative	2000-2010	Negative	Increase
	80	Negative			Increase
	300	Positive			Decrease
	600	Zero			No change
3	20	Positive	1965-1985 2010-2014	Positive	Increase
	80	Negative			Decrease
	300	Positive			Increase
	600	Zero			No change
3	20	Positive	2000-2010	Negative	Decrease
	80	Negative			Increase
	300	Positive			Decrease
	600	Zero			No change
4	20	Positive	1982-2005	Positive	Increase
	80	Negative			Decrease
	300	Negative			Decrease
	600	Zero			No change
4	20	Positive	2010-2014	Negative	Decrease
	80	Negative			Increase
	300	Negative			Increase
	600	Zero			No change

We found there was a very high variability from 1980 to 1995 and from 2000 to 2014 at the point C location ((Figures 71 and 72, and Table 19). From 1980 to 1995, the sound speed in the upper and intermediate layers decreased dramatically; conversely, the

upper and intermediate layers increased from 2000 to 2014. We found that sound speed does not change below a depth of 600 meters during the entire period.
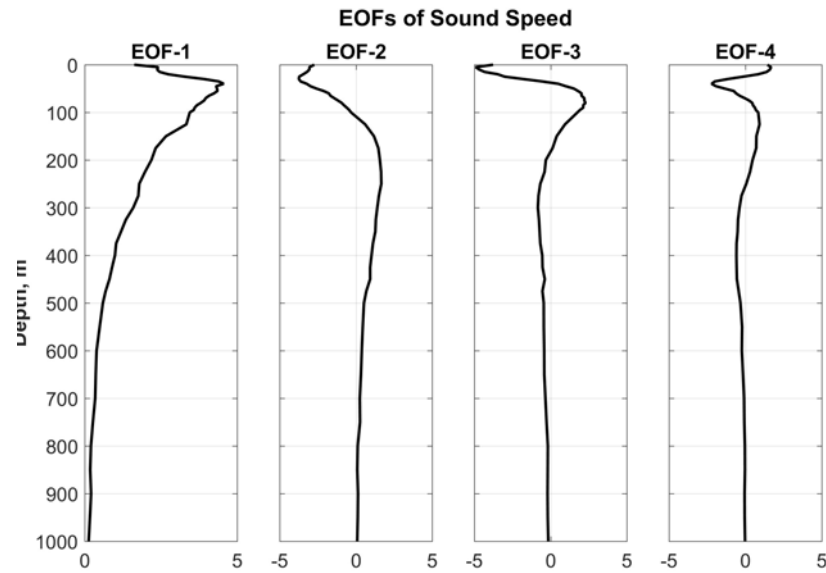
Figure 73.   The First Four EOFs of Point D
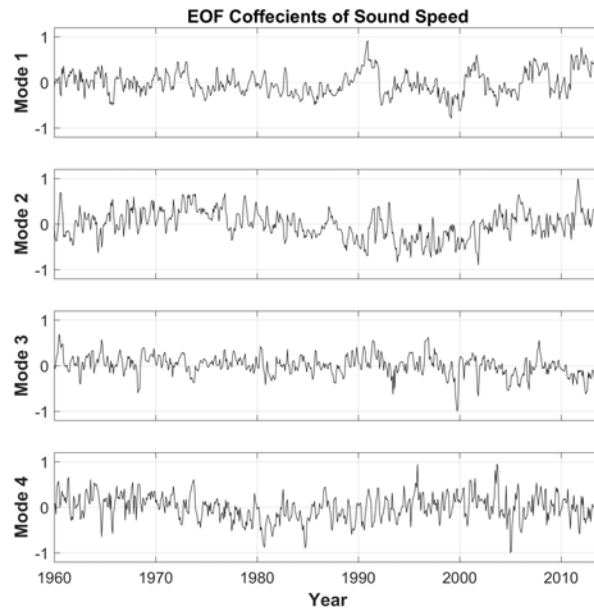
Figure 74.   Coefficients of Sound Speed of Point D

Table 20.   EOF Analysis at Point D

Mode Number	EOF Mode		PC		Sound Speed
	Depth	Value	Time	Value	
1	20	Positive	1960-1975 1990-1992 2000-2014	Positive	Increase
	80	Positive			Increase
	300	Positive			Increase
	800	Zero			No change
1	20	Positive	1980-1990 1992-2000	Negative	Decrease
	80	Positive			Decrease
	300	Positive			Decrease
	800	Zero			No change
2	20	Negative	1960-1988 2002-2014	Positive	Decrease
	80	Negative			Decrease
	300	Positive			Increase
	800	Zero			No change
2	20	Negative	1988-2002	Negative	Increase
	80	Negative			Increase
	300	Positive			Decrease
	800	Zero			No change
3	20	Negative	1960-1973 1988-1998	Positive	Decrease
	80	Positive			Increase
	300	Negative			Decrease
	800	Zero			No change
3	20	Negative	1998-2014	Negative	Increase
	80	Positive			Decrease
	300	Negative			Increase
	800	Zero			No change
4	20	Positive	1960-1975 1990-2012	Positive	Increase
	80	Negative			Decrease
	300	Negative			Decrease
	800	Zero			No change
4	20	Positive	1975-1990	Negative	Decrease
	80	Negative			Increase
	300	Negative			Increase
	800	Zero			No change

At Point D (Figures 73 and 74, and Table 20), there was a very high variability from 1990 to 2000 and from 2000 to 2014. The sound speed increased in the upper layers from 1990 to 1992 and from 2000 to 2014. Conversely, it decreased from 1992 to 2000 in

the upper layers. Sound speed did not change below a depth of 800 meters over the entire time period.
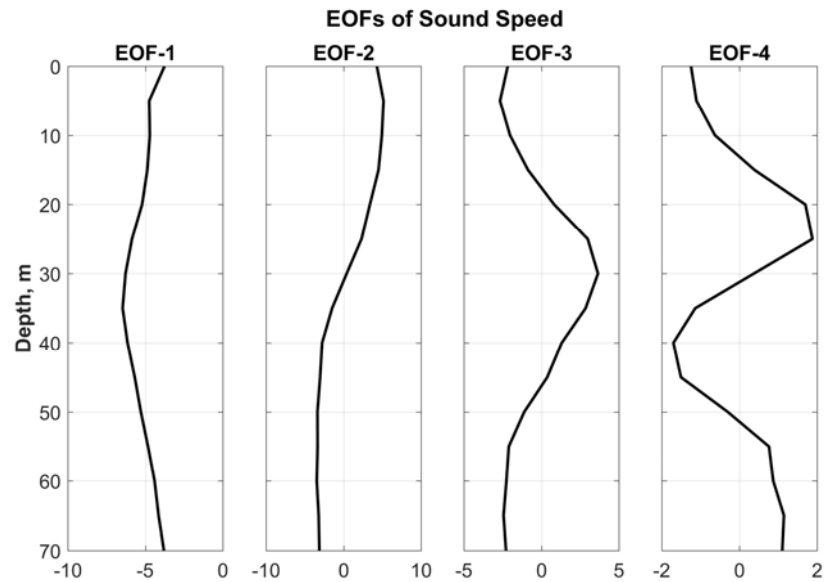
Figure 75.   The First Four EOFs of Point E
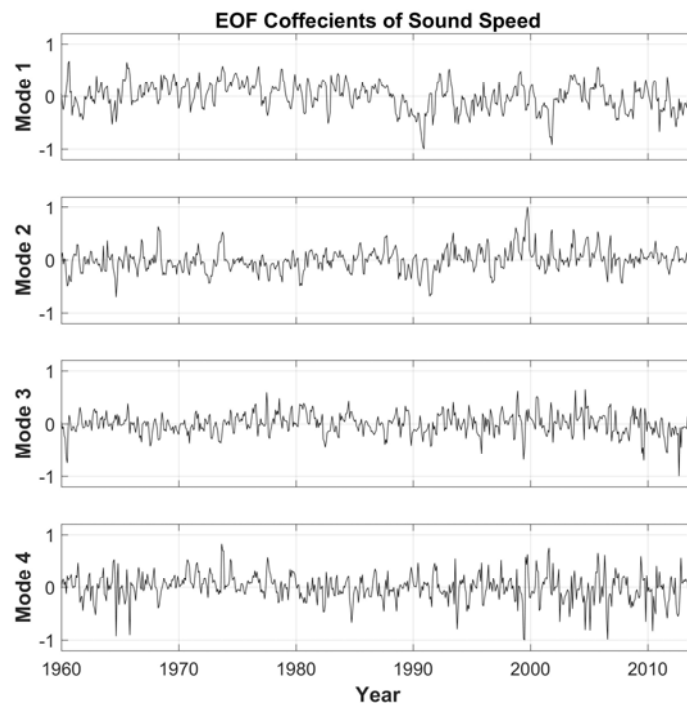
Figure 76.   Coefficients of Sound Speed of Point E

Table 21.   EOF Analysis at Point E

Mode Number	EOF Mode		PC		Sound Speed
	Depth	Value	Time	Value	
1	5	Negative	1960-1970 1970-1980 1980-1990	Positive	Decrease
	25	Negative			Decrease
	40	Negative			Decrease
	70	Negative			Decrease
1	5	Negative	1990-2002 2012-2014	Negative	Increase
	25	Negative			Increase
	40	Negative			Increase
	70	Negative			Increase
2	5	Positive	1992-2014	Positive	Increase
	25	Positive			Increase
	40	Negative			Decrease
	70	Negative			Decrease
2	5	Positive	1988-1992	Negative	Decrease
	25	Positive			Decrease
	40	Negative			Increase
	70	Negative			Increase
3	5	Negative	1973-2009	Positive	Decrease
	25	Positive			Increase
	40	Positive			Increase
	70	Negative			Decrease
3	5	Negative	1960-1972 2010-2014	Negative	Increase
	25	Positive			Decrease
	40	Positive			Decrease
	70	Negative			Increase
4	5	Negative	1970-1980 1990-2012	Positive	Increase
	25	Positive			Decrease
	40	Negative			Decrease
	70	Positive			Increase
4	5	Negative	1960-1970 1980-1990 1999-2014	Negative	Increase
	25	Positive			Decrease
	40	Negative			Increase
	70	Positive			Decrease

We found that the sound speed decreased from 1960 to 1990 at all depths at point E (Figures 75 and 76, and Table 21). Conversely, it increased from 1990 to 2002 and from 2012 to 2014. There was a very high variability at Point E, especially from 1960 to 1970 and from 2000 to 2014.

C.   TRANSMISSION LOSS

BELLHOP shows 2-dimensional ray tracing plots for the given sound speed profiles and bottom sediments. In this section, we plotted TL that BELLHOP creates by months between 1960 and 2014 in order to see TL variations.

Figures 77–81 are time-range plots of TL for a sound receiver located at 50 m. X-axis is time labeled in years and have a 1 month resolution; y-axis is range along the west-east path in meters. TL values are mapped as pseudo-color images using the "jet" colormap. The "warm," yellow-orange part of the colorbar corresponds to lower TL values and higher Received Level. The "cold," blue-green part of the colorbar corresponds to higher TL and lower Received Level.
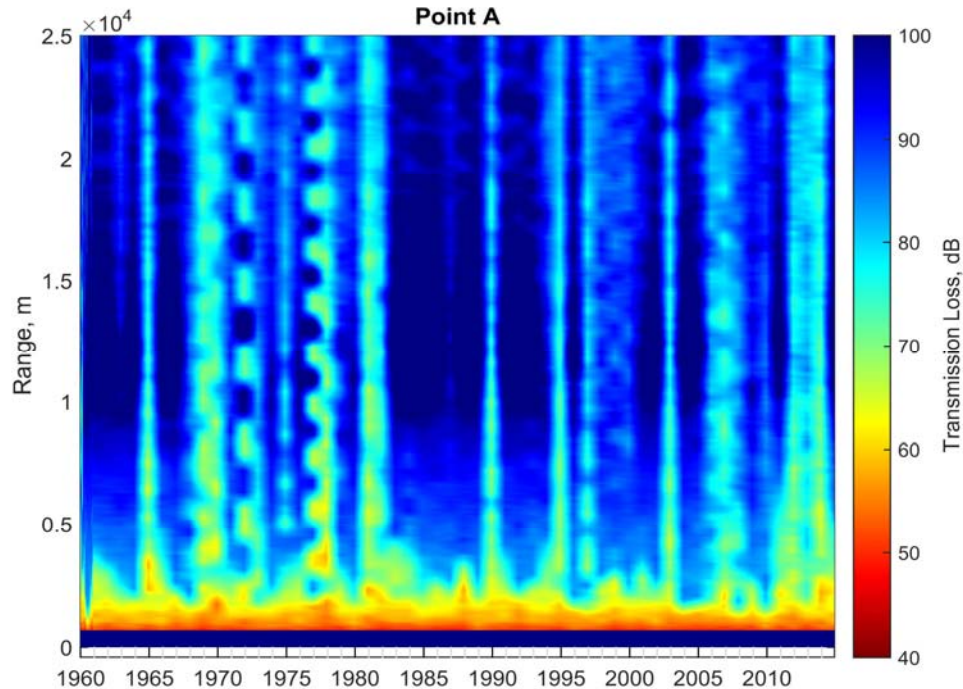
Figure 77.   Time-range TL plot for Point A
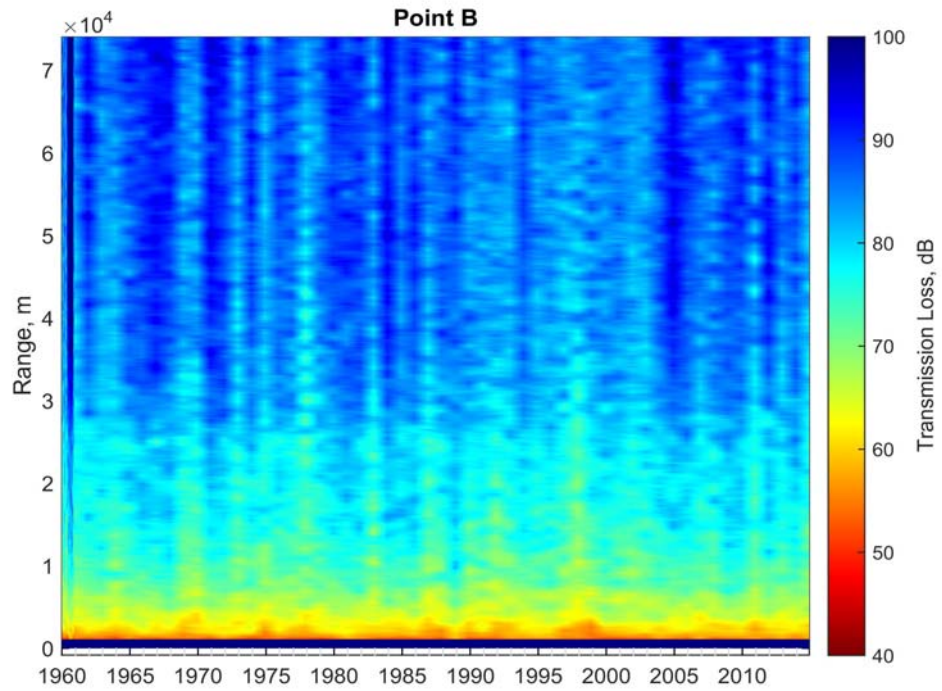
Figure 78. Time-range TL plot for Point B
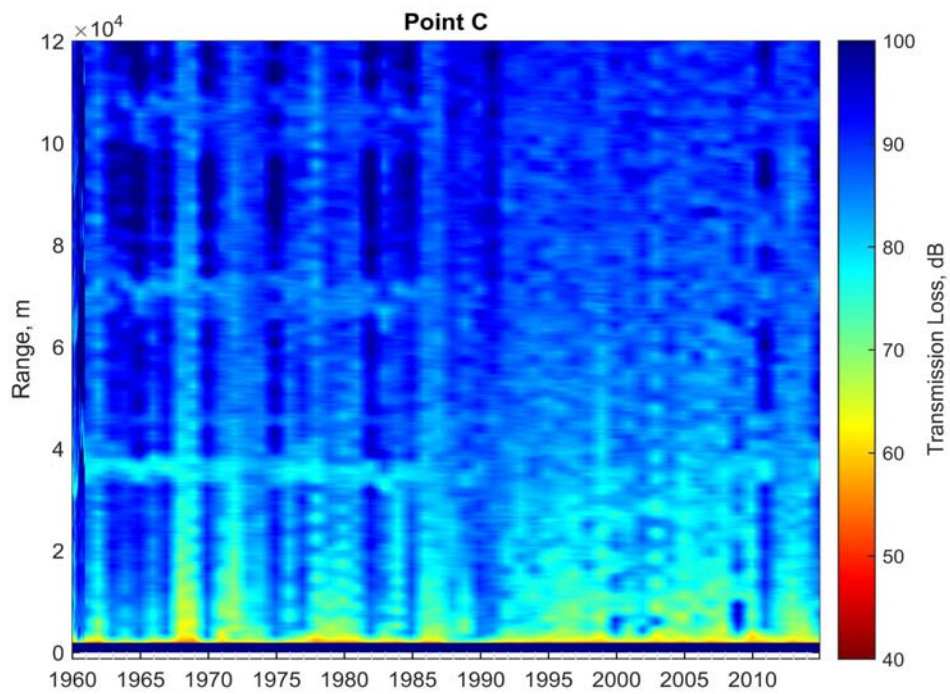
Figure 79. Time-range TL plot for Point C

109
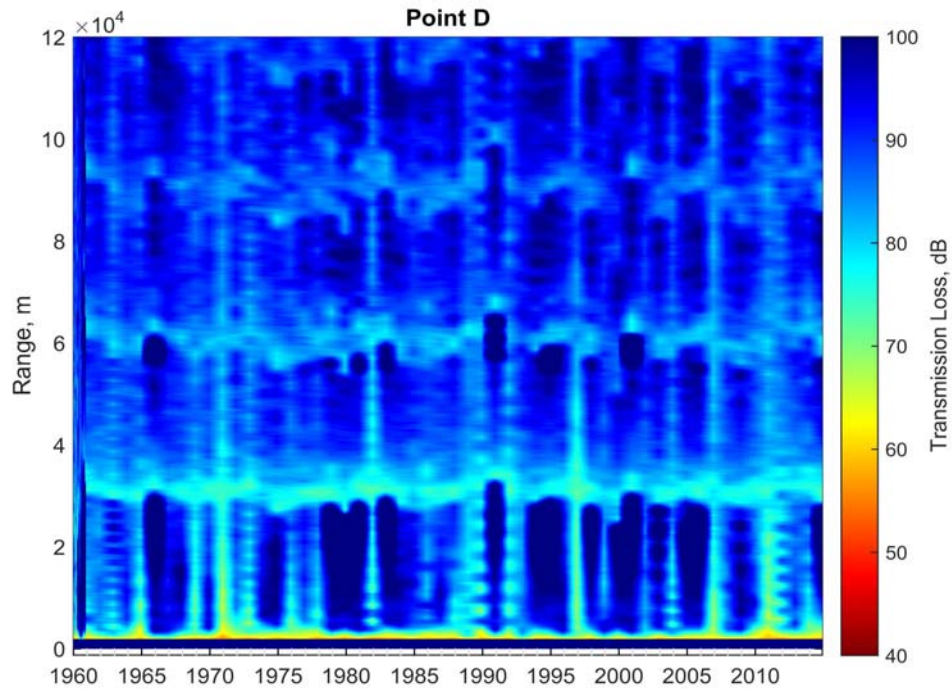
Figure 80.   Time-range TL plot for Point D
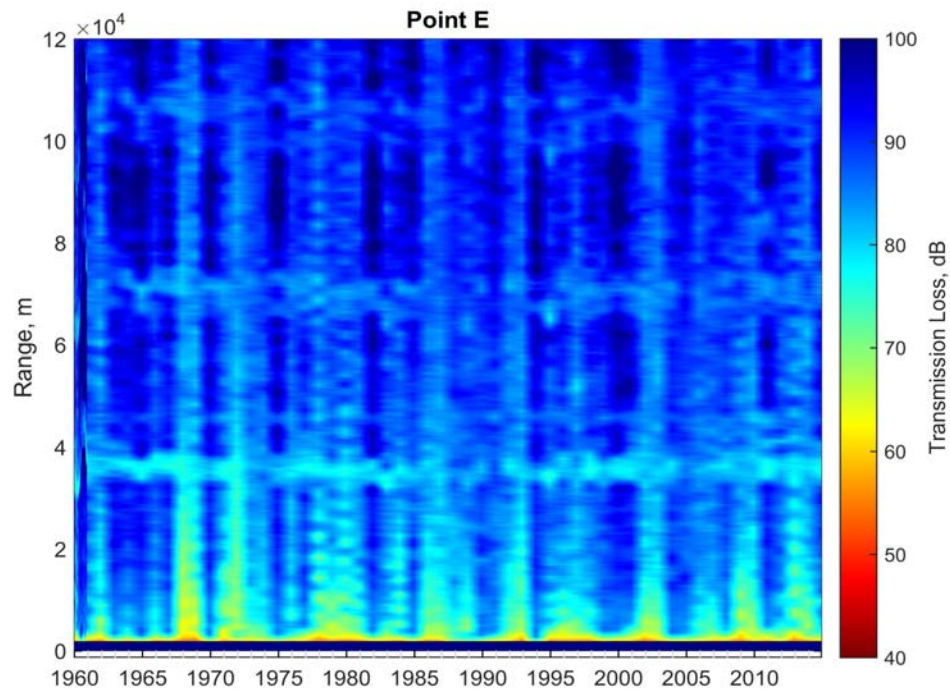
Figure 81.   Time-range TL plot for Point E.

At point A (Figure 77), TL exhibits a high inter-annual variability mostly in magnitude. The highest TL at long ranges occurred between 1982 and 1990. Time periods from 1970 to 1982 and from 2010 to 2014 seemed to have very low TLs overall. Conversely, the time span from 1982 to 1990 at close ranges, 0–5 km, showed a lower TL than from 1970 to 1982.

Point B (Figure 78) represented shallow water in the Central Mediterranean Sea. At this location, the main patterns of acoustic propagation are bottom bounce and surface duct. Figure 79 does not show as much inter-annual variability as Point A. This may be a result of the shallow water and interactions with bottom.

At point C (Figure 79), TL changed quickly between 1960 and 1995. After 1995, the TL exhibited the same values. Thus, we assume that the TL after 1995 shows a different TL distribution than before 1995. In addition, the TL appeared lower between 1995 and 2014. Thus, we assume that detection ranges increased after 1990. Horizontal TL lines represent convergence zone paths. Therefore, we found that a lower TL might occur at longer ranges due to the presence of caustics at the convergence zone.

Three horizontal TL lines in Figure 80 represent the convergence zones at the point D location. They occur at the same range over the all decades, and they do not show high inter-annual variability. Ranges closer than 38 km show high inter-annual variability. There were low TLs from 1960 to 1978, from 1985 to 1992, and from 2007 to 2014. Conversely, high TLs manifested from 1978 to 1985 and from 1992 to 2007. The lowest TL occurred between 2007 and 2014.

Three horizontal TL lines occur at the same range over all decades in Figure 81 for the point E location. They do not show a high variability. Ranges closer than 38 km show inter-annual variability; however, it takes place periodically. Thus, TLs could not be categorized into decades. Nevertheless, the lowest TL occurred between 1967 and 1973.

D. TRANSMISSION LOSS DUE TO SHORT-TERM INTER-ANNUAL VARIABILITY

August and January have been selected to represent the summer and winter seasons. We selected time periods according to years with very different TL distributions to show the effect of short-term inter-annual variability.

a. Point A

In the previous section, we saw that Point A had a lower TL in the period from 1970 to 1982 and from 2010 to 2014. In order to see the TL variations between these time periods, TL was modeled using BELLHOP with sound speed profiles averages over the selected intervals. Results are plotted in Figure 82.
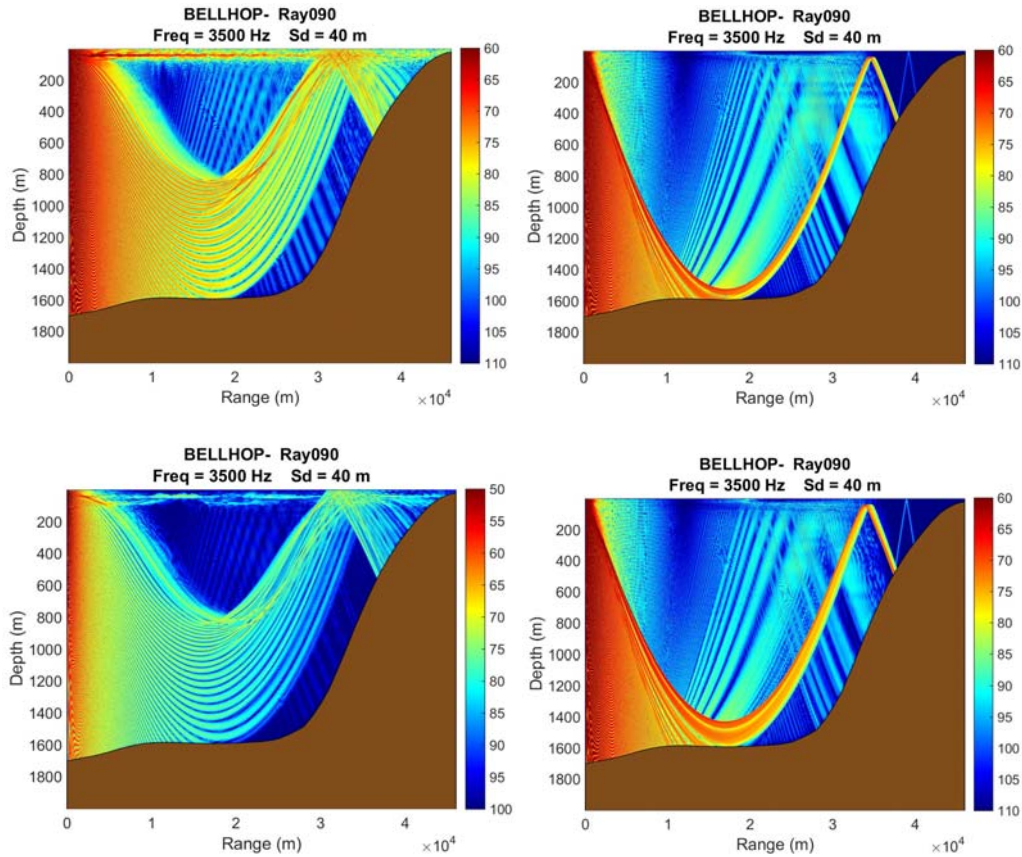
Figure 82. TL for 1970–1979 (upper panels), 1980–1990 (middle panels) and 2000–2014 (lower panels) for Point A in January (left column) and August (right column)
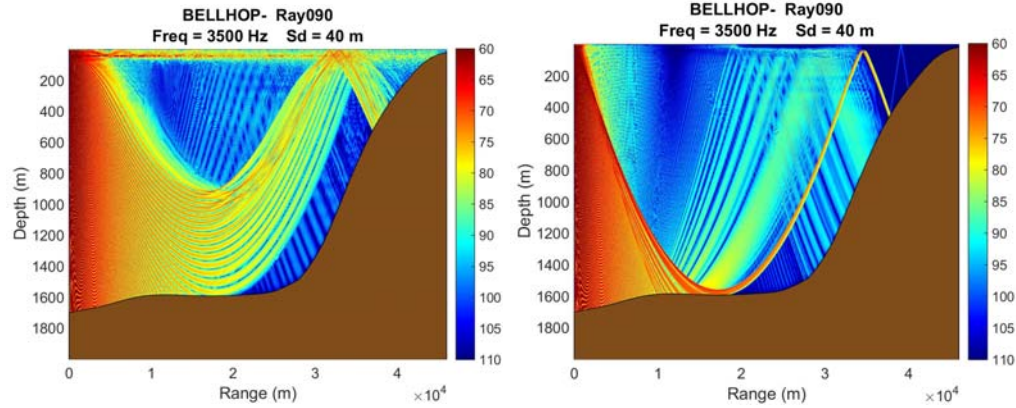
Figure 82 (cont'd)   TL for 1970–1979 (upper panels), 1980–1990 (middle panels)
and 2000–2014 (lower panels) for Point A in January
(left column) and August (right column)

TL variations in January were distributed using different limits. The 1970–1979 time period (upper left) has a 60 dB TL at close distances; however, it has a TL of about 70–85 dB at approximately 3 km and 45 km. The 1980–1990 time period (middle left) shows a TL of 75–85 dB between the same ranges. Specifically, it exhibits a lower TL at the surface duct and in the upper ray limit of the convergence zone. As compared to the 2000–2014 time period (lower left) it has the lower TL for close ranges, but it has a higher TL at long ranges. These results correspond with what we found in the previous section.

TL distributions in August 1970–1979 (upper right) and 1980–1990 (middle right) show the same TL at closer ranges; however, the 1970–1979 time period shows a lower TL at long ranges. The plot for August 2000–2014 (lower right) shows the same TL at closer ranges as in 1980–1990 but a lower TL at long distances.

The researchers found that 1970–1979 and 2000–2014 have higher TLs than 1980–1990 for closer ranges in January; however, they have the same TL in August. For longer ranges, 1980–1990 has the highest TL. Also, we found that January shows significantly more variations than August.

113

b.   *Point B*

From the EOF analysis, we saw that TL does not change very much inter-annually. We found that 2007–2008 and 1997–1998 exhibited the greatest variability. Sound speed throughout all depths decreased during these periods. Figure 83 compares TL for 1997–1998 (upper panels) and 2007–2008 (middle panels) with the SMG-WOD multi-year monthly averages calculated over the total time period of 1960–2014 for January (left columns) and August (right columns).

In January, the surface duct weakens and bottom bounce strengthens both between 1997 and 1998 (upper left) and between 2007 and 2008 (middle left), as compared to the multi-year average (lower left). In August, the bottom bounce weakens and changes into a surface sound channel between 1997 and 1998 (upper right). August 1997–1998 also provides lower TL at longer ranges. In August 2007–2008 (middle right) the bottom bounce does not change much, a higher TL occurred in all ranges, and there was greater propagation at the surface.
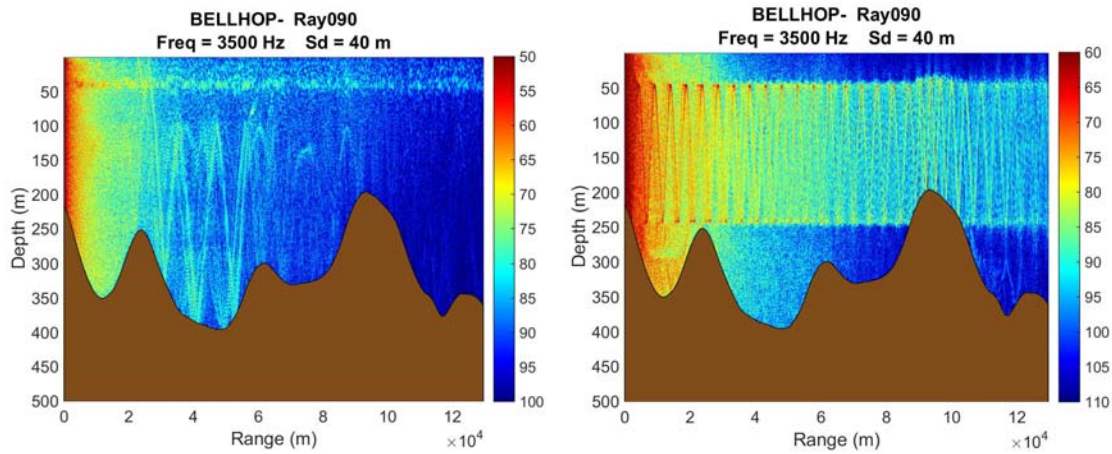
Figure 83.   TL for 1997–1998 (upper panels), 2007–2008 (middle panels)
and multi-year 1960–2014 monthly averages (lower panels) for
Point B in January (left column) and August (right column)
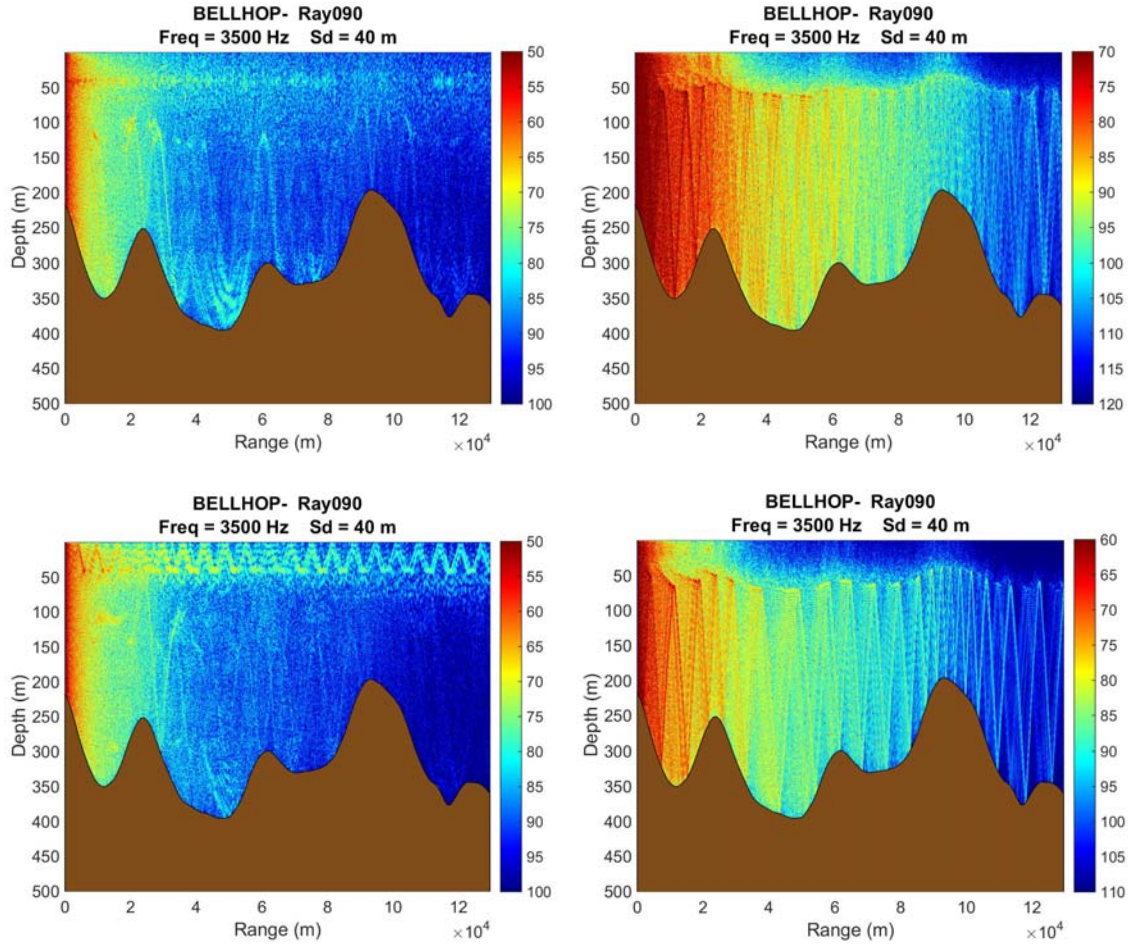
Figure 83 (cont'd).   TL for 1997–1998 (upper panels), 2007–2008 (middle panels) and multi-year 1960–2014 monthly averages (lower panels) for Point B in January (left column) and August (right column)

These results confirmed that there was a high variability from 1997 to 1998 and from 2007 to 2008. Also, we confirmed that January shows a lot more variations than August.

c.   Point C

We found that there is very high variability from 1980 to 1995 and from 2000 to 2014 based on EOF analysis. Also, the TL after 1995 exhibited a different distribution than before 1995. For these reasons, we plotted the TL for 1980–1995 and 2000–2014 (Figure 84) in January (left column) and August (right column).
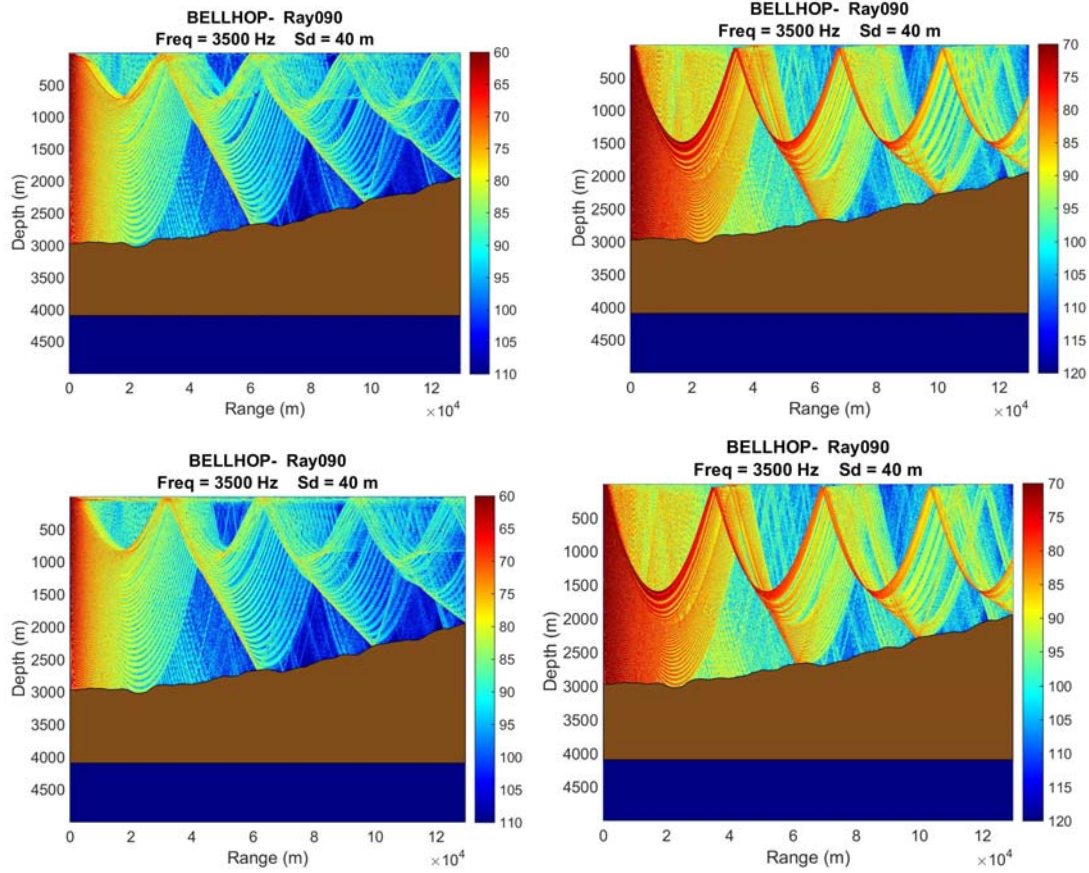
Figure 84.   TL for 1980–1995 (upper panels) and 2000–2014 (lower panels)
for Point C in January (left column) and August (right column)

There are some important variations of TL between these years. The 1980–1995 time period in January (upper left) only shows convergence propagation and the upper limiting ray of the convergence zone that extends to a depth of 800–1000 meters. However, the right figure shows a surface duct and convergence zone propagation together. Also, in 2000–2014 time period in January (lower left), the upper limit of the convergence zone extends to a depth of 900–1100 meters.

In August, both the time periods show convergence zone propagation. However, there is a slight difference between the upper limiting ray of the convergence zone. The upper limiting ray extends to a depth of 1500 meters in 1980–1995 and a depth of 1600 meters in 2000–2014. Also, January showed a lot more variations than August. This

anomaly must have been the result of mixing layer depths and sound-speed profiles because the Mediterranean Sea has very strong, severe winds in winter, but not in summer. These weather patterns may create more inter-annual variations at the surface, which affect sound-speed profiles. Although we saw some inter-annual variations in August, these actually did not affect sound-speed profiles very much. The variations may be a result of very warm water at the surface. Despite the inter-annual variations, August exhibited the highest sound speed at the surface without an upward bend.

d. Point D

From the EOF analysis, the researchers found that the years from 1990 to 2000 and from 2000 to 2014 exhibited high variability. For this reason, we plotted the TL for 1990–2000 and 2000–2014 (Figure 85).

The sound propagation profiles in January were almost the same (Figure 85, left column). Although there was high variability between these years, it did not affect the sound propagation type and TL very much. There was only a slight difference in the shadow zones at the surface. Thus, we found there was a slight inter-annual variability at Point D in January. In August, both the time intervals demonstrate almost the same sound propagation pattern and TL (right column). The 1990–2000 propagation shows a slightly lower TL than in 2000–2014 at long ranges. Therefore, we expected a slight inter-annual variability at Point D in August.
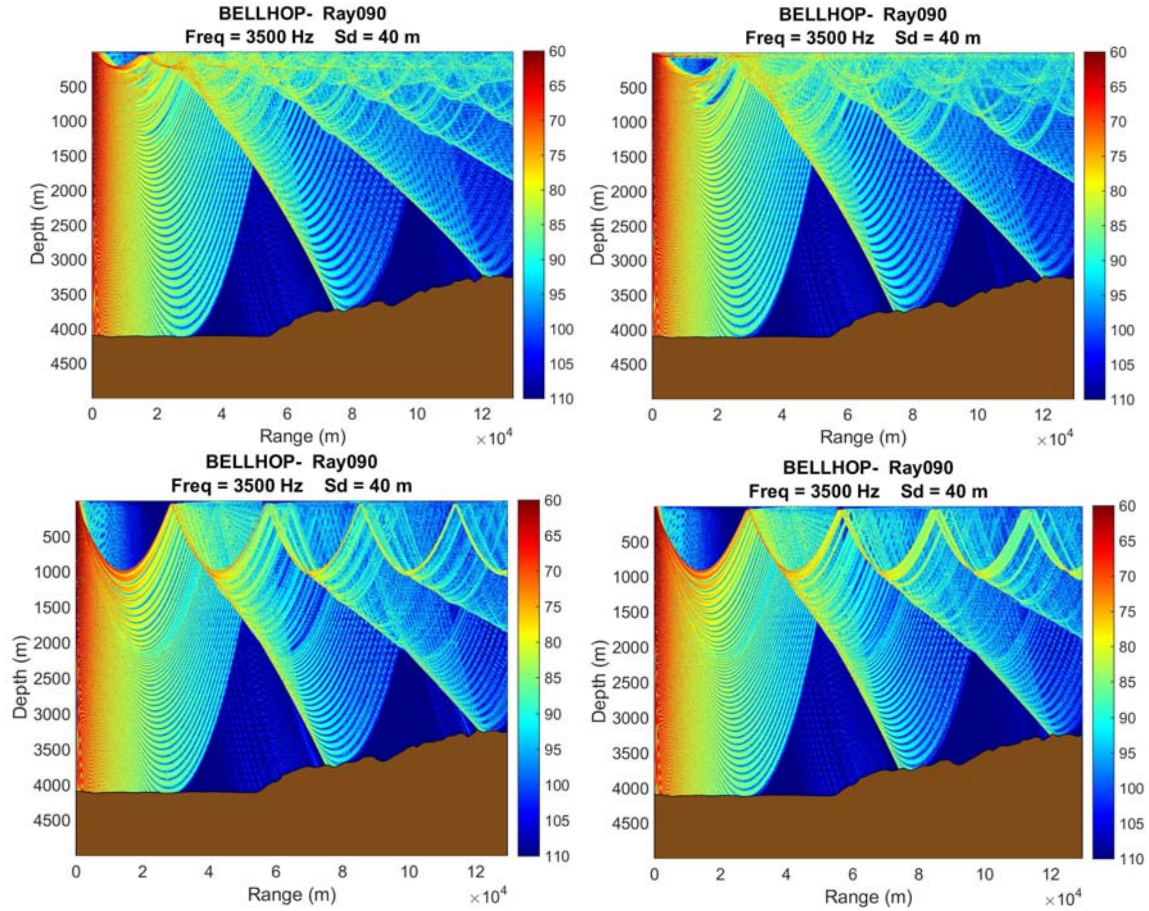
Figure 85.   TL for 1990–2000 (upper panels) and 2000–2014 (lower panels)
for Point D in January (left column) and August (right column)

e.   Point E

From EOF analysis, we found that Point E demonstrated very high variability from 1960 to 1980 and from 2000 to 2014. We also found that it showed a lower TL between 1967 and 1973 from TL analysis. In order to see inter-annual variability between these spans, we plotted Figure 86.
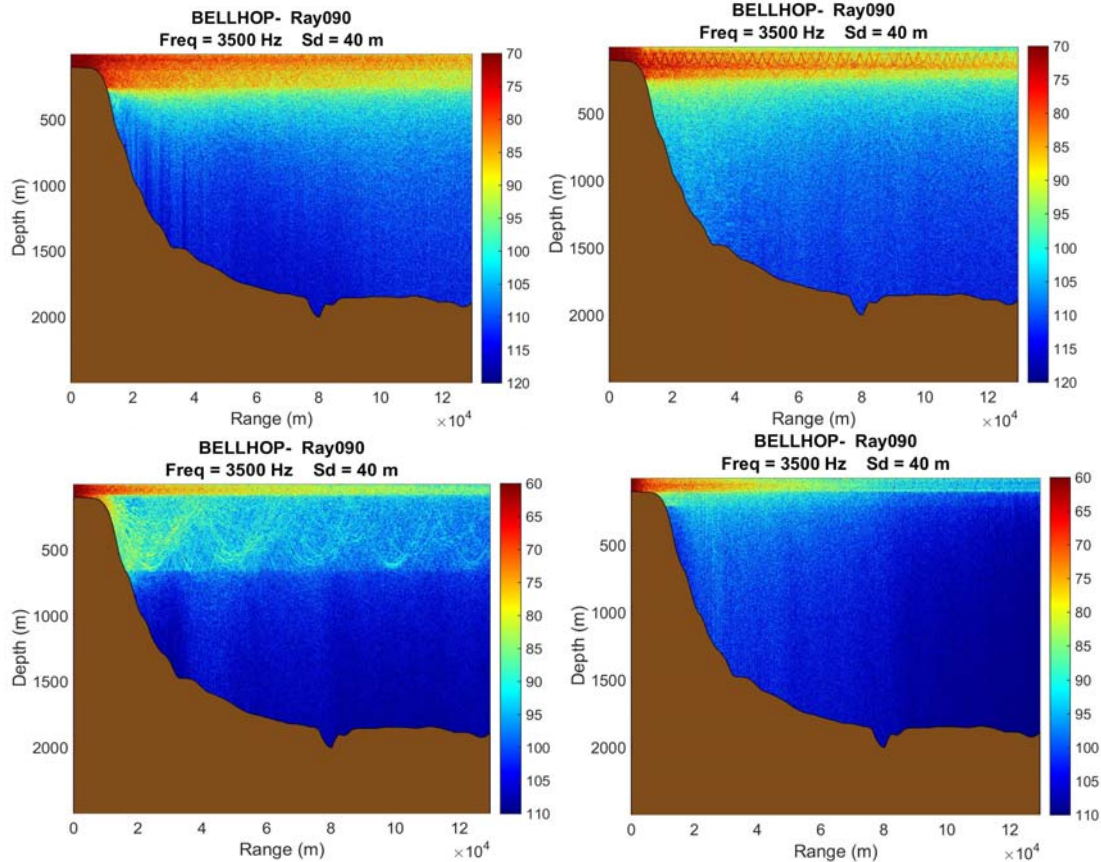
Figure 86.   TL for 1960–1970 (upper panels) and 2000–2014 (lower panels) for Point E in January (left column) and August (right column)

In January, there was high variability between 1960–1970 and 2000–2014 (Figure 86, left column). The earlier interval shows a lower TL at the surface, propagated over a long range and concentrated between the surface and a depth of 300 meters. The later interval demonstrates a sound channel and surface propagation together with a higher TL at long ranges and a lower TL at short ranges. Therefore, we confirmed that Point E showed high variability in January. This variability must have been the result of high-rate sound-speed changes at all depths.

In August, the sound propagations are almost identical in 1960–1970 and 2000–2014 (Figure 86, right column). Both the intervals demonstrate surface propagation; however, the earlier one shows propagation to deeper layers than the later one. There is also a difference in TLs between the figures. The left figure shows a higher TL at short ranges and a lower TL at long ranges. The researchers found that Point E had a higher

variability in January than in August. Moreover, 1960–1970 shows a lower TL at short ranges and a higher TL at long ranges in both months. We also examined why shallow water shows more inter-annual variations than deeper waters. The findings indicate that the mixed layer, especially in winter, may show higher variability than deep layers.

VII. CONCLUSIONS

The primary area of research was inter-annual variability of sound propagation in the Mediterranean Sea using synoptic monthly gridded data and environmental characteristics from the Generalized Digital Environmental Model (GDEM). The latter has been widely used in to model acoustic propagation for Navy needs, while the former is relatively new and has not been applied previously for acoustic modeling in the Mediterranean Sea.

We confirmed that both the climatological and multi-year mean synoptic databases correctly reproduce the high stratification of the Mediterranean Sea and its characteristic water masses. In particular, we found that the Levantine Surface Water (LSW), which forms in August, has the highest spiciness ($9.1\ m^3/kg$) among all water masses in the Mediterranean Sea. The Eastern Mediterranean Sea shows a greater scale of variability of spiciness than the Western Mediterranean Sea in August, but not in January. We also found that spiciness decreases in summer and increases in winter. Both basins showed the same scale of variation in January, but not in August. In addition, there are high spice values around the Crete passage where the Levantine Intermediate Water (LIW) forms in winter in response to strong northerly winds. High salinity and temperature, or high spiciness, is the signature of the LIW.

Five locations have been selected in the Western, Central and Eastern Mediterranean basins to reflect spatial differences in seasonal and inter-annual variability, as well as account for different geoacoustic characteristics and bathymetry. A composite analysis have been applied to sound speed profiles at each locations. This allowed to separate the seasonal and inter-annual variability in the Mediterranean sea.

The temperature profiles at all the locations exhibit strong seasonality associated with surface heat fluxes and variations in the vertical structure of water column. However, this seasonality was strongly modulated by inter-annual and decadal variability. For salinity the inter-annual variability is much stronger than seasonal, most likely associated with inter-annual and decadal variability of freshwater fluxes and water mass formation. For sound speed, variability shows that the upper layer sound speed is

determined by temperature as expected, while the lower level is determined by the pressure and shows neither seasonal nor inter-annual variability. It is however expected that strong inter-annual variability of salinity will affect the inter-annual variability of sound speed. Although temperature and salinity decrease or increase in some decades, overall, the Mediterranean is becoming warmer and saltier from 1960 to 2014, especially from 2000 to 2014.

The SMG-WOD multi-year monthly averages agreed well with and GDEM monthly mean sound-speed profiles. There was a slight difference between them in the upper layers, especially in the thermoclines. There are two possible reasons. First, the vertical resolution is different in these databases. In the upper part of the Mediterranean Sea, GDEM has 78 vertical layers of two-meter vertical resolution; however, SMG-WOD has 57 vertical layers with a 5 m step. Second, GDEM means are calculated for 1945–2014; however, the SMG-WOD covers data between 1960 and 2014. This 15-years' difference can result in biased mean values due to significant inter-annual and decadal variability in the Mediterranean Sea

Empirical orthogonal functions (EOF) analysis was conducted to identify the inter-annual variability of the sound speed profiles. The number of modes necessary to capture 90% of total variance depends on the region. Point E is very shallow and needs only three modes to reach 90 percent. In the Eastern Mediterranean Sea, Point A and Point C demand 10–11 modes to reach a 90 percent variance; however, Point D in the Central Mediterranean Sea reaches 90 percent with only six modes. Point B, which is shallower, reaches 90 percent with 10 modes. Thus, we cannot generalize which region demands more modes. We can only confirm that Points A and C in the Eastern Mediterranean need more modes than Point D at the same depth in the Central Mediterranean.

The maximum sound-speed variability was observed in different decades for different points. Point A (a deep location in the Eastern basin) had great variability from 1980 to 1990 and from 2000 to 2014. The largest variability was observed in 2009–2010. Point B (central shallow location) exhibited the greatest variability in two two-year periods: 2007–2008 and 1997–1998. Point C (another deep location in the Eastern

Mediterranean) had high variability in 1980–1995 and 2000–2014. Point D, which is located in deep water of the central part, shows great variability in 1990–2014. Point E is in very shallow water of the Western Mediterranean Sea, and has great variability in all years. The maximum variations took place between 2000 and 2014.

The inter-annual variability detected by the EOF analysis may result in different shapes of the sound speed profiles in different years for the same seasons. To assess how this variability affects acoustic propagation in the Mediterranean sea, a ray trace model Bellhop was used. The sound source was located at 40 m and has frequency of 3500 Hz. The propagation was modeled in west-east direction up to a maximum range of 70 nautical miles. TL profiles modeled with SMG-WOD multi-year monthly average are similar to those produced by GDEM monthly mean sound speed profiles. Nevertheless, there are some differences. For example, the lowest limiting ray of the convergence zone extends deeper in the SMG-WOD than the GDEM in very deep layers.

TL was calculated for the five selected locations with the acoustic environment modeled by averaging sound speed profiles over different time intervals. These time intervals were chosen based on the results of the EOF analysis. The acoustic modeling was conducted for January and August since it was determined that the maximum variance of sound speed in the Eastern Mediterranean Sea occurs from January to March; however, for the Central and Western Mediterranean Sea, the maximum variance occurs in August.

We analyzed TLs for each decade and found that the TL did not show high inter-annual variability over convergence zone paths. We also found that TL showed higher inter-annual variability at short, up to 5 km ranges, but not for long ranges. January showed more inter-annual changes than August. We detected different types of sound propagation in January, but not in August. A more significant inter-seasonal variability was observed in the upper layer of the water column. We hypothesized that it may be due greater variability of the mixed layer as compared to deep layers, especially in the winter.

The observed inter-annual variability in the acoustic propagation can be important for tactical naval applications. The convergence zones occur in the deep layer of the

Mediterranean Sea in all seasons. Thus, it is always possible to detect submarines from long distances at the surface. Furthermore, a surface duct emerges in winter and propagates sound over long distances. Therefore, we can say that the winter season creates a disadvantageous environment for submarines sailing at periscope depths. Although both the datasets exhibit similar TL profiles, there are some significant differences that can affect naval operations. For example, the SMG-WOD showed an uninterrupted surface duct at Point A in January; however, the GDEM exhibited an interrupted surface duct, which suggests that submarines cannot be detected from the surface at some specific ranges. Additionally, there are few differences in the TL values of the shadow zones. Shadow zones are very important regions for submarines to hide. Submarines can select shadow zones where ranges are poor to avoid detection.

APPENDIX A. BOTTOM SEDIMENTS

Table 22.   Sediment Type Definitions from the Enhanced Database.
Source: NAVO (2006).

Type	Enhanced Categories Description	Enhanced	Standard	Reduced	HFEVA
PT	Sand	102	1125	25	9
PT	Silt	105	1105	52	18
PT	Silty Clay	107	1107	50	7
PT	Clay	108	1108	8	23
PT	Gravel	112	1112	62	3
PT	Sandy Mud	196	1104	25	96
PT	Mud	197	1107	50	7
PC	Sand	202	1225	25	9
PC	Silty Sand	203	1203	24	11
PC	Sandy Silt	204	1204	53	16
PC	Silt	205	1205	52	18
PC	Clayey Silt	206	1206	50	19
PC	Silty Clay	207	1207	50	22
PC	Clay	208	1208	8	23
PC	Sand - Silt - Clay	209	1209	52	17
PC	Marl	211	1208	8	23
PC	Gravel	212	1212	62	3
PC	Gravelly Sand	220	1220	21	7
PC	Coarse Sand	222	1222	22	7
PC	Medium Sand	223	1223	23	9
PC	Sandy Clay	242	1242	25	20
PC	Ooze	310	1208	8	23
PS	Silt	405	1105	52	18
PS	Silty Clay	407	1107	50	7
PS	Clay	408	1108	8	23
PS	Ooze	510	1108	8	23
PS	Mud	511	1105	52	17
P	Clayey Silt	706	1106	50	19
P	Silty Clay	707	1107	50	22
P	Clay	708	1108	8	23
V	Sand	802	1102	23	9
V	Silt	805	1105	52	18
V	Silty Clay	807	1107	50	7
O	NO DATA	888	888	888	888
L	LAND	999	999	999	999
T	Rock	1101	1101	1	2
T	Sand	1102	1102	23	9
T	Silty Sand	1103	1103	25	11
T	Sandy Silt	1104	1104	25	16
T	Silt	1105	1105	52	18

Table 22 (cont'd).   Sediment Type Definitions from the Enhanced Database.
Source: NAVO (2006).

Type	*Enhanced Categories Description*	Enhanced	Standard	Reduced	HFEVA
T	Clayey Silt	1106	1106	50	19
T	Silty Clay	1107	1107	50	22
T	Clay	1108	1108	8	23
T	Sand - Silt - Clay	1109	1109	24	17
T	Gravel	1112	1112	62	3
T	Sandy Gravel	1113	1113	63	4
T	Silty Gravel	1114	1114	63	10
T	Muddy Sandy Gravel	1115	1114	63	6
T	Clayey Gravel	1116	1116	63	10
T	Muddy Gravel	1117	1116	63	10
T	Gravelly Muddy Sand	1118	1120	63	8
T	Gravel - Silty Sand	1119	1113	63	8
T	Gravelly Sand	1120	1120	21	7
T	Very Coarse Sand	1121	1121	21	5
T	Coarse Sand	1122	1122	22	7
T	Medium Sand	1123	1123	23	9
T	Fine Sand	1124	1124	24	11
T	Very Fine Sand	1125	1125	25	13
T	Clayey Sand	1126	1126	25	14
T	Gravel - Shell	1128	1112	62	3
T	Gravelly Silt	1130	1130	21	16
T	Gravelly Silt - Shell	1131	1130	21	16
T	Gravelly Sandy Silt	1132	1130	21	16
T	Gravelly Mud	1133	1130	21	16
T	Gravel - Sand - Mud	1134	1113	63	6
T	Rock - Sand - Mud	1135	1161	61	3
T	Rock - Gravel - Mud	1136	1161	61	3
T	Rock - Gravel - Sand	1137	1161	61	3
T	Rock - Gravel - Sand - Mud	1138	1161	61	3
T	Gravelly Clay	1140	1140	21	21
T	Sand - Clay - Shell	1141	1102	23	9
T	Sandy Clay	1142	1142	25	20
T	Coarse Sand - Shell	1146	1113	63	4
T	Very Fine Silt	1150	1150	50	21
T	Fine Silt	1151	1151	51	19
T	Medium Silt	1152	1152	52	17
T	Coarse Silt	1153	1153	53	15
T	Rough Rock	1154	1101	1	1
T	Mud over Rock	1155	1101	1	2
T	Silty Clay - Shell	1156	1130	21	16
T	Boulders	1160	1160	60	2
T	Cobbles (Stones) - Shell	1161	1161	61	3
T	Pebbles - Shell	1162	1162	62	3
T	Granules	1163	1163	63	3
T	Sand - Silt - Clay - Shell	1164	1112	62	16
T	Gravel - Sand - Shell	1165	1161	61	3
T	Shell	1166	1162	62	3

Table 22 (cont'd). Sediment Type Definitions from the Enhanced Database.
Source: NAVO (2006).

Type	Enhanced Categories Description	Enhanced	Standard	Reduced	HFEVA
C	Muddy Gravel	1217	1216	63	10
C	Gravelly Muddy Sand	1218	1220	63	8
C	Gravel – Silty Sand	1219	1213	63	8
C	Gravelly Sand	1220	1220	21	7
C	Very Coarse Sand	1221	1221	21	5
C	Coarse Sand	1222	1222	22	7
C	Medium Sand	1223	1223	23	9
C	Fine Sand	1224	1224	24	11
C	Very Fine Sand	1225	1225	25	13
C	Clayey Sand	1226	1226	25	14
C	Oolite	1227	1223	23	9
C	Gravel - Shell	1228	1212	62	3
C	Gravelly Silt	1230	1230	21	16
C	Gravelly Silt - Shell	1231	1230	21	16
C	Gravelly Sandy Silt	1232	1230	21	16
C	Gravelly Mud	1233	1230	21	16
C	Gravel - Sand - Mud	1234	1213	63	6
C	Rock - Sand - Mud	1235	1261	61	3
C	Rock - Gravel - Mud	1236	1261	61	3
C	Rock - Gravel - Sand	1237	1261	61	3
C	Rock - Gravel - Sand - Mud	1238	1261	61	3
C	Gravelly Clay	1240	1240	21	21
C	Sand - Clay - Shell	1241	1202	23	9
C	Sandy Clay (Sandy Marl)	1242	1242	25	20
C	Coral Debris - Sand	1243	1212	62	3
C	Coral Debris - Sand - Shell	1244	1212	62	3
C	Coral Debris - Shell	1245	1212	62	3
C	Coarse Sand - Shell	1246	1213	63	4
C	Coral Debris - Sand - Mud	1247	1212	62	6
C	Coral Debris - Mud - Shell	1248	1212	62	6
C	Coral Debris - Mud	1249	1212	62	6
C	Very Fine Silt	1250	1250	50	21
C	Fine Silt	1251	1251	51	19
C	Medium Silt	1252	1252	52	17
C	Coarse Silt	1253	1253	53	15
C	Rough Rock	1254	1201	1	1
C	Mud over Rock	1255	1201	1	2
C	Silty Clay - Shell	1256	1230	21	16
C	Coral Debris - Sand - Mud - Shell	1257	1212	62	3
C	Coral Debris	1258	1212	62	3
C	Coral	1259	1201	1	1
C	Boulders	1260	1260	60	2
C	Cobbles (Stones) - Shell	1261	1261	61	3
C	Pebbles - Shell	1262	1262	62	3
C	Granules	1263	1263	63	3
C	Sand - Silt - Clay - Shell	1264	1212	62	16

Table 22 (cont'd).   Sediment Type Definitions from the Enhanced Database.
Source: NAVO (2006).

Type	*Enhanced Categories Description*	Enhanced	Standard	Reduced	HFEVA
C	Gravel - Sand - Shell	1265	1261	61	3
C	Shell	1266	1262	62	3
C	Rock - Gravel - Sand - Shell	1267	1261	61	3
C	Sand - Shell	1268	1213	63	4
C	Rock - Gravel	1270	1201	1	2
C	Rock - Coral	1271	1201	1	1
C	Rock - Sand	1272	1201	1	2
C	Rock - Mud	1273	1201	1	2
C	Mud - Shell	1274	1214	63	10
C	Gravel - Sand	1275	1213	63	4
C	Gravel - Mud	1276	1214	63	10
C	Clayey Sand - Shell	1277	1220	21	7
C	Soft Mud	1278	1206	50	21
C	Hard Mud	1279	1206	50	19
C	Silty Sand - Shell	1281	1221	21	5
C	Gravelly Sand - Shell	1282	1213	63	4
C	Medium Sand - Shell	1283	1220	21	5
C	Fine Sand - Shell	1284	1220	21	7
C	Sandy Gravel - Shell	1285	1213	63	4
C	Clayey Silt - Shell	1286	1230	21	16
C	Silt - Shell	1287	1230	21	16
C	Silty Gravel - Shell	1288	1214	63	10
C	Sandy Silt - Shell	1289	1213	21	8
C	Muddy Tidal Flats	1290	1253	53	15
C	Sandy Tidal Flats	1291	1223	23	9
C	Sandy Muddy Tidal Flats	1292	1209	24	17
C	Sand Dune	1293	1202	23	9
C	Mud - Sand	1294	1209	24	17
C	Muddy Sand	1295	1209	24	12
C	Sandy Mud	1296	1204	25	18
C	Mud	1297	1205	52	18
C	Clay - Shell	1298	1240	21	10
C	Stiff Mud	1299	1206	50	19
S	Silt	1405	1105	52	18
S	Clay	1408	1108	8	23
S	Ooze	1510	1108	8	23
S	Mud	1511	1105	52	17
V	Sand	1802	1102	23	9
V	Silt	1805	1105	52	18
V	Gravel	1812	1112	62	3
V	Sandy Gravel	1813	1113	63	4
V	Gravelly Sand	1820	1120	21	7
V	Rough Rock	1854	1101	1	1
V	Boulders	1860	1160	60	2
V	Rock - Gravel	1870	1101	1	2
V	Rock - Sand	1872	1101	1	2
V	Gravel - Sand	1875	1113	63	4

Table 22 (cont'd.).   Sediment Type Definitions from the Enhanced Database.
Source: NAVO (2006).

Type	Enhanced Categories Description	Enhanced	Standard	Reduced	HFEVA
UC	Silt	2205	1205	52	18
UC	Clayey Silt	2206	1206	50	19
UC	Silty Clay	2207	1207	50	22
UC	Clay	2208	1208	8	23
UC	Sand - Silt - Clay	2209	1209	24	17
UC	Marl	2211	1208	8	23
US	Silt	2405	1105	52	18
US	Clay	2408	1108	8	23
UC	Ooze	2210	1208	8	23
U	Silty Sand	2603	1103	25	11
U	Sandy Silt	2604	1104	25	16
U	Silt	2605	1105	52	18
U	Clayey Silt	2606	1106	50	19
U	Silty Clay	2607	1107	50	22
U	Clay	2608	1108	8	23
U	Sand - Silt - Clay	2609	1109	24	17
U	Fine Sand	2624	1124	24	11
U	Gravel - Sand	2675	1113	63	4
U	Gravelly Sand - Shell	2682	1113	63	5
HC	Rock	3201	1201	1	2
HC	Sand	3202	1202	23	9
HC	Silty Sand	3203	1203	25	11
HC	Sandy Silt	3204	1204	25	16
HC	Silt	3205	1205	52	18
HC	Clayey Silt	3206	1206	50	19
HC	Silty Clay	3207	1207	50	22
HC	Clay (Marl)	3208	1208	8	23
HC	Sand - Silt - Clay	3209	1209	24	17
HC	Ooze	3210	1208	8	23
HC	Gravel (Shell Detritus)	3212	1212	62	3
HC	Sandy Gravel	3213	1213	63	4
HC	Silty Gravel	3214	1214	63	10
HC	Muddy Sandy Gravel	3215	1214	63	6
HC	Clayey Gravel	3216	1216	63	10
HC	Muddy Gravel	3217	1216	63	10
HC	Gravelly Muddy Sand	3218	1220	63	8
HC	Gravel - Silty Sand	3219	1213	63	8
HC	Gravelly Sand	3220	1220	21	7
HC	Very Coarse Sand	3221	1221	21	5
HC	Coarse Sand	3222	1222	22	7
HC	Medium Sand	3223	1223	23	9
HC	Fine Sand	3224	1224	24	11
HC	Very Fine Sand	3225	1225	25	13
HC	Clayey Sand	3226	1226	25	14
HC	Gravel - Shell	3228	1212	62	3
HC	Gravelly Silt	3230	1230	21	16
HC	Gravelly Silt - Shell	3231	1230	21	16

129

Table 22 (cont'd.).   Sediment Type Definitions from the Enhanced Database.
Source: NAVO (2006).

Type	Enhanced Categories Description	Enhanced	Standard	Reduced	HFEVA
HC	Gravelly Sandy Silt	3232	1230	21	16
HC	Gravelly Mud	3233	1230	21	16
HC	Gravel - Sand - Mud	3234	1213	63	6
HC	Rock - Sand - Mud	3235	1261	61	3
HC	Rock - Gravel - Mud	3236	1261	61	3
HC	Rock - Gravel - Sand	3237	1261	61	3
HC	Rock - Gravel - Sand - Mud	3238	1261	61	3
HC	Gravelly Clay	3240	1240	21	21
HC	Sand - Clay - Shell	3241	1202	23	9
HC	Sandy Clay (Sandy Marl)	3242	1242	25	20
HC	Coral Debris - Sand	3243	1212	62	3
HC	Coral Debris - Sand - Shell	3244	1212	62	3
HC	Coral Debris - Shell	3245	1212	62	3
HC	Coarse Sand - Shell	3246	1213	63	4
HC	Coral Debris - Sand - Mud	3247	1212	62	6
HC	Coral Debris - Mud - Shell	3248	1212	62	6
HC	Coral Debris - Mud	3249	1212	62	6
HC	Very Fine Silt	3250	1250	50	21
HC	Fine Silt	3251	1251	51	19
HC	Medium Silt	3252	1252	52	17
HC	Coarse Silt	3253	1253	53	15
HC	Rough rock	3254	1201	1	1
HC	Mud over Rock	3255	1201	1	2
HC	Silty Clay - Shell	3256	1230	21	16
HC	Coral Debris - Sand - Mud - Shell	3257	1212	62	3
HC	Coral Debris	3258	1212	62	3
HC	Boulders	3260	1260	60	2
HC	Cobbles (Stones) - Shell	3261	1261	61	3
HC	Pebbles - Shell	3262	1262	62	3
HC	Granules	3263	1263	63	3
HC	Sand - Silt - Clay - Shell	3264	1212	62	16
HC	Gravel - Sand - Shell	3265	1261	61	3
HC	Shell	3266	1262	62	3
HC	Rock - Gravel - Sand - Shell	3267	1261	61	3
HC	Sand - Shell	3268	1213	63	4
HC	Rock - Gravel	3270	1201	1	2
HC	Rock - Coral	3271	1201	1	1
HC	Rock - Sand	3272	1201	1	2
HC	Rock - Mud	3273	1201	1	2
HC	Mud - Shell	3274	1214	63	10
HC	Gravel - Sand	3275	1213	63	4
HC	Gravel - Mud	3276	1214	63	10
HC	Clayey Sand - Shell	3277	1220	21	7
HC	Soft Mud	3278	1206	50	21
HC	Hard Mud	3279	1206	50	19
HC	Silty Sand - Shell	3281	1221	21	5

Table 22 (cont'd.).   Sediment Type Definitions from the Enhanced Database.
Source: NAVO (2006).

Type	*Enhanced Categories Description*	Enhanced	Standard	Reduced	HFEVA
HC	Gravelly Sand - Shell	3282	1213	63	4
HC	Medium Sand - Shell	3283	1220	21	5
HC	Fine Sand - Shell	3284	1220	21	7
HC	Sandy Gravel - Shell	3285	1213	63	4
HC	Clayey Silt - Shell	3286	1230	21	16
HC	Silt - Shell	3287	1230	21	16
HC	Silty Gravel - Shell	3288	1214	63	10
HC	Sandy Silt - Shell	3289	1213	21	8
HC	Sand - Mud	3294	1209	24	17
HC	Muddy Sand	3295	1209	24	12
HC	Sandy Mud	3296	1204	25	18
HC	Mud	3297	1205	52	18
HC	Clay - Shell	3298	1240	21	10
HC	Stiff Mud	3299	1206	50	19
HT	Rock	3301	1101	1	2
HT	Sand	3302	1102	23	9
HT	Silty Sand	3303	1103	25	11
HT	Sandy Silt	3304	1104	25	16
HT	Silt	3305	1105	52	18
HT	Clayey Silt	3306	1106	50	19
HT	Silty Clay	3307	1107	50	22
HT	Clay	3308	1108	8	23
HT	Sand - Silt - Clay	3309	1109	24	17
HT	Gravel	3312	1112	62	3
HT	Sandy Gravel	3313	1113	63	4
HT	Silty Gravel	3314	1114	63	10
HT	Muddy Sandy Gravel	3315	1114	63	6
HT	Clayey Gravel	3316	1116	63	10
HT	Muddy Gravel	3317	1116	63	10
HT	Gravelly Muddy Sand	3318	1120	63	8
HT	Gravel - Silty Sand	3319	1113	63	8
HT	Gravelly Sand	3320	1120	21	7
HT	Very Coarse Sand	3321	1121	21	5
HT	Coarse Sand	3322	1122	22	7
HT	Medium Sand	3323	1123	23	9
HT	Fine Sand	3324	1124	24	11
HT	Very Fine Sand	3325	1125	25	13
HT	Clayey Sand	3326	1126	25	14
HT	Gravel - Shell	3328	1112	62	3
HT	Gravelly Silt	3330	1130	21	16
HT	Gravelly Silt - Shell	3331	1130	21	16
HT	Gravelly Sandy Silt	3332	1130	21	16
HT	Gravelly Mud	3333	1130	21	16
HT	Gravel - Sand - Mud	3334	1113	63	6
HT	Rock - Sand - Mud	3335	1161	61	3
HT	Rock - Gravel - Mud	3336	1161	61	3
HT	Rock - Gravel - Sand	3337	1161	61	3

Table 22 (cont'd).   Sediment Type Definitions from the Enhanced Database.
Source: NAVO (2006).

Type	Enhanced Categories Description	Enhanced	Standard	Reduced	HFEVA
HT	Rock - Gravel - Sand - Mud	3338	1161	61	3
HT	Gravelly Clay	3340	1140	21	21
HT	Sand - Clay - Shell	3341	1102	23	9
HT	Sandy Clay	3342	1142	25	20
HT	Very Fine Silt	3350	1150	50	21
HT	Fine Silt	3351	1151	51	19
HT	Medium Silt	3352	1152	52	17
HT	Coarse Silt	3353	1153	53	15
HT	Rough rock	3354	1101	1	1
HT	Mud over Rock	3355	1101	1	2
HT	Silty Clay - Shell	3356	1130	21	16
HT	Boulders	3360	1160	60	2
HT	Cobbles (Stones) - Shell	3361	1161	61	3
HT	Pebbles - Shell	3362	1162	62	3
HT	Granules	3363	1163	63	3
HT	Sand - Silt - Clay - Shell	3364	1112	62	16
HT	Gravel - Sand - Shell	3365	1161	61	3
HT	Shell	3366	1162	62	3
HT	Rock - Gravel - Sand - Shell	3367	1161	61	3
HT	Sand - Shell	3368	1113	63	4
HT	Rock - Gravel	3370	1101	1	2
HT	Rock - Coral	3371	1101	1	1
HT	Rock - Sand	3372	1101	1	2
HT	Rock - Mud	3373	1101	1	2
HT	Mud - Shell	3374	1114	63	10
HT	Gravel - Sand	3375	1113	63	4
HT	Mud - Gravel	3376	1114	63	10
HT	Clayey Sand - Shell	3377	1120	21	7
HT	Soft Mud	3378	1106	50	21
HT	Hard Mud	3379	1106	50	19
HT	Silty Sand - Shell	3381	1121	21	5
HT	Gravelly Sand - Shell	3382	1113	63	4
HT	Medium Sand - Shell	3383	1120	21	5
HT	Fine Sand - Shell	3384	1120	21	7
HT	Sandy Gravel - Shell	3385	1113	63	4
HT	Clayey Silt - Shell	3386	1130	21	16
HT	Silt - Shell	3387	1130	21	16
HT	Silty Gravel - Shell	3388	1114	63	10
HT	Sandy Silt - Shell	3389	1113	21	8
HT	Sand - Mud	3394	1109	24	17
HT	Muddy Sand	3395	1109	24	12
HT	Sandy Mud	3396	1104	25	18
HT	Mud	3397	1105	52	18
HT	Stiff Mud	3399	1106	50	19
HV	Clayey Gravel	3816	1116	63	17
HV	Rock - Gravel - Sand - Shell	3867	1161	61	3
HV	Muddy Sand	3895	1109	24	12

Table 22 (cont'd.).   Sediment Type Definitions from the Enhanced Database.
Source: NAVO (2006).

Type	*Enhanced Categories Description*	Enhanced	Standard	Reduced	HFEVA
HV	Sandy Mud	3896	1104	25	18
HV	Mud	3897	1105	52	18
HS	Ooze	3510	1108	8	23
N	Oceanic Rock Outcrops	4000	1101	1	1
N	Continental Rock Outcrops	5000	1101	1	2
N	Hard Bottom	5069	1101	1	3
A	Marsh	6845	1109	24	18
A	Mangrove	6850	1109	24	11
A	Intratidal	6855	1109	24	9
A	Supratidal Zone	6860	6860	21	999
A	Salt Dome	6865	6865	61	3
A	Gypsum	6870	6870	61	3
A	Peat	6875	1102	23	12
A	Rock Outcrop	6880	1101	1	2
A	Rubble	6885	1162	61	1
A	Manmade Features	6890	1101	1	1

A   Anomalous

C   Calcareous

H   Hemipelagic

N   Non-Depositional

L   Land

O   No Data

P   Pelagic

S   Siliceous

T   Terrigenous

U   Turbiditic

V   Volcanic

THIS PAGE INTENTIONALLY LEFT BLANK

APPENDIX B. SPICINESS CALCULATION FUNCTION

The following equation and coefficients for calculating spiciness (Table B1) are from Flament (1986).

$$\pi(\theta,s) = \sum_{i=0}^{5}\sum_{i=0}^{4} b_{ij}\theta^{i}(s-35)^{i}$$

Table B1: Coefficients, b_{ij}, of the polynomial expression for spiciness.

		j				
		0	1	2	3	4
	0	0	7.7442e-1	-5.85e-3	-9.84e-4	-2.06e-4
	1	5.1655e-2	2.034e-3	-2.742e-4	-8.5e-6	1.36e-5
i	2	6.64783e-3	-2.4681e-4	-1.428e-5	3.337e-5	7.894e-6
	3	-5.4023e-5	7.326e-6	7.0036e-6	-3.0412e-6	-1.0853e-6
	4	3.949e-7	-3.029e-8	-3.8209e-7	1.0012e-7	4.7133e-8
	5	-6.36e-10	-1.309e-9	6.048e-9	-1.1409e-9	-6.676e-10

A Matlab version of Flament's algorithm is listed below as SPICE.M:

SPICE.M: Spiciness Calculation Function

```
function Tau = spice(S,Theta)
% SPICE - 'Spiciness', an oceanographic variable for
% characterization of intrusions and water masses.
%
% Use as: Tau = spice(S,Theta)
% Inputs: S    = Salinity (psu)
%          Theta = Potential temperature (°C)
```

```matlab
% Output: Tau  = spiciness
%
% Brian Schlining; 07 Oct 1997
% Algorithm from Flament, 1985.

% Table of Coefficients b(i,j) of polynomial expression
b = [ 0        7.7442e-1 -5.85e-3  -9.84e-4  -2.06e-4;...
      5.1655e-2 2.034e-3 -2.742e-4 -8.5e-6    1.36e-5;...
      6.64783e-3 -2.4681e-4 -1.428e-5 3.337e-5 7.894e-6;...
      -5.4023e-5 7.326e-6 7.0036e-6 -3.0412e-6 -1.0853e-6;...
      3.949e-7  -3.029e-8 -3.8209e-7 1.0012e-7 4.7133e-8;...
      -6.36e-10 -1.309e-9 6.048e-9 -1.1409e-9 -6.676e-10];

% Polynomial calculation of spiciness
Tau = b(1,1).*Theta.^0.*(S-35).^0 + ...
    b(1,2).*Theta.^0.*(S-35).^1 + ...
    b(1,3).*Theta.^0.*(S-35).^2 + ...
    b(1,4).*Theta.^0.*(S-35).^3 + ...
    b(1,5).*Theta.^0.*(S-35).^4 + ...
    b(2,1).*Theta.^1.*(S-35).^0 + ...
    b(2,2).*Theta.^1.*(S-35).^1 + ...
    b(2,3).*Theta.^1.*(S-35).^2 + ...
    b(2,4).*Theta.^1.*(S-35).^3 + ...
    b(2,5).*Theta.^1.*(S-35).^4 + ...
    b(3,1).*Theta.^2.*(S-35).^0 + ...
    b(3,2).*Theta.^2.*(S-35).^1 + ...
    b(3,3).*Theta.^2.*(S-35).^2 + ...
    b(3,4).*Theta.^2.*(S-35).^3 + ...
    b(3,5).*Theta.^2.*(S-35).^4 + ...
    b(4,1).*Theta.^3.*(S-35).^0 + ...
    b(4,2).*Theta.^3.*(S-35).^1 + ...
    b(4,3).*Theta.^3.*(S-35).^2 + ...
    b(4,4).*Theta.^3.*(S-35).^3 + ...
    b(4,5).*Theta.^3.*(S-35).^4 + ...
    b(5,1).*Theta.^4.*(S-35).^0 + ...
    b(5,2).*Theta.^4.*(S-35).^1 + ...
    b(5,3).*Theta.^4.*(S-35).^2 + ...
    b(5,4).*Theta.^4.*(S-35).^3 + ...
    b(5,5).*Theta.^4.*(S-35).^4 + ...
    b(6,1).*Theta.^5.*(S-35).^0 + ...
    b(6,2).*Theta.^5.*(S-35).^1 + ...
    b(6,3).*Theta.^5.*(S-35).^2 + ...
    b(6,4).*Theta.^5.*(S-35).^3 + ...
    b(6,5).*Theta.^5.*(S-35).^4;
```
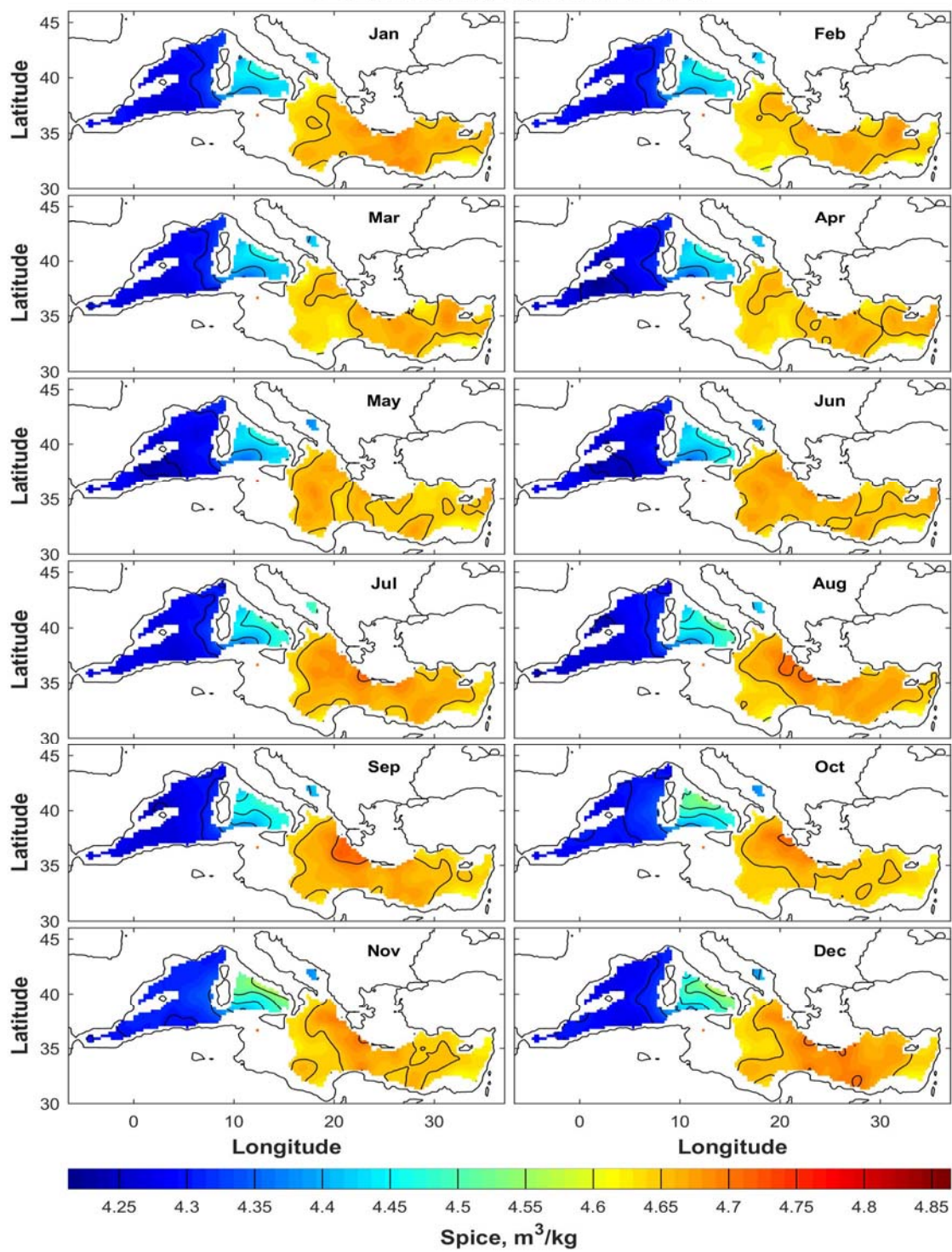
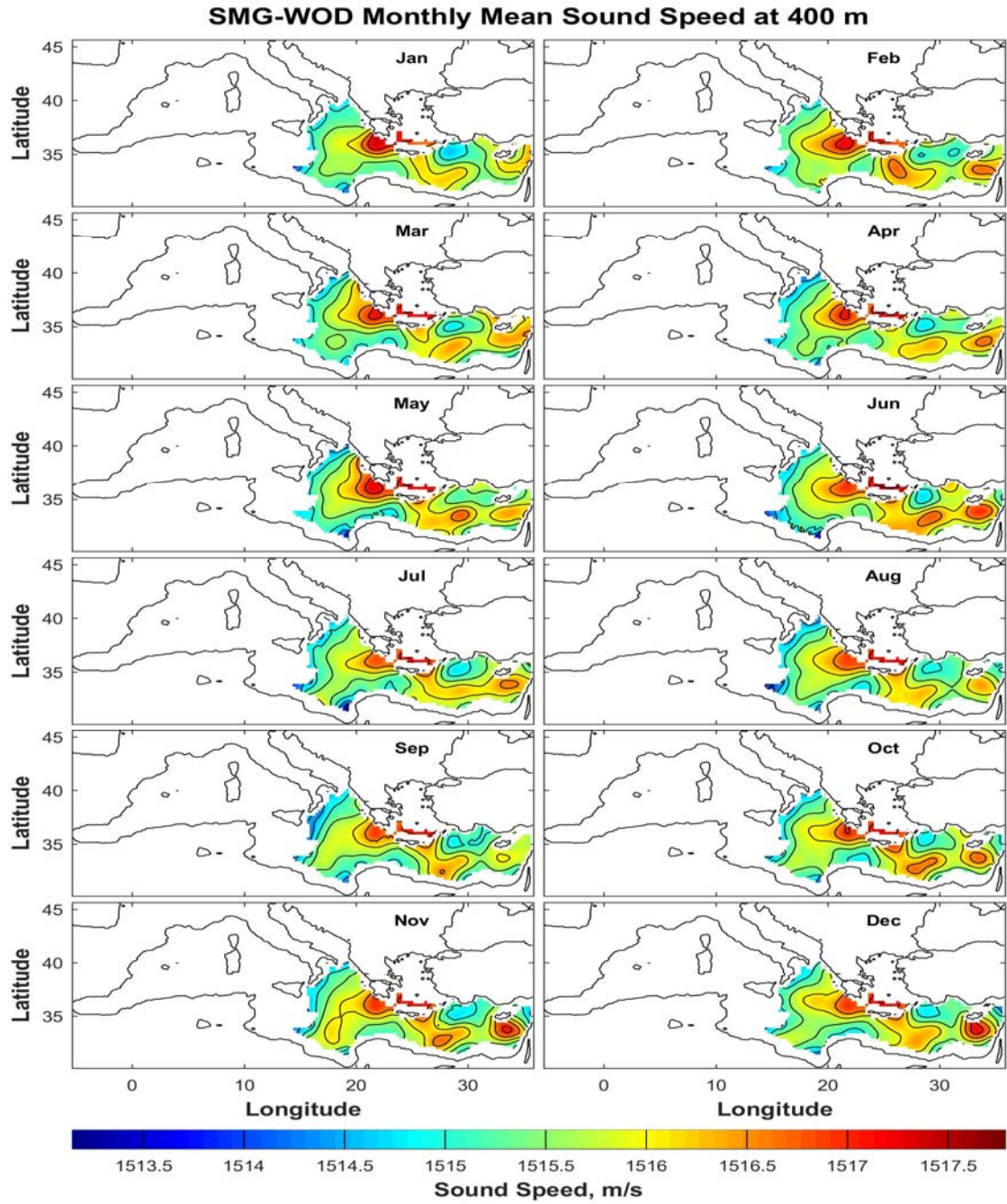# APPENDIX C. ADDITIONAL GDEM MONTHLY SPICE FIGURES

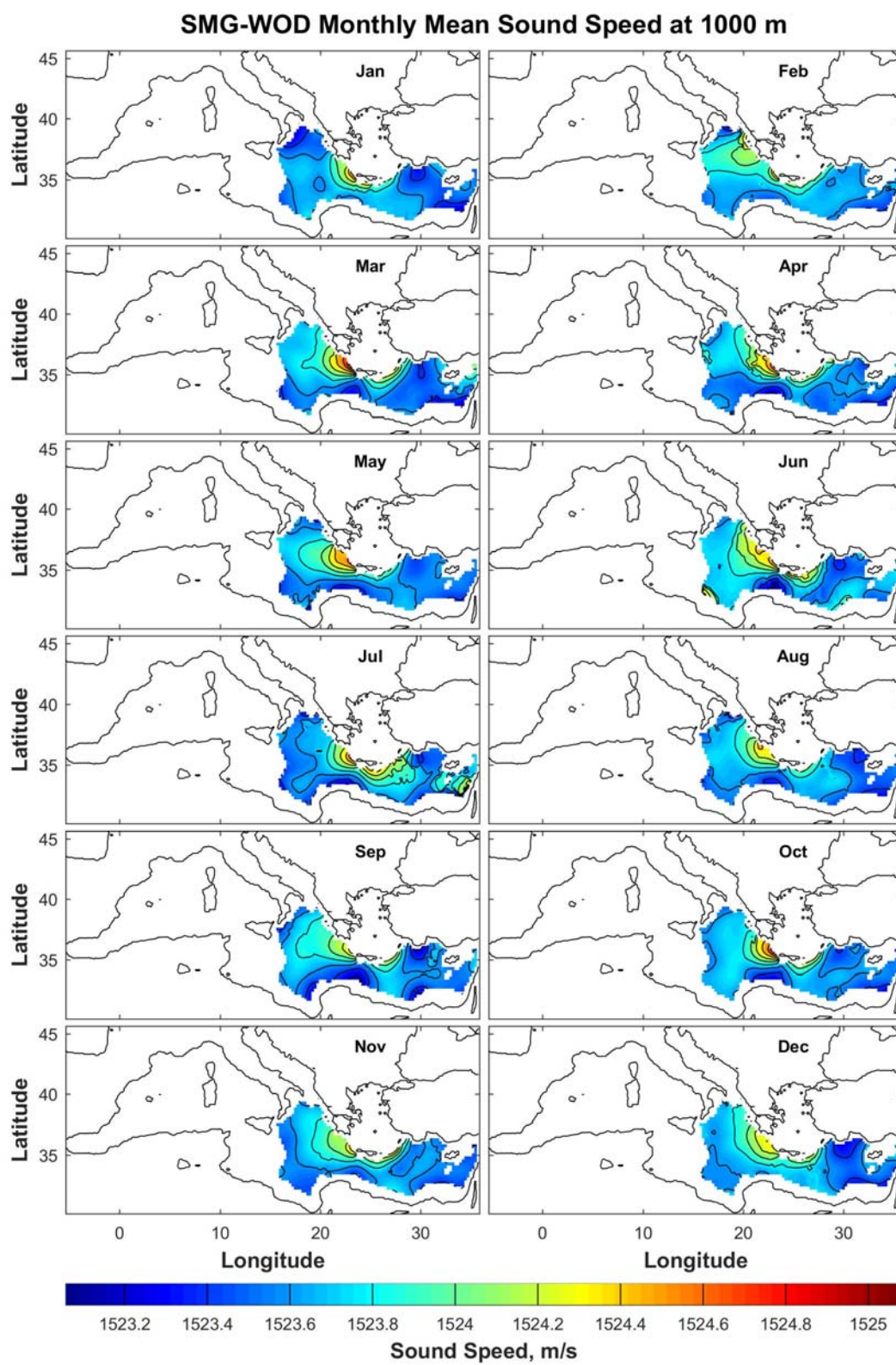GDEM Monthly Spice at 400 m
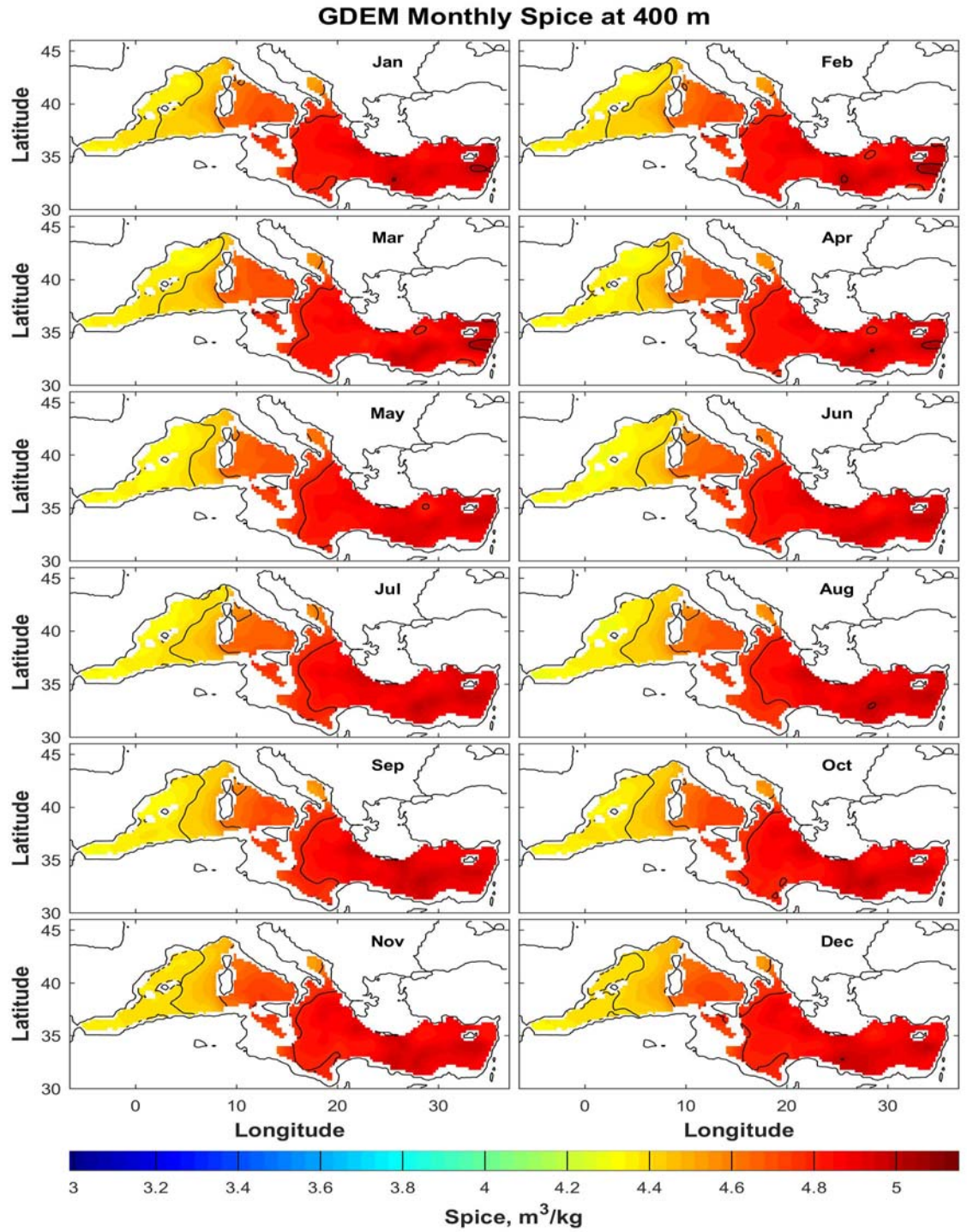
GDEM Monthly Spice at 1000 m

Spice, m³/kg

138

APPENDIX D. ADDITIONAL SMG-WOD MONTHLY MEAN SOUND SPEED FIGURES

SMG-WOD Monthly Mean Sound Speed at 400 m

139

SMG-WOD Monthly Mean Sound Speed at 1000 m

140

APPENDIX E. ADDITIONAL GDEM MONTHLY SOUND SPEED FIGURES

GDEM Monthly Sound Speed at 400 m
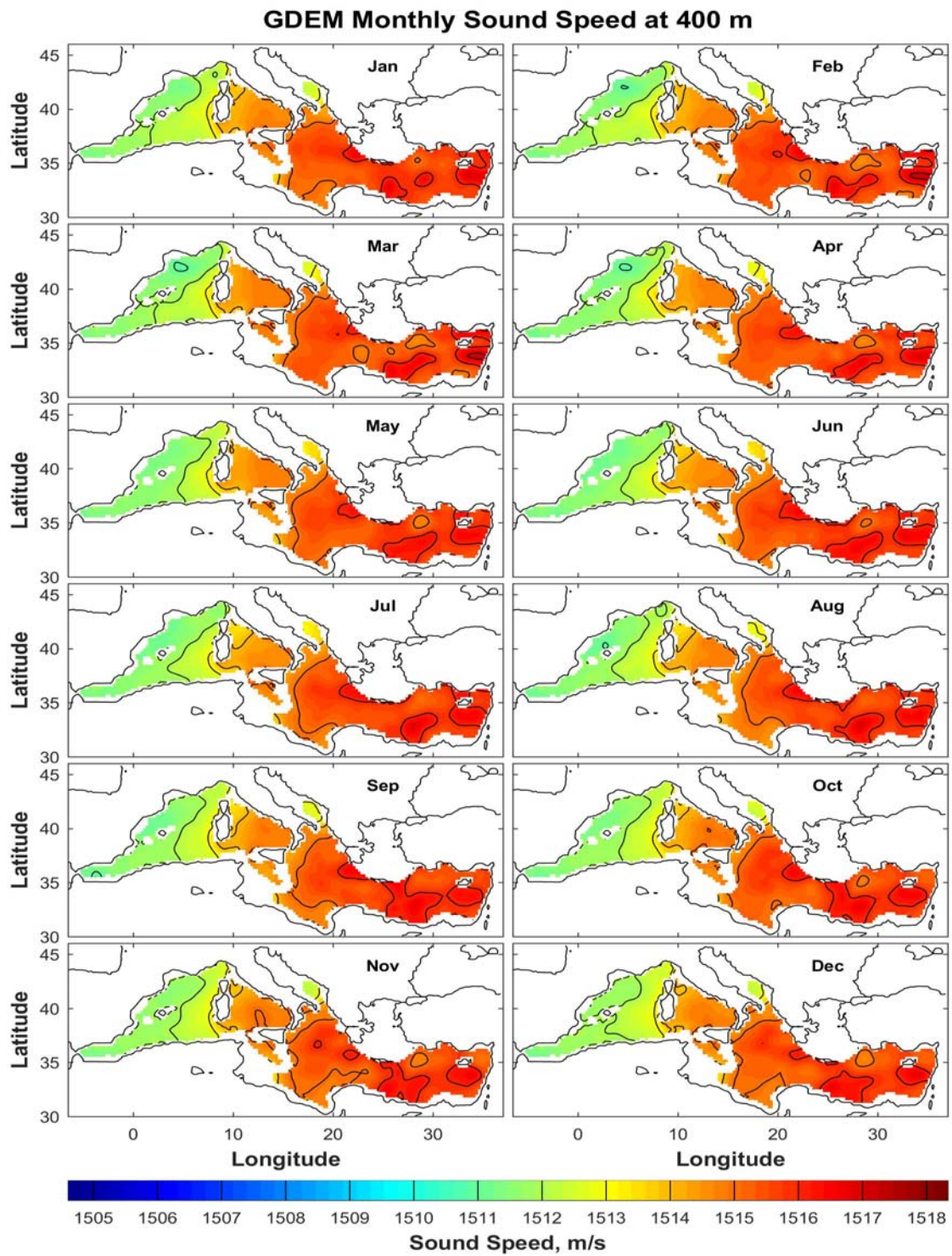
GDEM Monthly Sound Speed at 1000 m
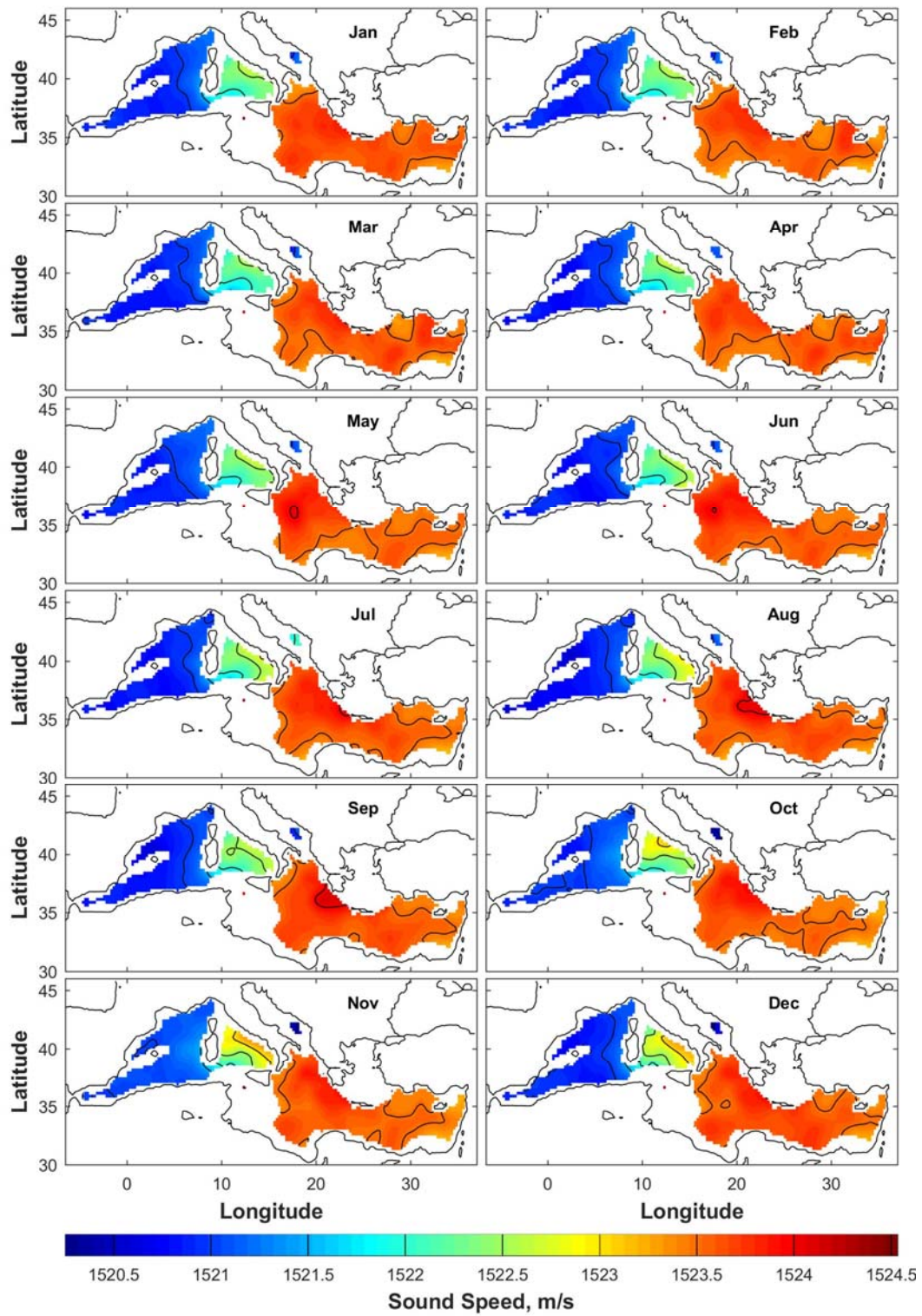
LIST OF REFERENCES

Alhammoud, B., K. Béranger, L. Mortier, M. Crépon, and I. Dekeyser, 2005: Surface circulation of the Levantine Basin: Comparison of model results with observations. *Prog.Oceanogr.*, **66**, 299–320.

Artale, V., D. Iudicone, R. Santoleri, V. Rupolo, S. Marullo, F. D'Ortenzio, 2002: Role of surface fluxes in ocean general circulation models using satellite sea surface temperature: Validation of and sensitivity to the forcing frequency of the Mediterranean thermohaline circulation. *J. Geophys. Res.*, **107,** 29–1–29-24, doi: 10.1029/2000JC000452.

Béranger, K., L. Mortier, and M. Crépon, 2005: Seasonal variability of water transport through the Straits of Gibraltar, Sicily and Corsica, derived from a high-resolution model of the Mediterranean circulation. *Prog. Oceanogr.*, **66,** 341–364.

Béthoux, J. P., 1979: Budgets of the Mediterranean Sea, their dependence on the local climate and on characteristics of the Atlantic waters. *Oceanol. Acta*, **2,** 157–163.

Bindoff, N. L., and T. J. McDougall, 1994. Diagnosing climate change and ocean ventilation using hydrographic data. *J. Phys. Oceanogr.*, **24,** 1137–1152.

Borghini, M., H. Bryden, K. Schroeder, S. Sparnocchia, and A. Vetrano, 2014: The Mediterranean is becoming saltier. *Ocean Sci.*, **10,** 693–700.

Boyer, T. P., and Coauthors, 2013: World ocean database 2013. NOAA Atlas NESDIS 72, 209 pp, doi: 10.7289/V5NZ85MT.

Bryden, H. L., and T. H. Kinder, 1991: Steady two-layer exchange through the Strait of Gibraltar, *Deep-Sea Res.*, **38** (Supplement 1), S445– S463.

Carnes, M. R., 2009: Description and evaluation of GDEM-V 3.0. Naval Research Laboratory. NRL/MR/7330--09-9165, 24 pp. [Available online at https://www7320.nrlssc.navy.mil/pubs/2009/carnes-2009.pdf.]

Chapman, S. J., 2009: *Essentials of MATLAB Programming*. Cengage Learning, 412 pp.

Chu, P. C., C. Cintron, S. D. Haeger, and R. E. Keenan, 2002: Acoustic mine detection using the Navy's CASS-GRAB. *Fifth International Symposium on Technology and Mine Problems, Society for Counter-Ordnance Technology*, Monterey, CA, 10 pp. [Available online at http://hdl.handle.net/10945/36255.]

Chu, P.C., and G.H. Wang, 2003: Seasonal variability of thermohaline front in the central South China Sea. *J. Oceanography, Oceanographic Society of Japan*, **59,** 65–78.

Chu, P. C., Y. Q. Qi, Y. C. Chen, P. Shi and Q. W. Mao (2004): South China Sea wind-wave characteristics. Part I: Valida- tion of Wavewatch-III using TOPEX/Poseidon data. *J. Atmos. Oceanic Technol.*, **21**, 1718–1733.

Chu, P.C., Y.C. Chen, A. Kunikaka, 2005: Seasonal variability of the Yellow Sea/East China Sea surface fluxes and thermohaline structure. *Adv in Atm Sci,* **22,** 1–20.

Chu, P. C., H. Tseng, C. P. Chang, and J. M. Chen, 2007: South China Sea warm pool detected in spring from the Navy's Master Oceanographic Observational Data Set (MOODS). *J. of Geophys. Research*, **102,** 15761–15771.

Chu, P. C., and C. W. Fan, 2016a: Synoptic monthly gridded world ocean database (SMG-WOD). *Geosci. Data J.*, submitted for publication.

Chu, P. C., and C. W. Fan, 2016b: Synoptic monthly gridded three dimensional (3D) World Ocean Database temperature and salinity from January 1945 to December 2014 (NCEI Accession 0140938). Version 1.1. NOAA National Centers for Environmental Information. Dataset. [Available online at http://data.nodc.noaa.gov/cgi-bin/iso?id=gov.noaa.nodc:0140938.]

Chu, P. C., R. T. Tokmakian, C. W. Fan, and C. L. Sun, 2015: Optimal spectral decomposition (OSD) for ocean data assimilation. *J. of Atmos. Oceanic Tech.*, **32,** 828–841.

Department of Oceanography, Naval Postgraduate School, 2015: Surface duct propagation. Accessed 10 November 2016. [Available online at http://www.oc.nps.edu/~bird/oc2930/acoustics/surfaceduct.html.]

DOSITS, 2014: Map of shadow zone in the ocean. Accessed 9 November 2016. [Available online at http://www.dosits.org/people/history/1920/.]

Emerson, C., J. F. Lynch, P. Abbot, Y. T. Lin, T. F. Duda, G. G. Gawarkiewicz, and C. F. Chen, 2015: Acoustic propagation uncertainty and probabilistic prediction of sonar system performance in the southern East China Sea continental shelf and shelfbreak environments. *IEEE J. Oceanic Eng.*, **40,** 1003–1017.

European Ocean Observatory Network, 2000: The schematic of the thermohaline circulation in the Mediterranean Sea. Accessed 22 November 2016. [Available online at http://outreach.eurosites.info/outreach/DeepOceans/station.php?id=7.]

Flament, P., 2002: A state variable for characterizing water masses and their diffusive stability: Spiciness. *Prog. Oceanogr.*, **54,** 493–501.

Fox, H.E., M.B. Mascia, X. Basurto, A. Costa, L. Glew, D. Heinemann, L.B. Karrer, S.E. Lester, A.V. Lombana, R.S. Pomeroy, and others. 2012. Reexamining the science of marine pro- tected areas: Linking knowledge to action. *Conservation Letters,* **5,** 1–10, http://dx.doi.org/ 10.1111/j.1755-263X.2011.00207.x.

GRID-Arendal, 2013: Mediterranean Sea water masses: vertical distribution. Accessed 3 November 2016. [Available online at http://www.grida.no/graphicslib/detail/mediterranean-sea-water-masses-vertical-distribution_d84b.]

Hamilton, E. L., 1980. Geoacoustic modeling of the sea floor. *J. Acoust. Soc. Am.*, **68** (5), 1313–1340.

Hannachi, A., 2004: A primer for EOF analysis of climate data. Dept. of Meteorology, University of Reading, 33 pp. [Available online at http://www.met.rdg.ac.uk/~han/Monitor/eofprimer.pdf.]

Jensen, F. B., W. A. Kuperman, M. B. Porter, and H. Schmidt, 2011: Fundamentals of ocean acoustics. W. M. Hartman., Springer Science, 1–64.

Kalmbach, M. 2011: Estimation of the ocean sound velocity profile. HYPACK, accessed 9 November 2016. [Available online at http://www.hypack.com/new/portals/1/pdf/sb/06_08/Estimation%20of%20the%20Ocean%20Sound%20Velocity%20Profile.pdf.]

McDonald, C. (2016). Inter-annual variability of the acoustic propagation in the Yellow Sea identified from a synoptic monthly gridded database as compared with GDEM. M.S. thesis, Dept. of Oceanography, Naval Postgraduate School, 39–54.

MetEd,UCAR, 2015: Map of sound propagation in the arctic ocean. Accessed 10 November 2016. [Available online at https://www.meted.ucar.edu/sign_in.php?go_back_to=http%253A%252F%252Fwww.meted.ucar.edu%252Foceans%252Farctic_metoc%252Flesson_9_oceanography.htm.]

Millot, C., 1997: Circulation in the Western Mediterranean Sea. *J. Mar. Syst.*, **20,** 423–442.

Millot, C., 2013: Levantine intermediate water characteristics: An astounding general misunderstanding. *Sciente Mar.*, **77,** doi: 10.3989/scimar.03518.13A.

Munk, W., 1981: Internal waves and small-scale processes. *Evolution of Physical Oceanography*, MIT Press, 264–291.

National Oceanography Centre Southampton, 2015: Mediterranean outflow sill. Accessed 3 November 2016. [Available online at http://www.euroargo-edu.org/img/med_outfl_sill.png.]

Naval Oceanographic Office, NAVO, 2006: Database description for bottom sediment type Digital Bathymetric Data Base–Variable Resolution (DBDB-V) version 5.4 (U). Oceanographic and Atmospheric Master Library, OAML-DBD-90, 55 pp.

Naval Oceanographic Office, NAVO, 2009: Database description for the generalized digital environmental model–variable resolution (GDEM-V) version 3.0.1 (U). Oceanographic and Atmospheric Master Library, OAML-DBD-72F, 39 pp.

Office of Ocean Exploration and Research, 2001: Map of sound channel in the ocean. Accessed 9 November 2016. [Available online at http://oceanexplorer.noaa.gov/explorations/sound01/background/acoustics/media/ sofar.html.]

Ozsoy E., A. Hecth, and U. Unluata, 1989: Circulation and hydrography of the Levantine Basin: Results of POEM coordinated experiment 1985–1986. *Prog. Oceanogr.*, **22,** 125–170.

Ozsoy E., U. Unluata, and Z. Top, 1993: The Mediterranean water evolution, material transport by double diffusive intrusions, and interior mixing in the Black Sea. *Prog. Oceanogr.*, **31,** 275–320.

Porter, M. B, 2011: The BELLHOP manual and user's guide: Preliminary draft. Heat, Light, and Sound Research, Inc. 57 pp.

Reddy, M. P. M., 2001: *Descriptive Physical Oceanography*. A. A. Balkema, 299 pp.

Renilson, M., 2015: Hydro-static Performance. *Submarine Hydrodynamics*, Springer Science, 147–148.

Robinson, W., G. Leslie, A. Theocharis, A. Lascaratos, 2001: *Mediterranean Sea Circulation*. Academic Press, doi:10.5194/cp-11-233-2015.

Rodriguez, D. L., 2016: Inter-annual variability of the California current system and associated biochemical characteristics from prolonged data series. M.S. thesis, Dept. of Oceanography, Naval Postgraduate School, 129 pp.

Tanabe, R., 2013: Mediterranean Sea. Accessed 3 November 2016. [Available online at http://www.newworldencyclopedia.org/p/index.php?title=Mediterranean_Sea&ol did=971160.]

Tchernia, P. 1980: *Descriptive Regional Oceanography*. Pergamon, 289 pp.

Topper, R. P. M., and P. Th. Meijer, 2015: Changes in the Mediterranean circulation and water characteristic due to restriction of the Atlantic connection: A high-resolution ocean model. *Clim. Past*, **11,** 233–251, doi:10.5194/cp-11-233-2015.

WorldAtlas, 2015: Map of the Mediterranean Sea. Accessed 3 November 2016. [Available online at http://www.worldatlas.com/aatlas/infopage/medsea.htm.]

World Facts Inc., 2016: Map of the Mediterranean Sea. Accessed 3 November 2016.
[Available online at https://sites.google.com/site/worldfactsinc/the-mediterranean-sea-and-it-s-islands.]

THIS PAGE INTENTIONALLY LEFT BLANK

INITIAL DISTRIBUTION LIST

1.   Defense Technical Information Center
        Ft. Belvoir, Virginia

2.   Dudley Knox Library
        Naval Postgraduate School
        Monterey, California